Microstructure Evolution in Electrodeposited Copper Thin Films for Advanced Microelectronic Applications

by

Nidal Khalaf Alshwawreh

B.Sc., United Arab Emirates University, 2000
M.Sc., United Arab Emirates University, 2007

A THESIS SUBMITTED IN PARTIAL FULFILLMENT OF
THE REQUIREMENTS FOR THE DEGREE OF

DOCTOR OF PHILOSOPHY

in

The Faculty of Graduate Studies

(Materials Engineering)

THE UNIVERSITY OF BRITISH COLUMBIA

(Vancouver)

April 2012

Abstract

Copper interconnects in advanced integrated circuits are manufactured by processes that include electrodeposition, chemical mechanical polishing and annealing. The as-deposited copper is nano-crystalline and undergoes a microstructure evolution at room temperature (self-annealing) or during an annealing step. During this process, significant changes in resistivity and grain size are observed. In this work, the microstructure evolution in 0.5-3 μm-thick electrodeposited copper thin films was studied. Resistivity measurements were used to quantify the role of deposition conditions on the microstructure evolution rate. In-situ electron backscatter diffraction (EBSD) was employed to observe self-annealing at the film surface. The resistivity-microstructure correlation during self-annealing was examined. A phenomenological model using the Johnson-Mehl-Avrami-Kolmogorov (JMAK) approach was developed to describe recrystallization during isothermal and continuous annealing treatments. The microstructure evolution in copper-silver alloys and films produced by variable deposition rates was investigated. Phase-field model was applied to simulate self-annealing and the effect of deposition current density.

The results show that the drop in resistivity during self-annealing is accompanied by significant changes of the microstructure at the film surface.

Abstract

Different criteria were developed to assess self-annealing rate from EBSD maps including grain size, image quality and local orientation spread. Adopting a grain size threshold, it was found that there is a reasonable correlation between resistivity and microstructure during self-annealing. The recrystallization in copper thin films appears to be thermally activated with an activation energy of 0.89-0.93 eV. Adopting the principle of additivity, it was found that the recrystallization rate during continuous annealing can be described by the JMAK model using the isothermal resistivity profiles. A method was proposed to accelerate recrystallization based on a capping layer deposition. No recrystallization was observed when silver was co-deposited with copper in the absence of chloride (even when annealed at 100 °C for 5 hours). Phase-field model was able to describe self-annealing and the effect of deposition current density. The results in this thesis are of significance to the microelectronic industry where recrystallization is a crucial step in the fabrication of copper interconnects for the high performance integrated circuits.

Preface

A version of chapter 5 was published. N. Alshwawreh, M. Militzer, D. Bizzotto, JC. Kuo, Resistivity-Microstructure Correlation of Self-Annealed Electrodeposited Copper Thin Films. (2012) Microelectronic Engineering, 95, 26-33. I have performed all experiments and analyzed all the data under the guidance of my supervisors (Prof. M. Militzer and Prof. Dan Bizzotto). Some of the experiments (electron backscatter diffraction experiments) were conducted in the laboratory of Dr. JC. Kuo in The National Cheng Kung University in Taiwan. I wrote the manuscript and the co-authors provided me with suggestions to revise it and prepare it for submission.

A version of chapter 6 was published. N. Alshwawreh, M. Militzer, D. Bizzotto, Recrystallization of Electrodeposited Copper Thin Films During Annealing. (2010) Journal of Electronic Materials, 39, 11, 2476-2482. I have designed and performed all the experiments. I wrote the manuscript and the co-authors provided me with suggestions to interpret the data and prepare the manuscript for publication.

Table of Contents

Appendices

List of Tables

List of Figures

List of Symbols

η	The interface thickness
Γ	The dislocations density in the microstructure
Ω	The atomic volume
ω	The magnitude of electron scattering from the grain boundary
ϕ	The order parameter (or field variable) in the phase field model
σ^*	The interface energy
C_f	The correction factor for interface mobility
K_{sp}	The solubility product
Q_{rex}	The effective activation energy for recrystallization
T_p	The temperature at which the exothermal peak in the differantial scanning calorimetry is observed.
w	The width of the interconnect line
j^*	The deposition current density
$\bar{n}$	The number of electrons involved in the electrochemical reaction

β The heating rate during continuous annealing treatment

ΔP The driving pressure for microstructure evolution

δ The atomic jump distance in the boundary

γ_{gb} The grain boundary energy

λ The intrinsic mean free path of electrons

μ The shear modulus

ν The Poisson's ratio

ρ The electrical resistivity

ρ_0 The as-deposited resistivity

ρ_∞ The resistivity after self-annealing is complete

ρ_g The resistivity contribution from grain boundaries

ρ_{inc} The resistivity during the incubation period

ρ_i The resistivity contribution from impurities

ρ_n The normalized resistivity

ρ_p The resistivity contribution from phonons

ρ_s The resistivity contribution from surfaces

ρ_T The bulk resistivity of the material

σ The flow stress

τ The time required to achieve a certain fraction recrystallized isothermally

$\varepsilon\varepsilon_0$ The interlayer dielectric constant

ξ A term which describes the relative sensitivity of the oxidization/reduction processes to the overpotential

A_d The deposition area

b_v The magnitude of the Burger's vector

C_0 The bulk electrolyte concentration

D The density of copper

d The thickness of the interconnect line/film

D_{gb} The grain boundary diffusion coefficient

$E - E_{eq}$ The applied overpotential during electrodeposition

F The Faraday's constant

f The fraction recrystallized

F_v The volume fraction of the pinning particles

G The grain size

I The injected current during resistivity measurments

i The deposition current

j The flowing current density in the interconnect line

k_B The Boltzmann's constant

L The length of the interconnect line

M The grain boundary mobility

M_w The molecular weight of copper

n The Avrami exponent

p The distance between the interconnectsl lines

P_z The pinning pressure

q The total charge during electrodeposition

Q_a Activation energy for electromigration

R The gas constant

r The grain radius

r_d The dislocation loop radius

r_p The radius of the pinning particles

RC_{delay} The time delay caused by the resistance and capacitance

t The time

T The temperature

$t_{50\%}$ The time for 50% recrystallization

t_F The median time to failure due to electromigration

V The measured voltage during resistivity measurement

v The velocity of the grain boundary

Acknowledgments

I would like to thank my supervisor Prof. Matthias Militzer for giving me the chance to work on this project and for his continuous support and guidance. I also would like to thank my co-supervisor Prof. Dan Bizzotto for his encouragement and support. I benefited a lot from my supervisors knowledge and feedback during the project meetings and discussions. Many thanks for Dr. Chad Sinclair and Dr. John Madden for their suggestions and useful feedback.

I am so thankful for Dr. Jui-Chao Kuo for accepting me to work in his lab in Taiwan. I am thankful for his students Delphic Chen, Wei-Ling Lin and Hung-Pin Lin for their kind assistance. I appreciate the help from Dr. Aya Soda, Amanda Musgrove and all the members of Prof. Bizzotto's lab. Many thanks for summer students Katherine Lawrie and Saara Mehtonen. I would like to thank all members of the microstructure group, the staff and students in the clean room in AMPEL and the staff in the department of Materials Engineering. I would like to acknowledge the funding from The Natural Sciences and Engineering Research Council of Canada (NSERC).

I thank my parents (Zahra and Khalaf), my wife Rasha, my daughter Luma and my son Salem for their continuous love and patience.

I thank ALLAH for giving me the power to finish this work.

Chapter 1

Introduction

In any integrated circuit (IC), millions of transistors are fabricated by precisely doping a semiconductor material like silicon. These transistors are linked to each other by a backbone network of wires (interconnects). These interconnects provide the physical channel that carries electrical signals between transistors as well as power, clock and ground signals. The features size in advanced integrated circuits and microprocessors has been dramatically reduced from 3 μm in 1970 to 28 nm in 2011. This is inline with Moore's law which predicts that the density of transistors will double every 18-24 months as a consequence of the increasing demand for high performance ICs. High performance and reliability of back-end-of the line (BEOL) interconnects are crucial for future microprocessors and integrated circuits. Copper replaced aluminum in the last 10 years as the interconnect material of choice because of its lower resistivity and better reliability. As feature sizes approach the mean free path of electrons, interconnect resistivity dramatically increases due to a higher resistivity contribution from surfaces and sidewalls. As a consequence, interconnect time delay increases and the propagation speed of electrical signals throughout the integrated circuit is reduced. Moreover, power consumption and electromigration-induced failure are magnified with the increase in the applied current density.

With these challenges, a proper design of interconnect microstructure becomes essential. Electrodeposition using the Dual Damascene process is the method of choice in the semiconductor industry for interconnect fabrication. However, the role of organic additives in the electrochemical bath and the microstructure evolution phenomenon that takes place after deposition are still under debate. In electrodeposited copper films, the as-deposited nanocrystalline microstructure is unstable and undergoes a remarkable spontaneous evolution process at room temperature, known as self-annealing, whereby an order of magnitude increase in the grain size is observed in a period of few hours to several days. The transformation in the microstructure causes significant changes in the film resistivity as well as stress and ductility. There was a debate in the literature whether self-annealing phenomenon can be described by grain growth, abnormal grain growth or recrystallization. Additionally, the role of additives and alloying elements on copper self-annealing are not yet well understood. Therefore, a better understanding of the microstructure evolution phenomenon in copper interconnects is of a great importance and will provide the knowledge necessary to improve interconnects performance and to address the accelerated reliability challenges.

In this work, the phenomenon of self-annealing was studied. The work included a systematic investigation of the effect of deposition conditions (deposition current density, film thickness and electrolyte age) on self-annealing rate. Moreover, the film microstructure during self-annealing was observed by in-situ electron backscatter diffraction technique. The correlation between the film microstructure and its electrical properties during self-annealing was then discussed. In addition, self-annealing phenomenon was simulated using

phase-field which is an emerging tool to model microstructure evolution processes that include grain growth and recrystallization.

Annealing is a key step in the fabrication of integrated circuits where copper interconnects are heat treated at elevated temperature to promote fast microstructure evolution. In this way, low resistivity of the interconnect line is obtained in a reasonable time. There are models available in the literature which describe the rate of self-annealing as a function of time after deposition. However, a model to describe the effect of temperature during annealing treatment is not available despite its significance to the microelectronic industry. In this work, the microstructure evolution during isothermal and continuous annealing treatments was quantified using resistivity measurements. Based on the experimental results, a phenomenological model was developed using the Johnson-Mehl-Avrami-Kolmogorov (JMAK) approach.

To improve the reliability of copper interconnects, several novel deposition strategies were proposed in the literature including pulse-deposition and alloying. In this work, the microstructure evolution in films produced using variable deposition rates was studied using resistivity and electron backscatter diffraction techniques. From these results, a deposition strategy was proposed to accelerate the microstructure evolution in copper interconnects. Further, the microstructure evolution in films that are produced by copper-silver co-deposition was investigated.

The structure of this thesis is as follows: chapter 2 provides a survey of the literature and followed by an outline of the research objectives (chapter 3). Chapter 4 deals with the materials and the experimental methodology

that was followed. The results related to the phenomenon of self-annealing and resistivity-microstructure correlation are presented in chapter 5. The microstructure evolution during annealing treatment of copper thin films is covered in chapter 6. Microstructure evolution in novel interconnects is presented in chapter 7. Phase-field modelling is discussed in chapter 8 and followed by a summary and recommendations for future work (chapter 9).

Chapter 2

Literature Review

2.1 RC Delay

When electrical signals propagate through metallic interconnects, they experience a time delay caused by the resistance of the interconnect and the capacitance of two adjacent interconnects separated by a dielectric material. This delay is known as RC delay (RC_{delay} = Resistance $\times$ Capacitance). It is well known that transistors switching frequency is inversely proportional to their size and the time needed for a transistor to switch between two logic states is referred to as the intrinsic gate delay. As the technology node drops below 0.25 μm, RC_{delay} becomes more significant than the intrinsic gate delay of transistors. This trend is illustrated in Fig. 2.1. As a consequence, the design rules for integrated circuits become restricted which negatively affects further development of high performance ICs. Bohr [1] used an electrical model to describe the RC_{delay} as a function of the properties of the interconnect and dielectric materials where RC_{delay} can be expressed as

$$RC_{delay} = 2\rho L^2 \varepsilon\varepsilon_0 \left(\frac{4}{p^2} + \frac{1}{d^2}\right) \tag{2.1}$$

where ρ, L, d are the resistivity, length and thickness of the interconnect respectively, while $\varepsilon\varepsilon_0$ and p are the interlayer dielectric constant and the

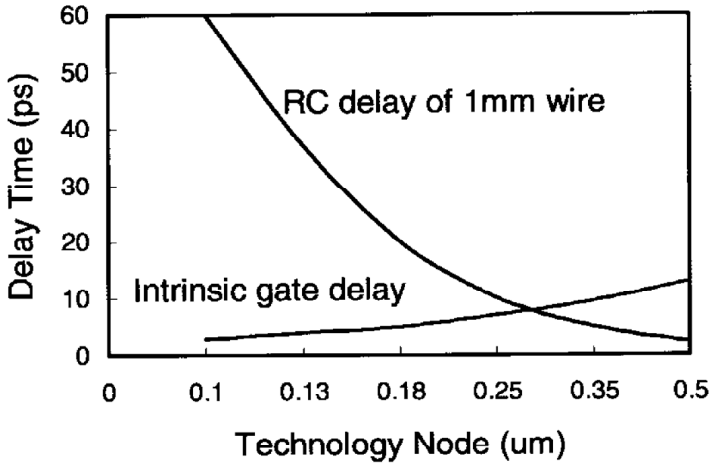

Figure 2.1: Intrinsic gate delay of a transistor vs. RC_{delay} of interconnect. [2]

distance between the metal lines, respectively. The model shows that RC_{delay} strongly increases as the interconnects length increases. Further downsizing of features size requires smaller dimensions which also contributes to a higher RC_{delay}. As implied by Eq. 2.1, the effect of scaling can be minimized by selecting interconnect materials with low resistivity and dielectrics with low permittivity constant.

2.2 Copper/low-K Metallization

Aluminum was universally used as interconnect material since the 1970s. As feature sizes dropped to the deep submicron range, aluminum reached its technological limits and the RC_{delay} started to limit the development of high performance ICs. In 1998, copper replaced aluminum as the material of choice for interconnects when IBM introduced its 0.18 μm-complementary metal oxide (CMOS) chip based solely on copper metallization. A compar-

ison between copper and other possible interconnect materials is shown in Table 2.1. Copper was an excellent candidate to replace aluminum due to its better conductivity which allowed for longer and thinner interconnect lines to be fabricated. As a consequence, faster microprocessors with less power consumption were produced. In addition to the conductivity advantage, switching to copper improved the reliability of interconnects by being more immune to electromigration which is the diffusion of atoms under high applied current density. High electromigration resistance is desirable since electromigration leads to voids and hillock formation in the interconnect line which elevates the resistance and may eventually lead to a complete failure of the microsystem. Copper has electromigration resistance which is several orders of magnitude higher than that of aluminum which allows for high current density to be sustained. Black [3] formulated a semi-empirical equation for the median time to failure,, where:

$$t_F = \frac{A}{j^2} \exp\left(\frac{Q_a}{k_B T}\right) \tag{2.2}$$

Here, A is a constant which is related to the cross sectional area, j is the current density, T is the temperature, Q_a is the activation energy for electromigration and k_B is Boltzmann's constant. According to Eq. 2.2, the interconnect life time decreases with increasing current density and temperature. About 10 years following the introduction of Cu interconnects, electromigration and reliability challenges are magnified and significant effort has been made to improve the reliability of Cu interconnects [4–15]. Fig. 2.2 shows an example of interconnect line failure due to electromigration.

The reason why aluminum survived as interconnect material for a long

Table 2.1: A comparison between the properties of possible interconnect materials. [16]

Property	Metal			
	Cu	Ag	Au	Al
Resistivity ($\mu\Omega$.cm)	1.67	1.59	2.35	2.66
Thermal coefficient of resistivity (K^{-1})	0.0043	0.0041	0.004	0.004
Thermal conductivity (W cm^{-1})	3.98	4.25	3.15	2.38
Melting point (°C)	1085	962	1064	660
Corrosion in air	Poor	Poor	Excellent	Good
Self-diffusion Q(eV)	2.19	1.97	1.81	1.48
Mean free path (nm)	39	52	38	15

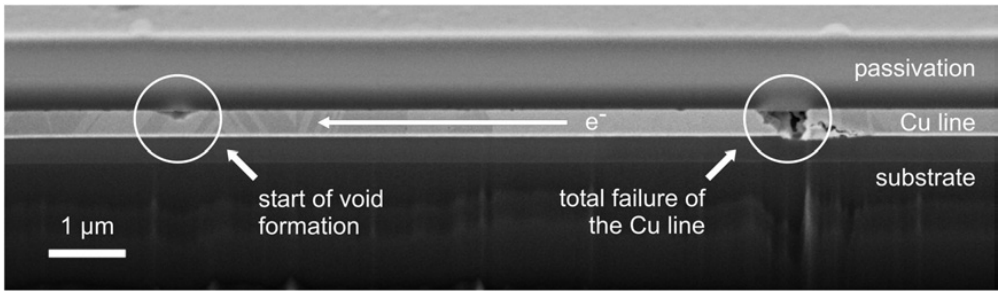

Figure 2.2: Focused-ion-beam (FIB) image of the cross section of a Cu interconnect line after electromigration failure. [15]

period of time before replacing it with copper is that there were a number of challenges associated with producing copper interconnects in a commercial scale. One of these challenges is the low resistance to corrosion which was improved by passivating the interconnect surface (normally by capping the metal line with a thin layer of Si_3N_4 using techniques like plasma enhanced chemical vapor deposition (PECVD) [15, 17]). Also, copper reacts with silicon at room temperature which necessitates the use of a barrier layer between the silicon wafer and the copper deposit to eliminate copper diffusion into silicon. Tantalum (Ta) and Tantalum based films (e.g. TaN)

were used for this purpose [18]. Silicon oxide (SiO_2) was traditionally used as an interlayer dielectric material between interconnects. However, it was found that materials with dielectric constants lower than that of SiO_2 (which equals to 4.5) along with copper metallization significantly reduce the interconnect time delay [19]. One of these materials (often referred to as low-K dielectrics) is SiCOH which is produced by doping SiO_2 with carbon [20]. The dielectric constant of SiCOH is significantly lower than SiO_2 (2.7-3.0) and was used in the 90 nm technology node. The dielectric constant can be further reduced by using porous SiCOH which was introduced in the 45 nm technology node [20]. Here, air gaps in the dielectric material contribute to lower dielectric constant [21, 22] since air has a dielectric constant of unity. The Cu/low-K enables for a highly complex microprocessors to be fabricated with several layers of metallization as shown in Fig. 2.3.

2.2.1 Dual Damascene and Electrodeposition

Unlike aluminum, copper lines cannot be fabricated by reactive ion etching and a new process was necessary for copper metallization. In this process, introduced by IBM and referred to as Damascene process, a dielectric layer (e.g. low-K material) is deposited on a silicon wafer by PECVD followed by lithography and etching to fabricate high aspect ratio trenches. A few nanometer thick barrier (Ta, TaN, Ti or TiN) and seed layers (Cu) are then deposited in these trenches by physical vapor deposition (PVD) [24,25]. Copper is then electrodeposited in the trenches and vias followed by chemical mechanical polishing (CMP) planarization to remove the excess deposit on the trench surface [19]. Single Damascene refers to the process of filling trenches

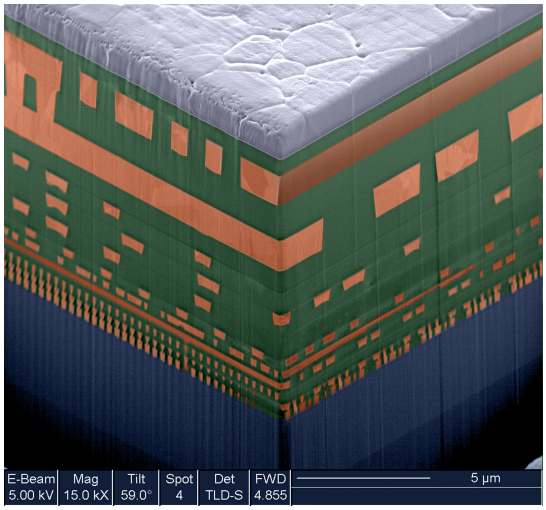

Figure 2.3: Cross-section of 64-bit high performance microprocessor chip built in IBM's 90 nm CMOS technology with Cu/low-K wiring. Courtesy of International Business Machines Corporation, © International Business Machines Corporation. [23]

(one level) while Dual Damascene (DD) refers to the filling of trenches and vias simultaneously. Etch stop or cap-layer (SiN, SiC...) is deposited after the CMP to facilitate subsequent layer metallization. Figure 2.4 shows a schematic diagram of the DD process.

Electrodeposition is selected in the DD process as the method of choice to deposit copper in trenches and vias because of its ability to achieve high quality filling characteristics of deep features especially when compared with CVD and PVD techniques. Electrodeposition is performed in a copper-containing electrolyte and involves the use of a working electrode (i.e. substrate) and a reference electrode in an electrochemical cell. Upon applying an external negative potential between the working electrode (cathode) and the reference (anode), the system will deviate from its equilibrium state and the following

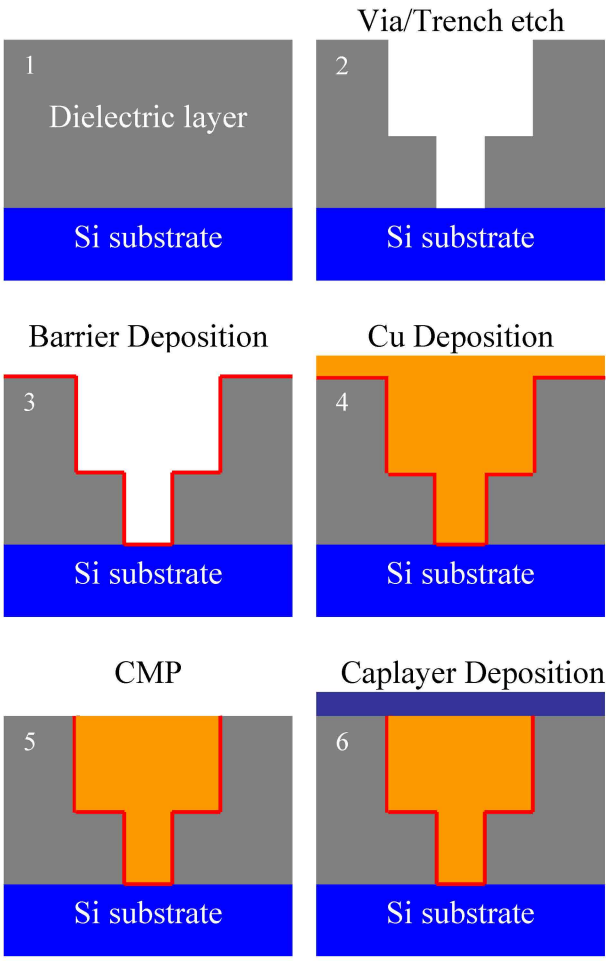

Figure 2.4: Flow for the fabrication of Cu interconnects in the Dual Damascene process.

oxidation/reduction reaction takes place

$$Cu_{(s)} \rightarrow Cu^{+2}_{(aq)} + 2e^{-} \text{ (Anode)}$$

$$Cu^{+2}_{(aq)} + 2e^{-} \rightarrow Cu_{(s)} \text{ (Cathode)}$$

This reduction reaction leads to a deposition of Cu on the working electrode (i.e. seed layer). The deposition current can be described by the Butler-Volmer model where the relation between the deposition current, i, the overpotential, $E - E_{eq}$, and the bulk electrolyte concentration, , can be described as

$$i = i_0 \left(\frac{C_0 \left(0, t\right)}{C_0} \right) \exp \left(\frac{-\bar{n} \xi F \left(E - E_{eq}\right)}{RT} \right) \tag{2.3}$$

Here i_0 is an important kinetic term referred to as exchange current, t is the time, R is the gas constant , F is Faraday's constant, $\bar{n}$ is the number of electrons involved in the reaction, and ξ is a term which describes the relative sensitivity of the oxidization/reduction processes to the overpotential [26, 27]. In commercial baths used for copper metallization, high concentration of copper is required to achieve a rapid deposition. Sulfuric acid is usually added to the electrolyte to increase the conductivity and minimize the potential gradient during electroplating which results in a uniform filling [26]. In addition to the concentration of the bath, applied potential and temperature, the quality and the rate of the electrodeposition depend highly on the presence of additives and the quality of the seed layer.

Three types of profile evolution are possible in the Damascene process: (i) Subconformal filling occurs when there is substantial copper ion depletion

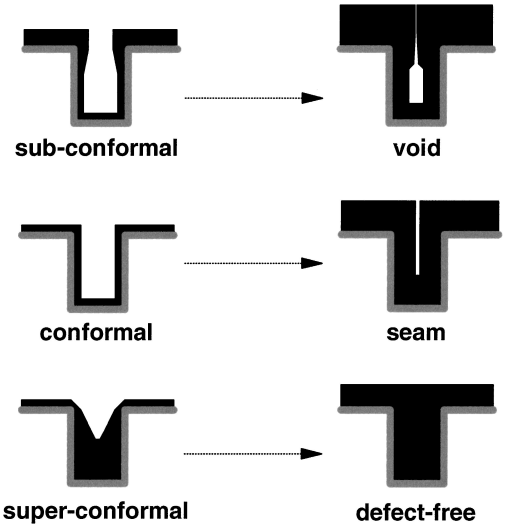

Figure 2.5: A schematic for the evolution of copper filling in a via with different degrees of conformality. [33]

in the trench which makes current to flow more in the accessible locations outside the trench [28]. Subconformal filling ultimately results in a formation of voids in the trench (see Fig. 2.5). (ii) Conformal filling happens when the deposition rate is equal in all feature sides which eventually leads to the formation of a seam in the final structure. (iii) Superfilling (superconformal) occurs when the deposition rate in the bottom of the trench is higher compared with that on the sides which results in a complete and seamless filling characteristics. Since voids and seams increase the deposit resistance, superfilling is highly desirable for high performance interconnects [29–32].

2.2.2 Role of Additives

It was reported that electrolytes containing only copper sulfate, sulfuric acid and chloride ions produce a conformal filling characteristics [26]. On the other

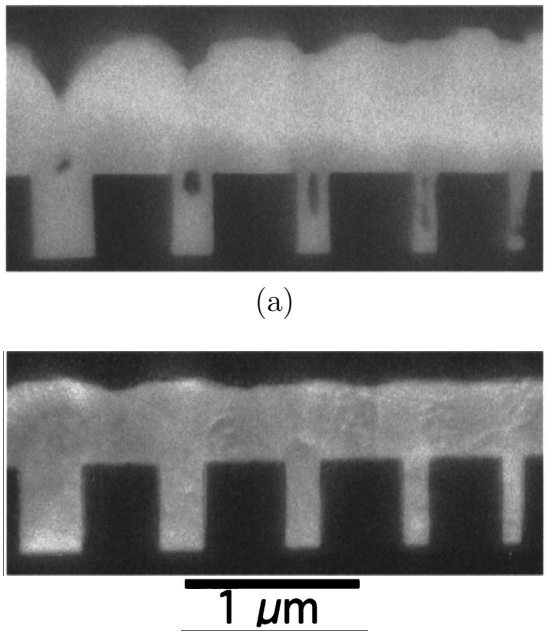

(a)

(b)

Figure 2.6: The Cu filling characteristics of high aspect ratio vias by electrodeposition in the (a) absence, (b) presence of additives. [37]

hand, superconformal filling can be achieved by the aid of certain organic additives like polyethylene glycol (PEG), bis(3-sulfopropyl) disulfide (SPS) and Janus green B (JGB) (see Fig. 2.6). The effect of these organic additives on copper electrodeposition can be classified as a brightener/accelerator, inhibitor/suppressor or leveler. PEG, which is a long chain polymer, produces an inhibitory effect on the deposition kinetics especially in the presence of chloride [28,34] while SPS accelerates the deposition rate at sites where it adsorbs [35, 36]. Compounds like 3-mercapto-1-propanesulfonate (MPSA) can also act as accelerators [31]. Levelers like JGB are added in low quantities to the electroplating bath to suppress the growth rate at regions with high mass transfer rates thus limiting the copper deposit thickness above trenches

and vias [26]. The suppressing effect of the leveler on the deposition rate in the bottom of the high aspect ratio trench is less effective compared with corners or protruding surfaces. In this way the final trench/via deposit will be at the same level as that on the surface. However, Kelly et al. [38] found that all three additives have to be present to achieve leveling, suggesting additive-additive interaction is responsible for leveling. Using cyclic voltammetry (CV) studies, it was found that electrolytes with accelerators (i.e. SPS or MSPA) produce a deposition current which is several times larger than that produced when inhibitors are present in the electrolyte at a given potential [26]. Moffat et al. [31] found that the deposition kinetics are heavily affected by the concentration of MPSA in the presence of other additives.

Several mechanisms were proposed in the literature to describe the role of additives in superfilling. Andricacos et al. [25] suggested that the superfilling is a diffusion-controlled process where the inhibition flux varies in the bottom of the trench and in the sidewalls and corners. The diffusion-controlled theory explains the superfilling as follows: initially, electrolyte containing all additives fills the via due to capillary forces. PEG has strong adsorption rate and covers the side walls of the via which produces a PEG diffusion flux in the via. However, PEG has very slow transport rate to reach the bottom of the via and this will give sufficient time for SPS which has strong adsorption on additive-free surfaces to cover the bottom of the via. Unlike PEG, SPS filling is not mass transport limited which results in accelerating the deposition in the bottom of the via while the deposition on the sidewalls is inhibited. PEG can not displace SPS during via filling because of the strong adsorption kinetics of SPS on the additive-free surfaces. However, SPS can

displace PEG slowly. A full description of the mass transport kinetics of additives was obtained by Akolkar and Landau [39]. A similar mechanism was proposed by Kondo et al. [35] who suggested that PEG-Chloride molecules inhibit the deposition process by adsorption on the trench/via entrance while accelerating complex compounds accumulate in the bottom of the trench/via which results in a superconformal filling. West et al. [40], Moffat et al [31] and Josell et al. [29] claimed that the diffusion-controlled mechanism is not able to describe key superfilling observations like the initial period of conformal growth and the formation of overfill bumps after the filling is complete and proposed another mechanism based on the curvature-enhanced accelerator coverage (CEAC). In this mechanism, there is a competition between inhibitors and accelerators and the accelerator is assumed to displace the inhibitor in deep features and remains segregated at the surface during deposition. A numerical model was then developed [31, 37] and the simulated filling profiles were in agreement with the experimental observations. CEAC theory received acceptance in the literature [41–43] and is believed to describe the superfilling mechanism better than the diffusion-controlled theory.

2.3 Microstructure Evolution in Copper Interconnects

Electrodeposited copper thin films and interconnects undergo a room temperature microstructure evolution soon after deposition. Initially, the Cu microstructure is metastable with an average grain size in the order of 100 nm. The corresponding resistivity of the as-deposited thin film is normally

20-40% higher than the nominal resistivity of bulk copper (1.67 $\mu\Omega$.cm). After an incubation period of a few hours, a sharp decrease in the resistivity is measured (see the normalized resistivity profile in Fig. 2.7). The change in resistivity indicates an underlying microstructure evolution since resistivity is strongly affected by the average grain size and defect density. As shown in the corresponding microstructure in Fig. 2.7, some grains with sizes bigger than the mean grain size start to appear at about 10 hours after deposition. These grains then continue to grow and consume the microstructure. After about 40 hours following the deposition, the resistivity saturates around the nominal resistivity of copper (total change in resistivity is$\approx$ 20%). Along with the changes in resistivity and grain size, changes in the residual stress are also measured. This microstructure phenomenon is referred to as self-annealing since no heating is involved. In addition to the resistivity drop and stress relaxation, other physical properties are also affected by self-annealing. For example, significant ductility increase was observed by Hasegawa et al. [44]. On the other hand, Dong et al. [45] reported a decrease in the film hardness where the initial and final hardness values are functions of the deposition current density. Teh et al. [46] investigated the surface roughness after the deposition using atomic force microscope (AFM). The researchers reported an immediate increase in the surface roughness for about 30 hours after deposition.

To explain the resistivity changes during self-annealing, it is helpful to discuss the origin of resistivity in polycrystalline materials. The electrical resistivity of any material is due to the electron scattering events that occur when an external voltage is applied. The level of scattering determines the

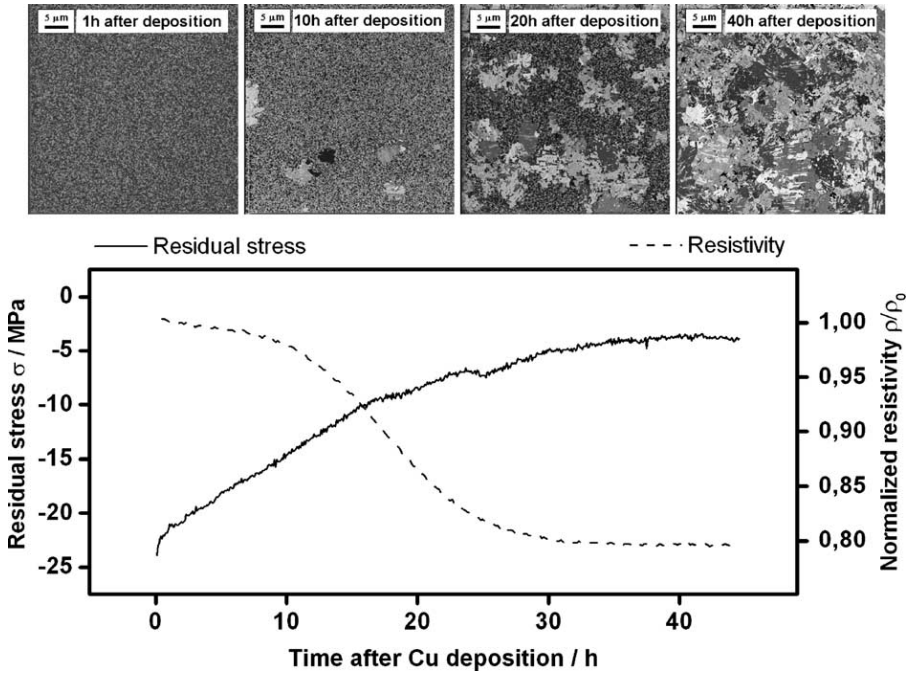

Figure 2.7: Self-annealing of 1 μm-thick Cu film deposited at 15 mA/cm^2 characterized by FIB, resistivity and stress measurements. The film was deposited on 3-inch Si (100) wafer with 50 nm-thick Cu seed layer. [47]

intrinsic resistivity of the material. The changes in the film resistivity during self-annealing can be explained using Matthiessen's rule. According to this rule, the total resistivity of a material, ρ_T, can be expressed as

$$\rho_T = \rho_p + \rho_g + \rho_s + \rho_i \tag{2.4}$$

where ρ_p, ρ_g, ρ_s and ρ_i are the resistivity contribution from phonons, grain boundaries, surfaces, and impurities, respectively. Mayadas and Shatzkes [48] modelled the grain boundary contribution to the resistivity. According to their model (often referred to as MS model), the ratio between the resistivity with grain boundaries, ρ_g, and the bulk resistivity, ρ_T, can be expressed as

$$\frac{\rho_g}{\rho_T} = \left[1 - \frac{3\alpha}{2} + 3\alpha^2 - 3\alpha^3 \ln\left(1 + \frac{1}{\alpha}\right)\right]^{-1} \tag{2.5}$$

$$\alpha = \frac{\lambda}{G}\frac{\omega}{1-\omega}$$

where G is the grain size and λ represents the intrinsic mean free path of electrons which is temperature-dependent (39 nm for pure Cu at room temperature [49]). The term ω is a coefficient (between 0 and 1) that represents the magnitude of electron scattering from the grain boundary where a value of 1 represents full scattering of electrons while 0 represents no scattering at all. The value of ω is material dependent and estimated to be between 0.2 and 0.4 for copper [49, 50] while ω=0.5 was experimentally determined by Shimada et al. [51] for 1 μm-thick electrodeposited Cu films. The different values that are available in the literature for the coefficient ω may be related to the difference in the purity level of the sample. The MS model shows that there is a strong relationship between the average grain size and the electrical properties of the material which is in agreement with what occurs during self-annealing. When the thickness of a conductor becomes comparable to its electrons mean free path, the surfaces of the materials will contribute significantly to the total resistivity. This phenomenon is known as the size effect and is considered a major issue in interconnects design. The contribution of surface scattering as compared to the bulk resistivity can be described as [50, 52, 53]:

$$\frac{\rho_s}{\rho_T} = \frac{3}{8}\left(1 + \frac{w}{d}\right)(1 - x_c)\frac{A_g\lambda}{w} \tag{2.6}$$

where w is the width, x_c is a constant in the range of 0-0.2, and A_g is geometrical constant near 1. The contribution of the surfaces to the overall resistivity becomes significant when the sample thickness is comparable to λ (for the case of copper, this occurs when w drops below $10\lambda \approx 400$ nm).

The resistivity is also sensitive to defects in the crystal (e.g. dislocations). In the case of a deformed Cu single crystal, Basinski and Saimoto [54] found that the value of resistivity per unit dislocation is in the order of 10^{-19} $\Omega.\text{cm}^3$. On the other hand, vacancies contribute to a resistivity increase of about 2.27 $\mu\Omega$.cm per atomic percent [16]. For the case of copper, and due to the low concentration of vacancies at room temperature, the contribution of vacancies to the overall resistivity is negligible [49]. Also, impurities contribute to an increase in the sample resistivity depending on their concentration. This can be up to several $\mu\Omega$.cm per atomic percent for the case of copper. The coefficient for the resistivity increase depends on the atomic size and valance of the impurity [49, 55]. For the case of electrodeposited nanocrystalline copper films that undergo self-annealing, the thickness is larger than λ (as in the case of as-deposited 1 μm-thick film). Thus, the effect of surfaces is negligible. Moreover, the concentration of organic impurities that are normally included in the electrodeposition bath is very low. This suggests that the major contribution to the high as-deposited resistivity comes from the electron scattering due to high density of grain boundaries. The decrease in resistivity during self-annealing is then mainly due to the increase in the grain size (i.e. reduction of the grain boundary area density).

2.3.1 Effect of Deposition Conditions on Self-annealing Rate

Since the microstructure and electrical resistivity affect the performance and reliability of copper interconnects, the phenomenon of self-annealing was extensively investigated in the literature [46, 56–63]. The self-annealing rate was found to be controlled by deposition conditions (i.e. deposition rate, film thickness and electrolyte recipe). Brongersma et al. [64] observed self-annealing in films produced with deposition currents > 0.75 A (on 8-in. Si(100) wafer with 150 nm-thick Cu seed layer) while no self-annealing was observed for films that were deposited at 0.3 A. With increasing the deposition current, self-annealing is accelerated as shown in Fig. 2.8. It was also observed that the extent of the incubation period depends on the deposition rate where films deposited at high current densities require less time to start self-annealing. Stangl and Militzer [65] reported a slight decrease in the resistivity during the incubation period. A similar trend can be observed from the normalized resistivity profiles shown in Fig. 2.8. To see if the current density affects the as-deposited microstructure, Lee et al. [66] measured the grain size of films deposited at different current densities and observed that the initial grain size is independent of the current density ($\approx$0.1 μm). In agreement with these observations, Stangl et al. [15] reported a constant initial grain size (90 nm) when the current density is higher than 10 mA/cm^2 for a 300 nm-thick Cu layer while films electrodeposited at current densities less than 10 mA/cm^2 showed an average grain size > 400 nm.

At a fixed deposition current density, the self-annealing rate in electrodeposited Cu films was shown to be highly dependent on film thick-

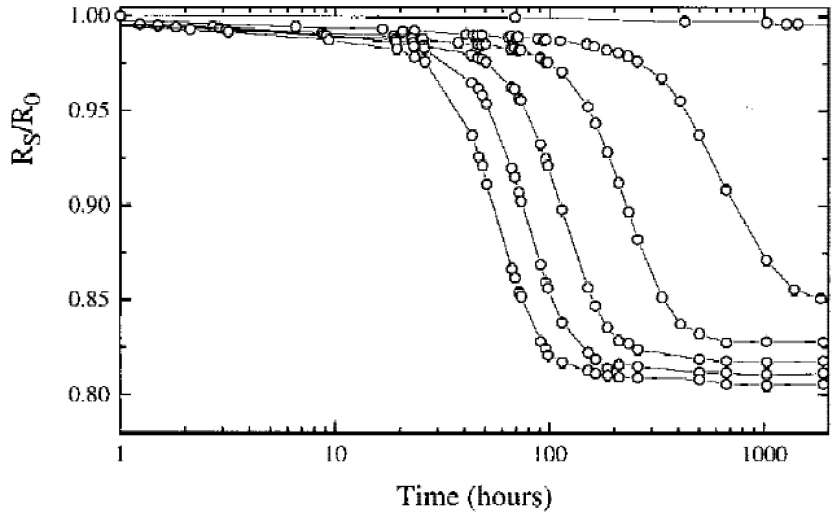

Figure 2.8: Effect of deposition current on self-annealing rates of 1.15 μm-thick Cu layer. The resistivity is normalized by the initial resistivity value. Deposition current is from left to right: 6, 4.5, 3, 1.5, 0.75 and 0.3 A. The deposition was carried on a 8-inch Si(100) wafer with 150 nm-thick Cu seed layer. [64]

ness [46, 63, 67]. Very slow or no self-annealing was observed for thicknesses below 500 nm while self-annealing is accelerated as the film thickness is increased. Little increase in the self-annealing rate was observed for films thicker than 2 µm. To some extent, these results agree with the work of Brunoldi et al. [68] who reported only 2.5% change in the resistivity of 70 nm-thick copper film after 200 hours following the deposition. In agreement with the trend in thin films, Lingk and Gross [69] reported that self-annealing occurs in Damascene narrow lines and found that the rate of the process increases as the width of the line increases.

The electrolyte chemistry has a consequence on the self-annealing rate in copper thin films. Hasegawa et al. [44] concluded that self-annealing does not

occur when no organic additives are present in the electrolyte. Films that were produced using electrolytes containing only PEG-Cl^- additives produced similar results. However when the plating electrolyte contains SPS-PEG-Cl^- additives at certain concentrations, self-annealing was observed during the first week following the deposition (see Fig. 2.9). In the absence of additives, Osaka et al. [70] did not observe significant change in the grain size in a period of 2 weeks after deposition as shown in Fig. 2.10-a. On the other hand, the grains grew by a factor of 4-5 when PEG-SPS-Cl^- additives are added to the bath as shown in Fig. 2.10-b. Although these results suggest that JGB is not necessary for self-annealing initiation, Gao [71] reported that the absence of JGB results in a very slow self-annealing. The rate of self-annealing, however, is sensitive to the concentration of the additives in the bath as reported by Ritzdorf et al. [72] who found that higher additive concentration slows down the self-annealing rate and that was attributed to the increased incorporation of impurities during deposition. In the case of Damascene copper interconnects, Neuner et. al. [73] used electron backscatter diffraction (EBSD) to quantify the effect of additive concentrations in a 72 nm-wide copper lines and found that the grain morphology is affected by increasing the additive concentrations. Thus, there is an optimal additive concentration to form a high quality film while keeping self-annealing times at a minimum.

There are evidences that the electrolyte recipe affects the electrical properties of the deposit. For example, Osaka et al. [70] found that the resistivity of the as-deposited additive-free film is lower than that when all additives are present (SPS-JGB-PEG-Cl^-) and this effect was attributed to the increased

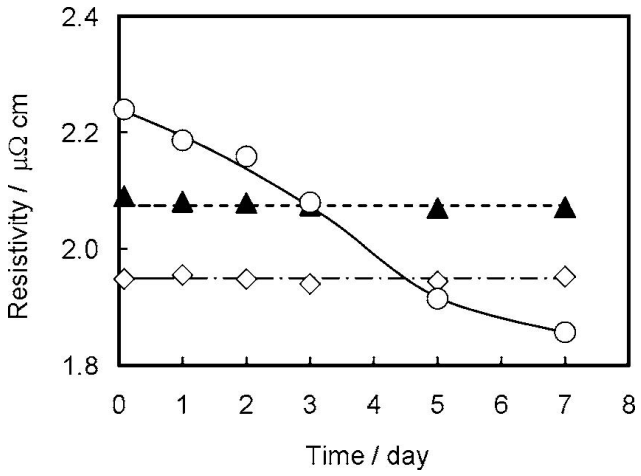

Figure 2.9: Effect of electrolyte chemistry on the self-annealing rate of 3 μm-thick film deposited at 10 mA/cm^2. The electrolyte contains (◊) no additives, (▲) PEG-Cl$^-$, (O) PEG-SPS-Cl$^-$. [44]

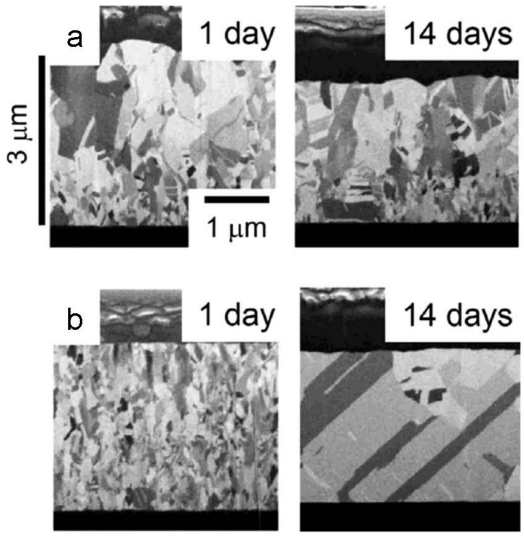

Figure 2.10: The cross-section of a 3 μm-thick copper film deposited at 10 mA/cm^2 observed 1 day and 14 days after deposition using electrolyte containing (a) additives-free, and (b) PEG-SPS-Cl$^-$. [70]

carbon concentration. This trend is also clear in the work of Hasegawa et al. [44] as can be seen in Fig. 2.9. With regard to the microstructure details, adding PEG-Cl^- only to the acidic electrolyte seems to generate twins across the film thickness. In this case, Kelly et al. [38] suggested that the deposit grows mainly via two-dimensional nucleation of macrosteps (i.e. one step over another) while a three-dimensional growth was observed when SPS was added to the electrolyte along with lower grain size and twin density. Another observation is that sulfur containing additives (e.g. SPS) produce a bright and smooth deposit. The addition of JGB to the electrolyte in the presence of the other additives produces more regular grains and significantly reduces the grain size below 100 nm without twin formation.

In addition to the electrolyte chemistry, the bath age affects the deposition quality and the subsequent self-annealing. The work of Gao [71] showed that self-annealing is significantly slowed when aged electrolyte (for few hours to few days) is used. The same conclusion was also reported by Stangl et. al. [74] where the researchers found an increase in the incorporation of impurities in films produced with aged electrolyte along with a small final grain size compared to the case when fresh electrolyte is used. The effect of aging is believed to be due to the decomposition of some organic additives in the solution (like SPS) which results in impurities that are able to pin the grain boundaries as suggested by Stangl et al. [74].

The excess copper in the overburden layer affects the self-annealing kinetics in the trench/via. Lingk and Gross [69] allowed self-annealing to occur and then studied the microstructure before and after CMP stage. They found that the self-annealing that occurred in the excess Cu layer was ex-

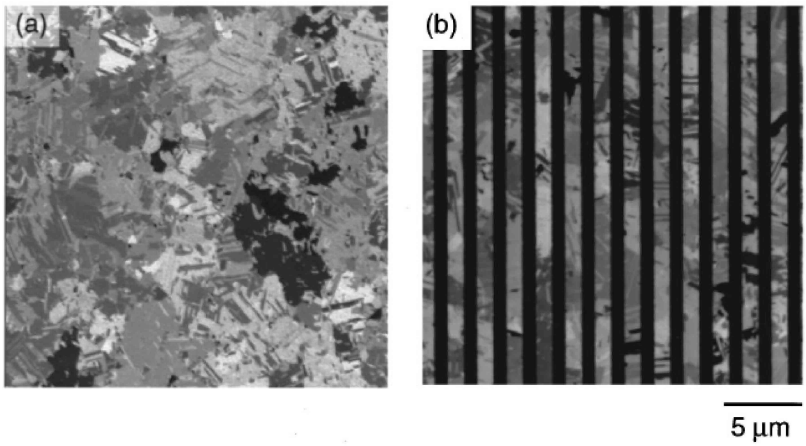

Figure 2.11: Focused ion beam (FIB) image of the microstructure of (a) 1 μm-thick Cu layer on top of Damascene trenches before applying CMP (b) Damascene trenches after CMP. The sample was stored at room temperature for 3 days (i.e. complete self-annealing was observed). [69]

tended to the trenches as shown in Fig. 2.11. However, applying CMP immediately after electrodeposition (i.e. removing the overburden layer) significantly reduces the rate of self-annealing in these trenches and incomplete self-annealing was observed even after 2 months following CMP. A similar trend was reported by Dubreuil et al. [75]. The fact that the presence of excess copper accelerates self-annealing may be related to the thickness effect discussed above. Lingk and Gross [69] concluded that the initiation of self-annealing occurs at the upper corners of the trenches due to the high stress and dislocation densities at these sites. In disagreement with Lingk and Gross [69], Neuner et al. [73] EBSD maps showed that grains in adjacent copper interconnects lines have the same orientation which suggests that self-annealing initiates in the overburden layer (not in the corners) and then proceeds to the nearby trenches and vias.

The stress relaxation that was observed by Stangl [47] seems to be affected by the deposition rate. Brongresma et al. [64] observed a change in the wafer curvature after electrodeposition (which indicates a stress evolution) and found that the deposition rate plays a role in determining the as-deposited and final stresses in the film as well as the nature of the stress (i.e. tensile or compression). Similarly, Harper et al. [49] and Stangl et al. [47] reported compressive stress while Teh et al. [46] observed a tensile stress. In addition, Lagrange et al. [67] indicated that the change in stress occurs immediately after deposition (i.e. no incubation period) and there is no correlation between resistivity and stress during self-annealing. This observation was explained by the fact that the two phenomena are not influenced by the same factors. In disagreement, Stangl et al. [47] found a reasonable correlation between stress and resistivity and discussed that the evolution of the stress can be described by two stages. During the incubation period, the first stress-relaxation stage is accompanied by hydrocarbon segregation. In this stage there is a little decrease in the film resistivity (<3%). A second stress-relaxation stage is observed where the film resistivity starts to decrease sharply (see Fig. 2.7). This stage is explained by the reduction of defects along with film densification [76]. On the other hand, Huang et al. [58] found tensile stress in all films (1.5-20 μm-thick) and a strong initial stress-thickness dependence. The researchers explained the variance in the initial stresses by 1) the longer total deposition time for thicker films allows for defects to annihilate during deposition; 2) there is some increase in the initial grain size with increasing the film thickness.

The Hall-Petch relationship relates the flow stress, σ, to the grain size by

$$\sigma = \sigma_0 + \frac{k}{\sqrt{G}} \tag{2.7}$$

where k is a proportionality constant. This model predicts that increasing the grain size decreases the flow stress in a film of a defined thickness. Read et al. [77] performed force probe microtensile test and found that the stress-strain curve of the electrodeposited Cu film agrees with the Hall-Petch relationship. However, the Young's modulus was found to be less than its value for bulk copper.

In the literature, there was a general trend to describe self-annealing using the conventional processes and terminologies that are used to describe the microstructure evolution in deformed metals and alloys subjected to annealing treatment. These mechanisms include recovery, recrystallization and grain growth. Since these terms are proposed in the literature to describe self-annealing, it is useful to provide a brief review for each one of them.

2.3.2 Microstructure Evolution Mechanisms

Recovery

When a polycrystalline material is cold-worked, the grains become elongated and a fraction of the deformation energy is stored in these grains in the form of dislocations and point defects. As a consequence, there is a driving pressure in the microstructure to release this excess energy and return to its original state before deformation. The dislocations in the microstructure can rearrange and annihilate after deformation which reduces some of the overall stored energy. This process is called recovery and its extent depends

on many parameters including the level of the deformation strain and the nature of the material itself (i.e. stacking fault energy). Moreover, higher annealing temperature promotes recovery by accelerating the movement and annihilation of dislocations. The recovery stage imposes some consequences on the mechanical properties like yield stress and hardness. Also, changes in electrical resistivity after deformation may correlate with recovery [78]. As indicated in the Matthiessen's rule, the resistivity of a material is affected by the presence of a high density of dislocations and defects. The annihilation of some of these dislocations during recovery reduces the total electron scattering. Recovery may not be easily observed using techniques like optical microscopy, and tracking the mechanical and electrical properties can provide indirect estimation of the process rate. In some cases, however, the change in these material properties due to recovery is small. Differential scanning calorimetry (DSC) is frequently used to quantify recovery where a distinct small peak in the released heat profile can be associated with recovery [78, 79]. The recovery stage eventually leads to a subgrain formation (i.e. low angle grain boundaries) and occurs prior to the recrystallization stage which is discussed below.

Recrystallization

The recrystallization process involves forming dislocation-free nuclei in the deformed grains that grow to consume the microstructure. The recrystallized grains are surrounded by high angle grain boundaries. The driving pressure for recrystallization is to minimize the stored energy within the deformed grains. The driving pressure, ΔP, due to dislocation density, Γ, can be

expressed as

$$\Delta P = 0.5\mu b_v^2 \Gamma \tag{2.8}$$

where b_v is the magnitude of the Burger's vector and μ is the shear modulus. The velocity of the recrystallized boundary, v, is a function of ΔP and the mobility of the boundary, M, i.e.:

$$v = M\Delta P \tag{2.9}$$

The mobility of the boundary is frequently described by an Arrhenius relationship, i.e.

$$M = M_o \exp\left(\frac{Q}{k_B T}\right) \tag{2.10}$$

here, M_o is a pre-exponential constant and Q is the activation energy. Thus, recrystallization occurs faster at high temperature and for heavily deformed microstructures in which a high driving pressure due to dislocations is present. Also, for the same driving pressure, boundaries with high mobilities will move faster than those with lower mobilities. The mobility term can not be easily measured. However, Vandermeer et al. [80] measured the stored energy in cold worked copper using calorimetry analysis. The researchers then measured the average interface velocity during recrystallization at 121 °C and found that the relationship between the two quantities obeys Eq. 2.9. The estimated mobility at this temperature was 6.31 $\times 10^{-8}$ cm^4/Js. For recrystallization to occur, however, a minimum deformation level is required (i.e. critical strain) [78]. Normally, the nucleation initiates at some preferred sites

in the microstructure (e.g. grain boundaries) and, for a stable nucleus to form, the driving pressure must be greater than the retarding pressure that originates from the curvature of the boundary. Thus, there is a critical nucleus radius below which the nuclei are unstable and will not grow.

The fraction recrystallized describes the volume fraction of the recrystallized grains in the material with respect to the overall volume (i.e. $0<f<1$) and can be quantified using characterization tools like EBSD [81], FIB [82] and transmission electron microscopy (TEM) [83]. In-situ EBSD experiments were performed by Wright and Nowell [84] on cold worked copper subjected to annealing treatment (160 ℃). By analyzing the orientation maps, the researchers were able to observe the different stages of recrystallization (see Fig. 2.12). Using a similar approach, local orientation spread maps were used [85] to locate and identify recrystallized grains as shown in Fig. 2.13. The local orientation spread measures the deviation from the average orientation of a group of scan points (3^{rd} neighbor points are normally considered). The recrystallized grains appear in blue with local orientation spread values $< 1^{\circ}$ which indicates low dislocation density. In agreement with Wright and Nowell [84], Field et al. [81] showed that deformed pure copper (99.99%) can recrystallize at temperatures between 155 ℃ and 200 ℃. In addition to techniques like EBSD, other indirect characterization tools are frequently employed for recrystallization assessment. For example, electrical resistivity [86] and microhardness [87] were used to quantify the recrystallization of cold worked copper and its alloys as a function of annealing temperature.

The recrystallization rate and the details of the final microstructure depend on many parameters including the level of deformation, prior grain size,

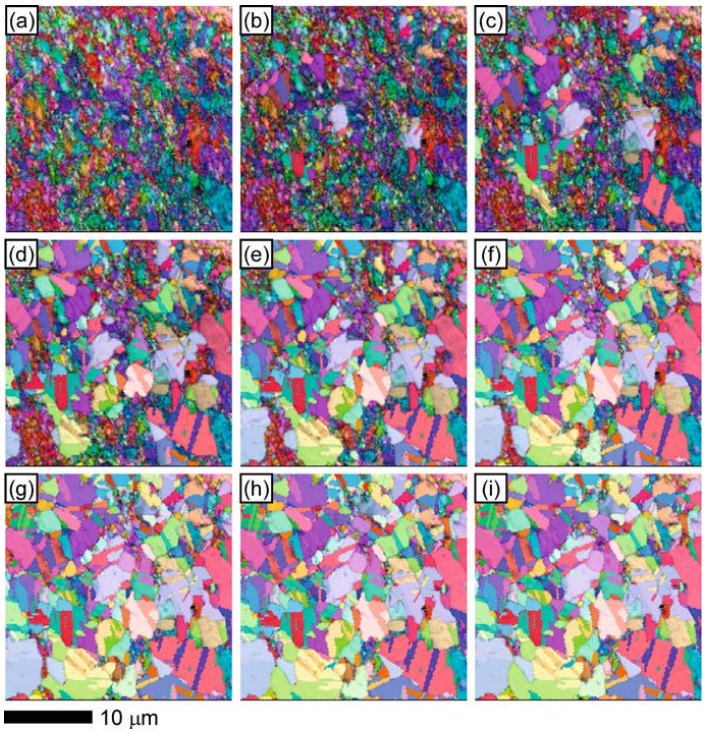

Figure 2.12: In-situ EBSD maps showing the progress of recrystallization in deformed pure copper at 160 °C at different times. [85]

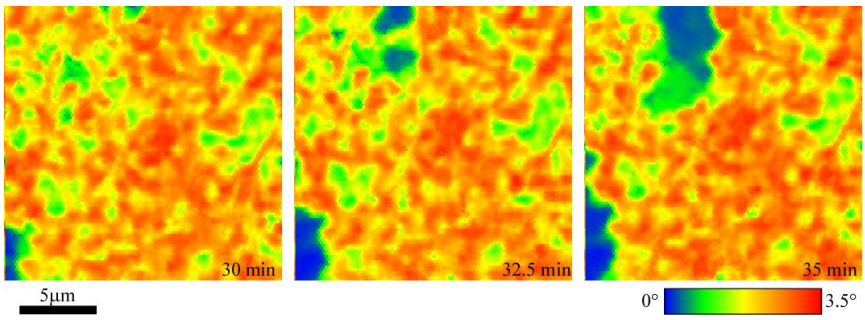

Figure 2.13: Assessment of the initial stage of recrystallization using local orientation spread maps. [84]

orientation, temperature, and the nucleation scenario [78]. For example, a small initial grain size will result in more nucleation sites compared with the case of large initial grain size. On the other hand, higher annealing temperature influences the recrystallization rate by promoting the nucleation and growth processes and, thus, the time required to achieve a fully recrystallized microstructure is shorter at higher temperatures. When comparing different recrystallization profiles that are obtained during isothermal heat treatment, it is convenient to use the time for 50% recrystallization ($t_{50\%}$) as a criterion for comparison. The temperature dependence of $t_{50\%}$ is frequently described by

$$t_{50\%} = C \exp\left(\frac{Q}{k_B T}\right) \tag{2.11}$$

where C is a constant and Q is the activation energy for recrystallization.

Grain Growth

Following recrystallization, the system will continue to evolve to reduce the total grain boundary area. This process leads to a coarse grain size and is referred to as grain growth. It is observed after recrystallization but grain growth is also common without a preceding recrystallization stage. The driving pressure for grain growth is much less than that for recrystallization (typically two orders of magnitude lower) and can be expressed by

$$\Delta P = 2\frac{\gamma_{gb}}{r} \tag{2.12}$$

where γ_{gb} is the grain boundary energy per unit area and r is the grain

radius. For the case of nanocrystalline copper ($r = 50$ nm), $\Delta P \approx 20$ J/cm^3 is obtained [88]. The evolution of average grain size during ideal grain growth follows a parabolic relationship with time, i.e.:

$$r^2 - r_0^2 = ct \tag{2.13}$$

where r_0 is the initial average radius and t is the time. However, ideal grain growth is almost never observed experimentally. The presence of particles and solutes can retard grain growth. Due to their interaction with the grain boundary, second phase particles can pin the boundaries and reduce the total driving pressure. The velocity of the boundary during grain growth in the presence of these particles can be expressed as

$$v = M.(P - P_z) = M.\left(\frac{2\gamma_{gb}}{r} - \frac{3F_v\gamma_{gb}}{2r_p}\right) \tag{2.14}$$

where F_v and r_p are the volume fraction and radius of the particles [78, 89]. As a consequence, particle pinning can limit the final grain size (i.e. the case when $v = 0$).

Similar to recrystallization, grain growth is observed experimentally at sufficiently high temperature, this is because, at low temperatures, the rate of grain growth is very low. Humphreys and Hatherly [78] pointed out that the rate of grain growth depends on the size of the sample. For the case of thin films, the growth stagnates when the growing grains become comparable or exceeding the film thickness (i.e. columnar grains).

In some cases, some grains in the microstructure have an advantage to grow at a rate higher than other grains. This will lead to abnormal grain

growth which is sometimes referred to as secondary recrystallization. The result of abnormal grain growth is a bimodal distribution in the grain size. The driving pressure for abnormal grain growth is the same as for normal grain growth (i.e. reduction of grain boundary area). However, higher mobility of some of these boundaries can be responsible for abnormal growth. It is indicated that abnormal grain growth may occur in highly textured materials where many grain boundaries have low energies [78]. In this case, other grains with some different random orientations (i.e. high angle grain boundary) will have the advantage to grow due to their boundary mobility advantage. On the other hand, particle pinning of grain boundaries may also contribute to abnormal grain growth where some particle-free boundaries may move rapidly such that many small grains are consumed. Some additional driving pressure may also contribute to nonclassical abnormal grain growth (e.g. due to minimization of strain energy and/or surface energy [88]). In this regard, Zhang et al. [90] claimed that strain-energy-driven abnormal grain growth occurs in Cu thin films on Si substrates.

2.3.3 Mechanism of Self-annealing

In the light of the above processes, several mechanisms were proposed to explain the driving pressure for self-annealing. Fukumuro et al. [91] used thermal desorption spectroscopy of hydrogen and found extremely high concentration of vacancy-hydrogen clusters in the as-deposited microstructure. These vacancy clusters decrease with time after deposition concurrently with grain growth. The researchers then suggested that self-annealing is caused by hydrogen induced superabundant vacancies. On the other hand, Harper

et al. [49] suggested that the grain boundaries are initially pinned by impurities. During the incubation period, these impurities start to coalesce which eventually frees some grain boundaries. As a result, some grains grow abnormally at the expense of the small grains in the film and in this way the reduction of grain boundary area is the driving pressure that accounts for the observed drop in resistivity. A similar theory was proposed by Hau-Riege and Thompson [92] who considered that the 3D grain growth is impaired by solute drag, and impurities play a crucial role in abnormal grain growth in Cu thin films. The researchers claimed that the rejection of impurities to the untransformed grains during growth contributes to the observed abnormality. Based on their TEM observations, a different explanation about the role of impurities was proposed by Paik et al. [62] who considered that the impurities that are incorporated in the film during the deposition may result in a strong anisotropy of grain boundary energies. The researchers proposed that this anisotropy is then responsible for the observed abnormal grain growth. Lee and Park [93] suggested that locally applied high stress originated from trapped PEG at the grain boundary is the driving pressure for self-annealing. According to this assumption, grain growth occurs after the stress is decreased due to the decomposition of PEG molecules. However, these mechanisms were not capable of explaining self-annealing in copper thin films deposited by PVD/sputtering [94–96]. Moreover, the work of Yoon et al. [61] on the distribution of impurities during self-annealing revealed that the impurities are redistributed in the film due to grain growth but this redistribution is not responsible for triggering self-annealing itself. They concluded that the impurities do not have sufficient kinetic energy at

room temperature and spontaneous diffusion of impurities is not likely the driving pressure for self-annealing. The fact that high electrodeposition current density accelerates self-annealing was explained, according to Chen et al. [97], by the high nucleation of copper grains during deposition at high current density which results in a higher total grain boundary energy that drives self-annealing.

Using the mobility value reported by Vandermeer et al. [80] at 121 °C and by applying Eq. 2.10, Detavernier et al. [88] estimated the mobility of the Cu grain boundaries at room temperature and were able to calculate the driving pressure for self-annealing, ΔP, assuming the velocity of the grain boundary, v , is 0.1 μm/hour, and by applying Eq. 2.9, concluded that a driving pressure $>$ 100 J/cm^3 is required to account for this speed. This pressure is much higher than the driving pressure for grain growth (i.e. grain boundary area reduction) estimated to be in the range of 10-20 J/cm^3. However, the estimated driving pressure was comparable to the stored energy due to dislocations (Eq. 2.8). Lee et al. [66] were able to provide an experimental evidence to support the Detavernier et al. [88] argument by observing dislocation loops in copper thin films prior to self-annealing using TEM as shown in Fig. 2.14. The researchers found an average loop radius of 5 nm which is independent of the deposition current density. Interestingly, the dislocation loop density scales with deposition current density which could provide an explanation why self-annealing rates are accelerated after high current density deposition. By counting the dislocations loops inside the grains shown in the TEM image, the researchers estimated the dislocation loop density to be 10^{17}-10^{19} loops/cm^3 which corresponds to a driving pressure in the

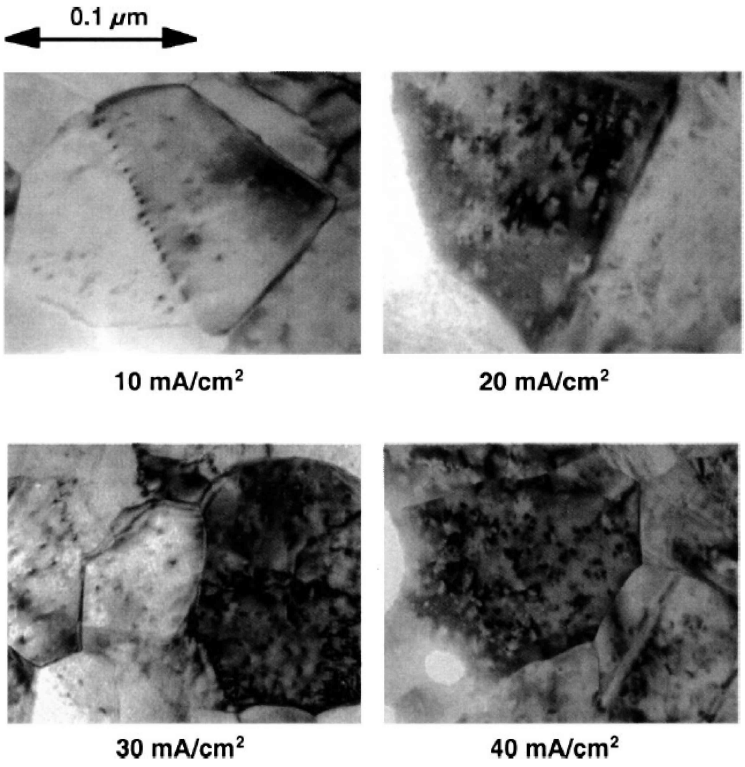

Figure 2.14: TEM images of dislocation loops in electrodeposited copper films prior to self-annealing. [66]

range of 3-300 J/cm^3 (i.e. according to the researchers, self-annealing is a recrystallization process). The time to complete self-annealing based on this estimation was approximated between 28 and 590 hours which compares well with the experimental results obtained from resistivity measurements. The researchers proposed that the self-annealing rate can be calculated by adding the stored energy due to dislocations to the driving pressure for grain growth and the velocity of the grain boundary during self-annealing can be described by

$$v = \frac{2D_{gb}\Omega}{k_B T\delta}\left[\frac{2\gamma_{gb}}{G} + 2\pi r_d \frac{\mu b_v^2}{4\pi\left(1-\nu\right)} \ln\left(\frac{r_d}{b_v}\right)\Gamma\right] \tag{2.15}$$

where Ω is the atomic volume, D_{gb} is the grain boundary diffusion coefficient, ν is Poisson's ratio, δ is the atomic jump distance in the boundary, and r_d is the dislocation loop radius. The estimation of the driving pressure that accounts for self-annealing in the work of Lee et al. [66] is in a reasonable agreement with the calculation of Detavernier et al. [88] based on the mobility-velocity approach (ΔP=392 J/cm^3). The stored energy values that were reported by Lee et. al. [66] are based on a rough estimation of the dislocation density (this method may be sensitive to the sample preparation procedure). No other evidence of high density of dislocations in the as-deposited microstructure seems to be available in the literature.

Abnormal grain growth is still widely used as a term to describe the microstructure evolution in copper. In this regard, Chen et al. [98] found (220) abnormal grain growth during copper wafer bonding and annealing and that was attributed to the minimization of surface or strain energy. Militzer et al. [99] explained the observed abnormal grain growth in Cu thin films

by the fact that desorption of the organic additives increases the mobility of grain boundaries. According to the researchers, the onset of this process is attributed to the low concentration of additives (i.e. an incomplete coverage of all grain boundaries).

On the other hand, it seems that there is an agreement in the literature that recovery provides the best interpretation for the slight decrease in the resistivity during the incubation period [65,100–102]. Regarding the slow self-annealing rate in thinner films, Lagrange et al. [67] explained that this is due to the physical restrictions when the recrystallized grains become comparable to the film thickness forcing a 2D growth .

2.3.4 Effect of Annealing on the Recrystallization Rate of Copper Interconnects

Although self-annealing occurs at room temperature, the transformation rate is significantly increased when the film is subjected to an annealing stage. The work done by Jiang and Thomas [103] on blanket films showed that, by annealing at moderate temperatures (17-80 °C), the transformation rate increases. About 10 minutes are sufficient to complete the transformation at 80 °C while about a week is required to achieve the same level at 17 °C. The final resistivity, however, was found to be independent of the annealing temperature in this range, as shown in Fig. 2.15, where about 18.2% drop in the resistivity is observed in all temperature profiles. Although thin Cu films showed no or slow recrystallization at room temperature, Hau-Reige and Thomson [92] were able to observe the start of recrystallization in a 300 nm-thick film annealed at relatively low temperature (55 °C, 12 minutes

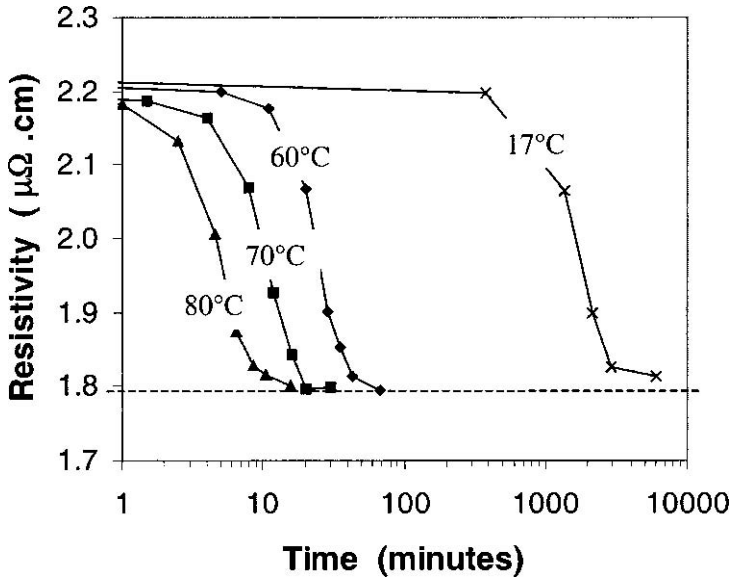

Figure 2.15: Resistivity of a 1.6 µm-thick blanket Cu film annealed at different temperatures. [103]

holding time) and, using in-situ TEM, were able to observe almost complete recrystallization within 1 hour of annealing treatment as shown in Fig. 2.16. Subsequent annealing at 200 °C and 300 °C produced complete recrystallization. In comparison, the researchers observed only a partially recrystallized microstructure at room temperature even after 80 hours following the deposition. The almost completely recrystallized microstructure of 300 nm-thick film after 1 hour of annealing at 55 °C is surprising when compared with the resistivity profile of 1.6 μm-thick film at 60 °C in the work of Jiang and Thomas [103]. One would expect that thinner films will take much longer time to recrystallize at the same annealing temperature. The fact that different electrolytes containing different proprietary additives were used in these two studies may account for this inconsistency.

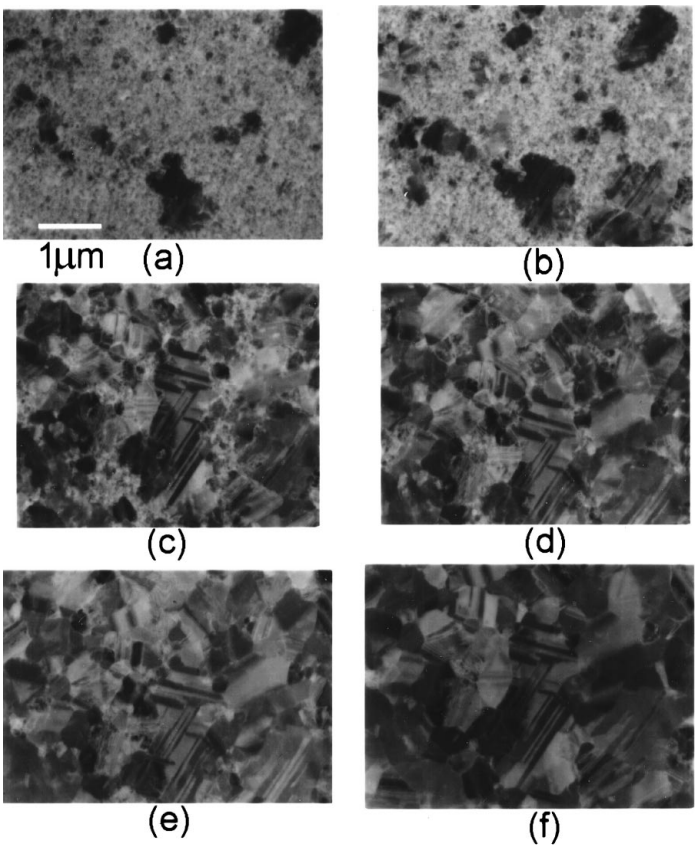

Figure 2.16: Effect of annealing on the microstructure of 300 nm-thick Cu film annealed at 55 °C for (a) 5 min (b) 12 min (c) 49 min (d) 1 hour. The images in (e) and (f) are after subsequent annealing for 10 min at 200 °C and 300 °C, respectively. [92]

The effect of temperature on accelerating the transformation rate can be explained by the fact that the mobility of grain boundaries, nucleation and the subsequent growth are all dependent on the annealing temperature. The fact that the resistivity is not a function of annealing temperature suggests that the annealing treatment produces a final microstructure with a big grain size that is sufficient to represent the bulk resistivity of copper (i.e. grain size $>$ 1 µm). On the other hand, the work of Kang et al. [104] on 500 nm-thick copper film subjected to isothermal annealing treatment (200, 300 and 400 ℃ for 30 min holding time) revealed changes in film resistivity, hardness, roughness and grain size. The researchers found that the change in the resistivity after annealing is higher than that at room temperature. Only 14% resistivity drop was measured for self-annealed film (2000 hours after deposition) while annealing produced a change that is between 18% and 19%.

Regarding the mechanical properties, nanoindentation experiments of Kang et al. [104] revealed a decrease in the film hardness from 2.9 GPa (as-deposited) to 1.9 GPa after annealing (400 ℃ for 30 min). The researchers used scanning electron microscope (SEM) to observe the changes in the microstructure after annealing and an increase in the mean grain diameter was observed with increasing the annealing temperature and being 1.81, 1.96 and 2.15 μm for annealing temperature of 200, 300 and 400 ℃, respectively. Carreau et al. [105] studied the effect of annealing temperature on the resistivity of the electrodeposited trenches and thin films. The researchers observed a lower resistivity upon annealing of 300 nm-wide trenches. For the case of thin films, annealing at 400 ℃ for 6 hours of 130 nm-thick Cu layer elec-

trodeposited on 150 nm TaN/Ta barrier layer produced a 500±300 nm grain size while a 700 nm-thick Cu layer produced an average grain size which is 6 times bigger. Similar observations were obtained by Brunoldi et al [68]. By combining the grain size results of Carreau et al. [105] and Kang et al. [104], it is clear that the grain size evolution depends on the film thickness even at high temperature. This suggests that the optimum annealing temperature depends on the geometry and higher annealing temperature is required to increase the final grain size of the microstructure.

Since recrystallization in copper interconnects appears to be a thermally activated process, the activation energy for this phenomenon can be determined. In this direction, Donthu et al. [106] and Yin et al. [57] used DSC to study the recrystallization kinetics in Cu thin films. Normally, an exothermal peak is observed in systems that contain excess energy due to deformation (i.e. stored energy due to dislocations). Kissinger's analysis is commonly applied to calculate the activation energy , Q_e, [107] where:

$$\ln \frac{\beta}{T_p^2} = -\frac{Q_e}{k_B T_p} + C \tag{2.16}$$

where C is a constant, β is the heating rate, and T_p is the temperature at which the exothermal peak in the DSC profile is observed. Using this technique, Yin et al. [57] found that the activation energy for recrystallization in copper interconnects is 0.85 eV. This is comparable with the activation energy for grain boundary diffusion in copper which is estimated to be 0.92 eV [108]. However, there is some discrepancy in the activation energy in the literature and values in the range between 0.62-1.18 eV were reported [88, 93, 103, 106]. This maybe due to the different electrolyte chemistry that is employed in

these independent studies which may play a role in determining the transformation temperature. Although the transformation kinetics for thin lines is much slower than that for thin films due to the physical constraints and 2D growth, Jiang and Thomas [103] found that the activation energy is independent of the geometry of the Damascene lines or film thickness. This suggests that the activation energy for the microstructure evolution in Cu thin films is a characteristic of the interconnect material itself.

2.4 Modelling of Microstructure Evolution in Cu Interconnects

Modelling of the microstructure evolution in copper interconnects is necessary to aid understanding of self-annealing where the changes that occur in the resistivity and the related microstructure details can be predicted. There were some attempts in the literature to model the self-annealing phenomenon as a function of the time after deposition and accounting for the effect of deposition conditions (i.e. current density, film thickness, and additives concentration). The models are based on data obtained using different characterization tools (i.e. resistivity, X-ray diffraction (XRD), FIB and TEM). Since self-annealing appears to be a recrystallization phenomenon, there is an agreement in the literature to model self-annealing based on the existing recrystallization models that describe the microstructure evolution processes in deformed metals and alloys. The rule of mixtures is frequently used to obtain the fraction recrystallized, f, from resistivity data, i.e.

$$f = \frac{\rho_0 - \rho}{\rho_0 - \rho_\infty} \tag{2.17}$$

Here, ρ_0 is the as-deposited resistivity, ρ_∞ is the final resistivity and ρ is the resistivity at any time. Stangl and Militzer [65] proposed an improved resistivity model to account for the high conductivity paths through connected large grains in the microstructure where the fraction recrystallized is obtained from

$$\frac{1}{\rho_n} = \frac{1 - f^2}{\rho_\infty f + \rho_{inc}\,(1 - f)} + \frac{f^2}{\rho_\infty} \tag{2.18}$$

where ρ_n is the normalized resistivity and ρ_{inc} is the resistivity during the incubation period. The researchers developed a phenomenological model to describe self-annealing in electrodeposited Cu thin films using the Johnson-Mehl-Avrami-Kolmogorov (JMAK) model where the fraction recrystallized can be described as [78, 109]

$$f = 1 - \exp\left(-bt^n\right) \tag{2.19}$$

Here, t is the time after deposition, b is a term that depends on the nucleation and growth rate of the recrystallized grains and n (Avrami exponent) indicates the nucleation conditions and the dimension of growth. By rearranging the JMAK equation, the value of n can be obtained where

$$\ln\left(\ln\frac{1}{1 - f}\right) = n \ln t + \ln b \tag{2.20}$$

In this way, the value of n can be calculated from the slope of the linear

curve that represents Eq. 2.20 where the value of f is obtained using a suitable characterization tool. The value of n is normally used to indicate the dimensionality of growth and nucleation mechanism. For example, when the number of the nuclei is fixed (i.e. site saturation nucleation), the case of n=3 represents a growth in 3D. The value of n is less when the growth is limited to 2D or 1D (n=2 and n=1, respectively). On the other hand, when the nucleation rate is constant, the value of n will be 4, 3 and 2 for 3D, 2D and 1D growth, respectively. As observed experimentally, the value of n falls between the above limits. For example, Ying et al [56] used the JMAK model to describe their in-situ XRD texture evolution during self-annealing. The researchers monitored the time variation in the (111) peak position, breadth and intensity and were able to calculate the recrystallized volume fraction and found that the Avrami exponent is less than 1.9. The low value of n can be due to the heterogeneous distribution of the stored energy in the microstructure [78]. To see if the JMAK model can be used to describe the microstructure evolution in Damascene trenches, Lingk and Gross [69] modelled the fraction recrystallized that was obtained using FIB experiments and the researchers showed that the JMAK model can describe self-annealing in these narrow lines. Donthu et al. [106] observed the microstructure during self-annealing and found that the number of nuclei are fixed which suggests site saturation nucleation mechanism. Stangl and Militzer [65] assumed that the grain boundary mobility and the driving pressure for recrystallization are time independent and the growth is considered to be in three dimensions assuming nucleation site saturation. The Stangl-Militzer model proposed phenomenological relations between the current density and

Table 2.2: A survey of Avrami exponent values that are available in the literature.

Reference	n	Thickness (µm)	Technique
Brongersma et al. [110]	1-3	0.65 <d< 3.15	Resistivity
Hau-Riege and Thompson [92]	1.0	0.3	TEM
Udeno et al. [111]	3.23, 4.2	1, 2	positron beam
Stangl and Militzer [65]	1.6	1	Resistivity
Pantleon and Somers [112]	3-4	1.5 <d< 5	XRD
Ying et al. [56]	1.56-1.89	0.4-1	XRD
Yin et al. [57]	3.54	18	FIB
Walther et al. [113]	2-7	0.5 <d<5	FIB
	0.5-4	0.5 <d<5	Resistivity

both the incubation period and the time for 50% recrystallization. The model prediction of the normalized resistivity profiles as a function of time after deposition agrees well with the experimental measurement where the actual driving pressure for recrystallization is assumed to be given by a distribution in the dislocation density.

Although there was a reported agreement between the experimental results and the developed models in the above studies, there is a significant discrepancy in the values of n that are available in the literature. Some of the results are summarized in Table. 2.2. For example, for 1 μm-thick films, values of 1.6 and 3.23 were reported. Moreover, and for the same deposition conditions, Walther et al. [113] found a difference in n value that was obtained from different characterization tools (here, resistivity and FIB). The reason for the unexpected value of $n = 7$ that was obtained by FIB for the 5 μm-thick film is not quite clear. The researchers concluded that self-annealing is too complex to be described with the JMAK approach. It may be possible, however, that some additional driving force is supplied during

FIB imaging and sample preparation which is not the case during resistivity probing. Moreover, a different electrolyte recipe in these studies may be responsible about the wide scatter in the value of the Avrami exponent.

2.5 Current Trends in Interconnects Research

2.5.1 Novel Deposition Strategies

In the advanced integrated circuits with 22 nm technology node and below, superfilling of vias and trenches becomes a significant challenge. In addition, the increase in resistivity due to sidewalls and reliability concerns in terms of electromigration become magnified. Hence, there is a trend to design novel deposition strategies that enhance the microstructure of copper interconnects. Some studies aim to synthesize deposition strategies that will lead to a different initial microstructure with enhanced properties. In this direction, Chen et al. [97] proposed a deposition strategy that consists of 3 stages. In each stage, a different deposition current density is used while switching the deposition on and off in the third stage. The researcher discussed that this strategy produced an accumulation of big and small grain sizes which, after the annealing cycle, reduces the residual stresses and void formation and improves the interface packaging density of Cu interconnects.

There is another direction which is focused on synthesizing Cu microstructure with high nanotwin density. To produce a nanotwinned microstructure, pulse electrodeposition is frequently used instead of direct current (DC) de-

position. Xu et al. [114] proposed that the nanotwins form due to stress and stress relaxation that occurs during pulse on and pulse off. In another work, Xu et al. [115] studied nanotwin formation using TEM, in-situ stress measurement and EBSD and found that high density of nanotwins produced by pulse electrodeposition improves the mechanical properties. From their EBSD results, pulse-electrodeposited films appear to have bigger grain sizes compared to DC electrodeposited films. The researchers claimed that nanotwins reduce the strain energy in the microstructure while improving thermal stability compared with fine-grained DC electrodeposited copper. Lu et al. [116] found that nanotwins prefer to nucleate near grain boundaries to reduce the total energy. The researchers also found that the distance between the nanotwins is affected by the deposition parameters like current density, time on and time off duration and temperature. An important finding in the researchers work is that nanotwins do not have significant influence on the electrical resistivity of Cu thin films. Liu et al. [117] showed that the intensity of the preferred texture, grain size and the fraction of the twins is reduced as the deposition current is increased.

2.5.2 Silver and Copper-Silver Alloying

Silver (Ag) has attracted increasing attention recently as a potential interconnect material. As can be seen from the comparison presented in Table 2.1, silver has the lowest resistivity of all metals at room temperature. Given the poor electromigration resistance of silver compared to copper, the gain in conductivity (around 5%) is not so significant to justify the replacement of copper with silver. However, as the technology node drops below the mean

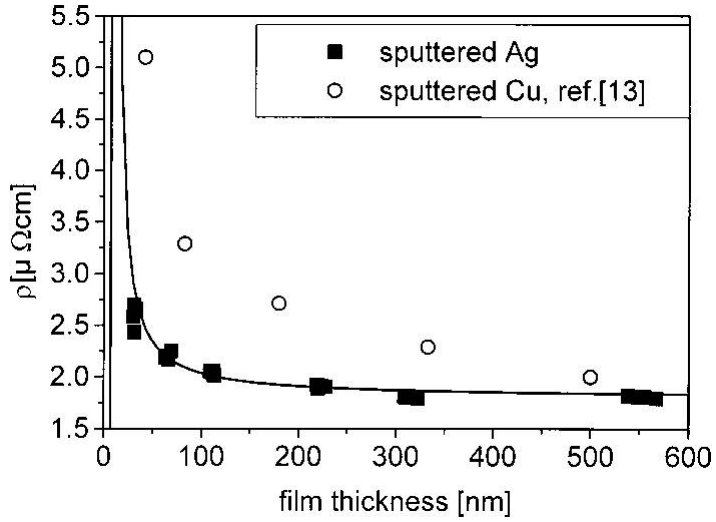

Figure 2.17: Comparison between the resistivity of sputtered Ag and Cu films as a function of film thickness. [118]

free path of electrons, the increase in resistivity of silver interconnects is much less than that in the case of copper interconnects. As shown in Fig. 2.17, the resistivity of sputtered Ag films can be 100% less than that in the case of copper at the same film thickness. One of the main reasons for this is the difference in the average grain size, mean free path and grain boundary reflection coefficient between both materials [32, 37].

If silver needs to be the next material for interconnects employing the same metallization process that is currently in place for copper, a good superfilling of silver in deep trenches is required. Moffat et al. [32] were able to prove that silver superfilling by electrodeposition can be achieved. The researchers used commercial electrolyte containing 0.34 mol/L KAg(CN)2 and 2.3 mol/L KCN and two additional proprietary additives (i.e. surfactant and brightener or catalyst). To investigate silver recrystallization (i.e. self-

annealing), the researchers prepared a 1 µm-thick silver film grown electrochemically (at 10 mA/cm^2) on a 100 nm-thick copper seed-layer supported on silicon (100) wafers with a 2.5 nm-thick chromium adhesion layer. From resistance measurements, a 1.8% resistivity drop was observed in 2 days but no further change was noticed thereafter. However, the researchers found that recrystallization can be induced by modest annealing temperatures (even during SEM or TEM sample preparation) where the resistivity change can reach up to 10%. The fact that silver also shows some degree of self-annealing suggests that this process is not exclusively a copper phenomenon. In agreement with Moffat et al. [32], self-annealing in silver thin film was also reported by Hansen and Pantleon [119] and Pantleon and Somers [112]. Using the XRD technique, it was found that the as-deposited silver film has a slight preferred texture orientation, but it then undergoes a strong texture evolution after a short incubation period. Considerable (111) grain growth was observed compared to slight growth of (200) oriented grains. Grains of (111) orientation can grow to more than 200 nm during self-annealing. The researchers also claimed that the kinetics of self-annealing depends on film thickness but no experimental evidence was presented. Pantleon and Somers [112] proposed that nucleation, recrystallization and growth can be also used to describe silver self-annealing. On the other hand, the researchers did not observe self-annealing in nickel electrodeposited thin films and only normal grain growth was evident at elevated temperature.

In light of the rapid resistivity increase of copper interconnects in submicron features and the increase in electromigration-induced failure, copper alloying with silver attracted increasing attention recently because of the

possibility to combine two desired features: low resistivity and high electromigration resistance while enhancing the mechanical strength of the interconnect. Also, it was found that copper alloying with silver can significantly improve the reliability when used as a seed layer as proven by the work of Isobayashi et al. [120]. Specifically, Cu-Ag alloys produce less resistivity rise and greater suppression of stress induced voiding when compared to pure Cu. It was also reported that silver precipitates and releases energy during annealing which can enhance the copper grain growth [121]. On the other hand, there is an effect of silver on the microstructure of electrodeposited Cu films. From the work of Strehle et al. [122] on the microstructure of the Cu-Ag alloy, several observations can be made: the mean grain size was not only dependent on the Ag content (0-4 at%) but also on the plating current density (5-30 mA/cm^2). Also, the film roughness was found to undergo significant changes with increasing silver content. On the other hand, the work of Isobayashi et al. [120] revealed that Cu-Ag grain size is lower than that of pure copper suggesting a potential pinning effect of silver atoms on the grain boundaries. This is in agreement with the work of Shao et al. [123] who used in-situ SEM characterization of Cu-Ag co-deposition and found that Ag in the electrolyte bath acts as grain refiner as shown in Fig. 2.18. Strehle et al. [122, 124] did not observe self-annealing in Cu-Ag electrodeposited thin films but this was attributed to the absence of additives and the effect of silver on grain boundary motion.

Additives also play a role in improving the reliability of the Cu-Ag system. It was found that incorporation of impurities (like sulfur) can enhance the electromigration resistance of the Cu-Ag system. Strehle et al. [125] used an

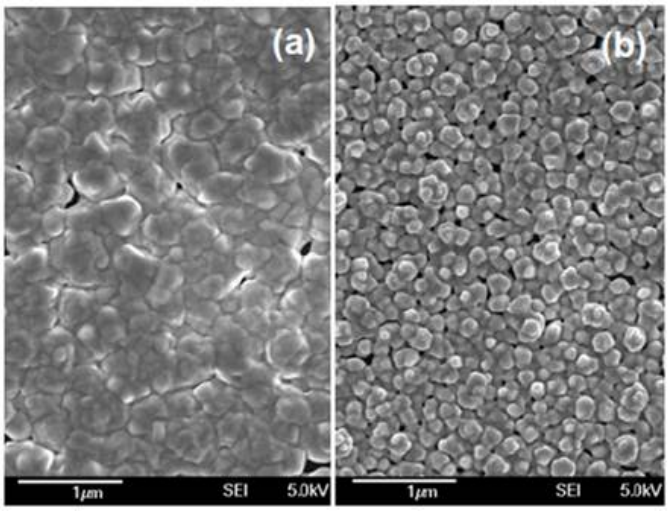

Figure 2.18: SEM image of as-deposited films that were produced using: (a) Acidic sulfate electrolyte (b) 0.1 mM $AgNO_3$ added to the acidic sulfate electrolyte. [123]

electrolyte solution containing $CuSO_4$, H_2SO_4, $AgNO_3$ and sulfur-containing additives for copper-silver deposition. The researchers avoided the use of chloride in order to prevent AgCl precipitation. An investigation of 1 µm-thick film revealed that sulfur is present in low concentrations in the form of CuxS compounds. To investigate the effect of silver on the stress-temperature behavior of Cu films, Menzel et al. [126] used sensitive laser-optical determination of the substrate curvature and found that Ag content significantly affects the stress-temperature profile. In light of the low solubility of Ag in Cu, the researchers suggested that silver atoms segregate to the surfaces and the grain boundaries. Ko et al. [121] suggested that silver precipitates in the grains and then diffuses to grain boundaries during annealing. A strong influence of the annealing temperature (25-600 °C) and film thickness (50-900 nm-thick) on the resistivity was also observed. Significant effect of annealing

on the microstructure evolution (i.e. grain size) of Cu-Ag films was reported along with 21-24% change in resistivity [122].

2.6 Summary of Literature Review

Based on the review that was presented above, some conclusions can be made. There is some evidence that a high density of dislocations in the as-deposited microstructure may play a role in driving self-annealing. Nevertheless, there is still a strong debate about the driving pressure for this phenomenon. There are some attempts in the literature to describe self-annealing using conventional recrystallization and recovery processes. In the reminder of this thesis, and while acknowledging the fact that there exists no clear conclusion regarding the actual driving pressure of self-annealing, recrystallization will be used as a terminology to describe this phenomenon. The self-annealing was also observed in sputtered copper films suggesting no significant role for impurities in driving self-annealing. The recrystallization rate is highly influenced by the deposition conditions and the process is accelerated with increasing temperature. The JMAK model is suitable to describe the self-annealing rate (with some notable exceptions). The reason for the wide variation in the reported value of the Avrami exponent is not clear but maybe related to the difference in the film thickness and electrolyte recipe (Most of the work in the literature is based on using proprietary electrolyte chemistry which complicates the comparison between different independent studies).

Although there has been significant research done on the topic, some work is still needed to provide a more in-depth understanding of self-annealing and

annealing in copper thin films. This includes a complete characterization of self-annealing using a standard (not proprietary) electrolyte. Since annealing is a key step in the fabrication of copper interconnects, a model that can describe the recrystallization rate during isothermal and continuous annealing treatments will be useful. All the models that are available in the literature are based on self-annealing profiles. Since the microstructure details appear to affect the performance of copper interconnects, a better understanding of the correlation between the microstructure and resistivity is needed. This also includes an investigation of where self-annealing initiates and what is the best measure to quantify the microstructure evolution. For future high performance integrated circuits, further enhancement of the microstructure is required to address the rapidly rising reliability and performance challenges. This requires an understanding of the role of alloying and a development of novel deposition strategies to optimize the microstructure characteristics.

Chapter 3

Research Objectives

The main objectives of this study are:

1. Quantify the effect of deposition conditions (film thickness, deposition rate, and electrolyte age) on the recrystallization rate of electrodeposited copper thin films using a standard (not proprietary) electrolyte.
2. Examine the correlation between the microstructure and resistivity during self-annealing.
3. Develop a phenomenological model to describe recrystallization rate during isothermal and continuous heat treatments.
4. Examine the microstructure evolution in films produced by: 1) variable deposition rates, and 2) copper-silver co-deposition.
5. Develop a phase-field model to simulate the phenomenon of self-annealing and the role of deposition current density.

Chapter 4

Materials and Experimental Methodology

4.1 Substrate Preparation

The substrates used in this work were 1 mm-thick glass sheets. The procedure for substrate cleaning involved a treatment in a hot bath containing nitric acid and sulfuric acid (1:1 volume ratio) for 5 hours. The substrates were then rinsed with deionized (DI) water in the clean room and dried using nitrogen gas. The final preparation of the substrates involved hot plate treatment at 90 °C for 10 minutes to completely remove any excess water at the surface of the substrate.

In this work, physical vapour deposition (PVD) was used to fabricate a thin chromium (Cr) layer on the top of the glass substrate followed by a thin layer of gold (Au). The purpose of the Cr layer is to improve the adhesion between the glass substrate and the Au layer which was used as a seed layer for the subsequent electrodeposition experiments. In each deposition experiment, three glass slides were prepared and placed in the centre of the PVD chamber. Since good deposition quality is desired, a suitable vacuum is required before starting the deposition. The deposition was per-

formed once a chamber pressure of 1.6×10^{-6} Torr (2.1×10^{-4} Pa) had been reached. The fabrication of Cr and Au layers in the PVD system used here (AIRCO Temescal CV-B) involves heating the target material using two different methods: electron beam heating or thermal heating. The target material then evaporates and transports inside the chamber where it deposits on the substrate. In the case of Cr deposition, the material was placed in a crucible and then heated by bombarding it with an electron beam that was generated from a current filament (cathode) and accelerated towards the crucible (Anode). The deposition rate was controlled by the filament current while the thickness of the deposited layer was observed using a thickness monitor. Once the desired thickness was reached (3-10 nm), a shutter was used to stop the deposition and the filament current was turned off. After 10 minutes, the thermal evaporation of the Au layer was started. The gold material (fine grain 99.99% pure, Technic Canada) was placed in an alumina-coated tungsten basket (model RDM-WBAO-3, R.D. Mathis). The basket was then heated to above the melting temperature of gold using an electric current (thermal evaporation). The evaporated Au material was deposited on top of the Cr-coated substrate. Once the required Au thickness (80 nm) was achieved, a shutter was used again to stop the evaporation of gold on the substrate and the current was immediately switched off. The samples were allowed to cool down inside the chamber for 20 minutes. The glass substrate was then cut to smaller substrates with the desired sizes (1×2.5 cm^2 each) using a diamond saw. Before each Cu deposition experiment, the substrate was cleaned using a hot mixture of nitric acid and sulfuric acid (1:1 volume ratio) for 30 seconds and then completely rinsed by DI water.

4.2 Copper Thin Film Electrodeposition

The electrolyte recipe for Cu electrodeposition experiments is shown in Table 4.1 which is similar to the recipe used by Kelly et al. [38]. The prepared electrolyte was always isolated from exposure to light. Except for two experiments that were designed to examine the effect of bath aging, all the deposition experiments were performed using a fresh electrolyte not aged more than 5 hours.

The deposition was performed employing a potentiostat (EG&G model 173) equipped with a digital coulometer (model 179). The film was deposited using a three-electrode system where the substrate (cathode) acts as working electrode. A platinum mesh was used as a counter electrode while a copper wire was used as a reference. In each deposition experiment, 200 mL of electrolyte was used. The film was grown galvanostatically (i.e. constant deposition current). The films studied in this work were deposited at a current density in the range of 5 to 40 mA/cm^2. During deposition, the solution was stirred using a magnetic bar to ensure an adequate mass transport around the substrate. The reaction charge at the cathode was monitored such that the desired film thickness is achieved. Here, the total reaction charge, q, is related to the deposition current, $i(t)$, by

$$q = \int_0^t i(t).dt \tag{4.1}$$

For the case of films produced using a constant deposition current, the total

Table 4.1: The electrolyte recipe used in Cu electrodeposition experiments.

Substance	Concentration
Cupric Sulfate ($CuSO_4.5H_2O$)	0.24 M
Sulfuric Acid (H_2SO_4)	1.8 M
Polyethylene Glycol (PEG)	300 mg/L
Janus Green B (JGB)	1 mg/L
Bis(3-sulfopropyl) disulfide (SPS)	1 mg/L
Potassium Chloride	105 mg/L

charge can be expressed as $q = i.t$. According to Faraday's law of electrolysis, the film thickness, d, is directly proportional to the total charge in the reaction, i.e.

$$d = \frac{M_w.q}{\bar{n}.D.F.A_d} = \frac{M_w}{\bar{n}.D.F.A_d} i.t \tag{4.2}$$

where D is the density of Cu (8.94 g/cm^3), A_d is the deposition area, and M_w is the molecular weight of Cu (63.5 g/mol). Thus, for the case when the deposition current density (i.e. i/A_d) is 40 mA/cm^2, 68 seconds of deposition time are required to achieve a 1 μm-thick Cu film (assuming 100% deposition efficiency). Immediately after deposition, the film was rinsed completely with DI water and dried with clean pressurized air (Falcon Air Duster). In this work, 0.5-3 μm-thick Cu films were deposited. The film thickness was confirmed by two ways: weighing the sample before and after deposition and using the surface profilometer (Dektak 150). The weight measurements revealed that the film thickness is always within -5% of the desired thickness. The same result was also confirmed by the surface profilometer. The scanning electron microscope (SEM) image in Fig. 4.1 shows the cross section of a 2 μm-thick film where the Au seed layer and the Cu film are marked.

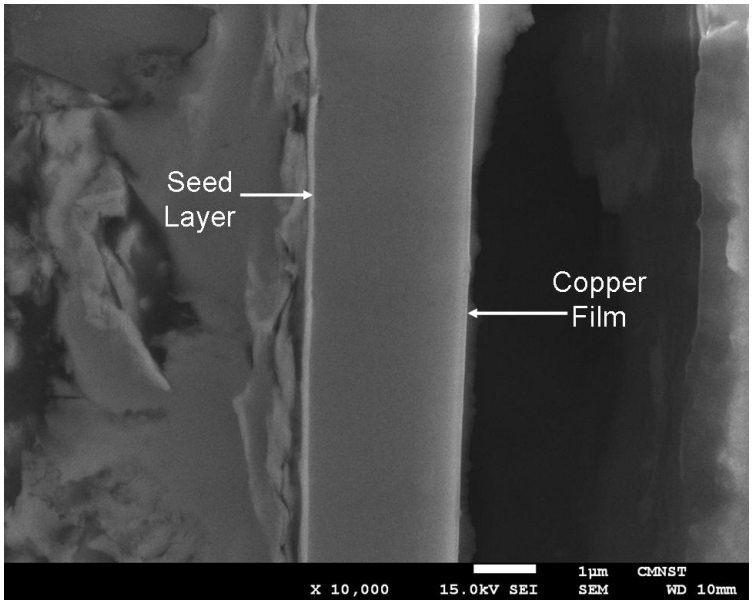

Figure 4.1: A cross section of a 2 μm-thick film deposited at 40 mA/cm^2.

4.3 Resistivity Measurements

Recording of the resistivity evolution of the electrodeposited films commenced approximately 5 minutes after deposition. Here, the resistivity was measured using a four-point probe (JANDEL). The four-point probe is a standard tool that is widely used in the semiconductor industry for wafer and film characterization in which a constant electrical current is injected between the outer pins of the probe. Due to the resistance of the film being measured, a voltage will develop which is sensed by the inner two pins of the probe. For a film with a certain thickness, d, the resistivity is calculated by

$$\rho = K\frac{V}{I}d \tag{4.3}$$

where I, V are the injected current and the measured voltage, respectively

and K is a geometrical correction factor. The value of K depends on the dimensions and shape of the film (i.e. square, circle..), and the geometry of the four-point probe itself (i.e. the spacing between the pins). The four-point probe employed in this study (JANDEL) has a linear arrangement of the 4 tungsten pins with equal spacing between them (1 mm). For this geometry, the K value corresponding to 1 μm-thick film with 1×1 cm^2 dimensions is 4.2209 [127]. The four-point probe measurement was always conducted in the centre of the sample to minimize any effect of the sample edges on resistivity. The voltage signal sensed by the four-point probe was then fed to a lock-in amplifier (DSP SR810 Stanford Research Systems), analyzed and filtered to remove the noise components from the measured signal. The Lock-in amplifier is useful to measure very low voltage signals where the noise signals are attenuated which improves the signal to noise ratio. In this work, the current that was injected in the film for resistivity measurements was a sinusoidal signal with an amplitude of 1.78 mA and a frequency of 1 KHz. A communication link was established between a LabVIEW code on a remote computer and the Lock-in amplifier. The acquired voltage signal was then processed by the LabVIEW code to obtain the time-resistivity profile according to Eq. 4.3. To check the accuracy of the resistivity measurements, a 25 μm-thick platinum foil was used as a reference. The room temperature resistivity was recorded at different locations of the sample and the average of 11 measurements was determined to be 11.02 $\mu\Omega$.cm with a standard deviation of 0.07 $\mu\Omega$.cm. The difference between the average resistivity value and the bulk resistivity of platinum at 20 °C (10.5 $\mu\Omega$.cm [128]) is 5.3% .

4.4 Annealing Treatment

The film resistivity was also measured during annealing treatments. For this purpose, a heating stage was employed. The temperature of the heating stage was controlled by an autotuning temperature controller (Lakeshore 321) in which an electrical current is passed through a predefined resistor. In this setup, the heat treatment parameters are specified by the user (e.g. heating rate and holding temperature) while the actual temperature of the stage is measured by a thermocouple. The temperature controller then uses an internal closed-loop control algorithm (PID controller) to adjust the actual temperature by increasing or decreasing the current that is passing through the heating stage resistor. In this setup, the parameters for the PID controller are auto tuned to achieve a proper response time. During the heat treatment, the four-point probe was used to measure the resistivity as specified in section 4.3. In the present study, the annealing temperature was less than 120 °C which is the maximum temperature allowed for the operation of the four-point probe. A communication link was established between the LabVIEW code on the remote computer, lock-in amplifier and the temperature controller such that a synchronized resistivity-temperature-time measurement was collected.

Two types of heat treatments were performed. First, the samples were heated from room temperature at a specific heating rate (10 °C/min) to the desired annealing temperature (40, 60 °C) and held there for a prescribed annealing time. In the second heat treatment type, the samples were continuously heated from room temperature to 100 °C at different heating rates (0.2-15 °C/min). The samples were then air-cooled to room temperature at a

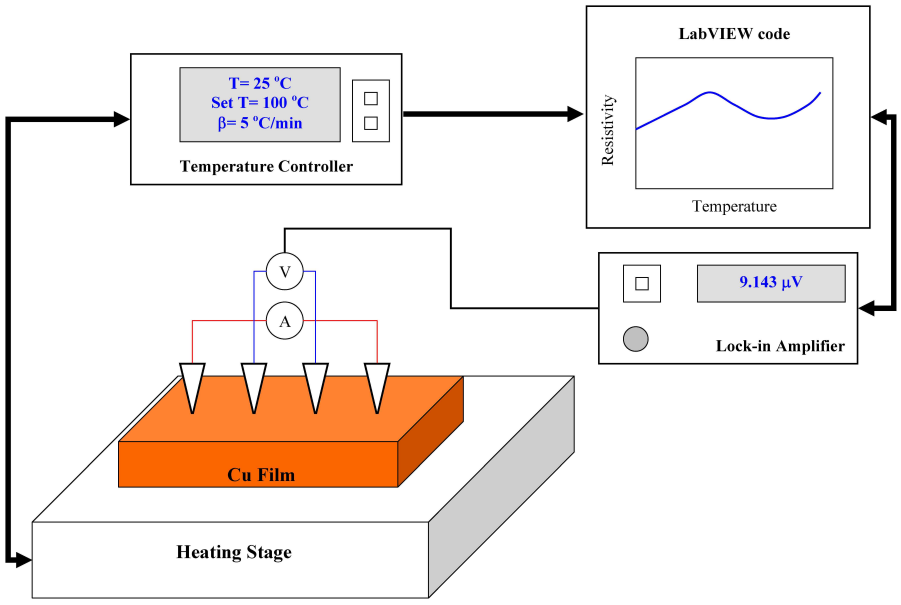

Figure 4.2: A schematic diagram for the setup used for resistivity measurement during annealing treatment.

rate of 2-5 °C/min. A schematic diagram for the setup used in the annealing treatment studies is shown in Fig. 4.2.

4.5 Microstructure Observation by EBSD

The microstructure of the film surface was observed by electron backscatter diffraction (EBSD). The EBSD characterization was carried out in a field emission gun scanning electron microscope (JEOL JSM-7001F) equipped with a TexSEM Laboratories (TSL) EBSD system. A schematic diagram for the principle of EBSD is shown in Fig. 4.3. In this technique, an electron beam interacts with the surface of the film which results in backscattered diffracted electrons that escape from the sample surface. The diffracted

electrons are then intercepted by a phosphorus screen where the diffraction pattern (normally referred to as a Kikuchi pattern) is captured by a CCD camera (EBSD detector). Here, the sample is rotated by 70° to increase the number of backscatter diffracted electrons which enhances the quality of the EBSD pattern. The EBSD pattern is stored and analyzed by a computer where the planes that generate the EBSD pattern are indexed. The indexed EBSD pattern is used to determine the crystallographic orientation of the scanned point. The electron beam is rastered and the EBSD indexing is automated such that a complete orientation map of a predefined size (e.g. 10 μm $\times$ 10 μm) is obtained.

In this work, in-situ EBSD was used to obtain the orientation maps of films that were deposited at rates of 10, 30 and 40 mA/cm^2. In these experiments, the deposition current was controlled by an AUTOLAB potentiostat. The electrolyte temperature during deposition was 25 °C. The sample preparation included surface polishing with 20 nm particle size colloidal silica for 3 minutes. The procedure is a combination of polishing and etching that removes the deformed layer [129]. Conductive liquid silver paint (PELCO® colloidal silver, supplied by Ted Pella Inc.) was used to mount the glass substrate and make a conducting path between the film and the EBSD sample holder. The sample was first tilted at 70°. A 10 μm $\times$ 10 μm area near the center of the film was then scanned. The scan step size was 30 nm. The time between completing the deposition experiment and starting of the EBSD scan was 3, 1.75 and 2 hours for films deposited at 10, 30 and 40 mA/cm^2, respectively. The time required to complete one scan was 40 minutes for the film deposited at 10 mA/cm^2 and 55 minutes for films deposited at 30 and 40

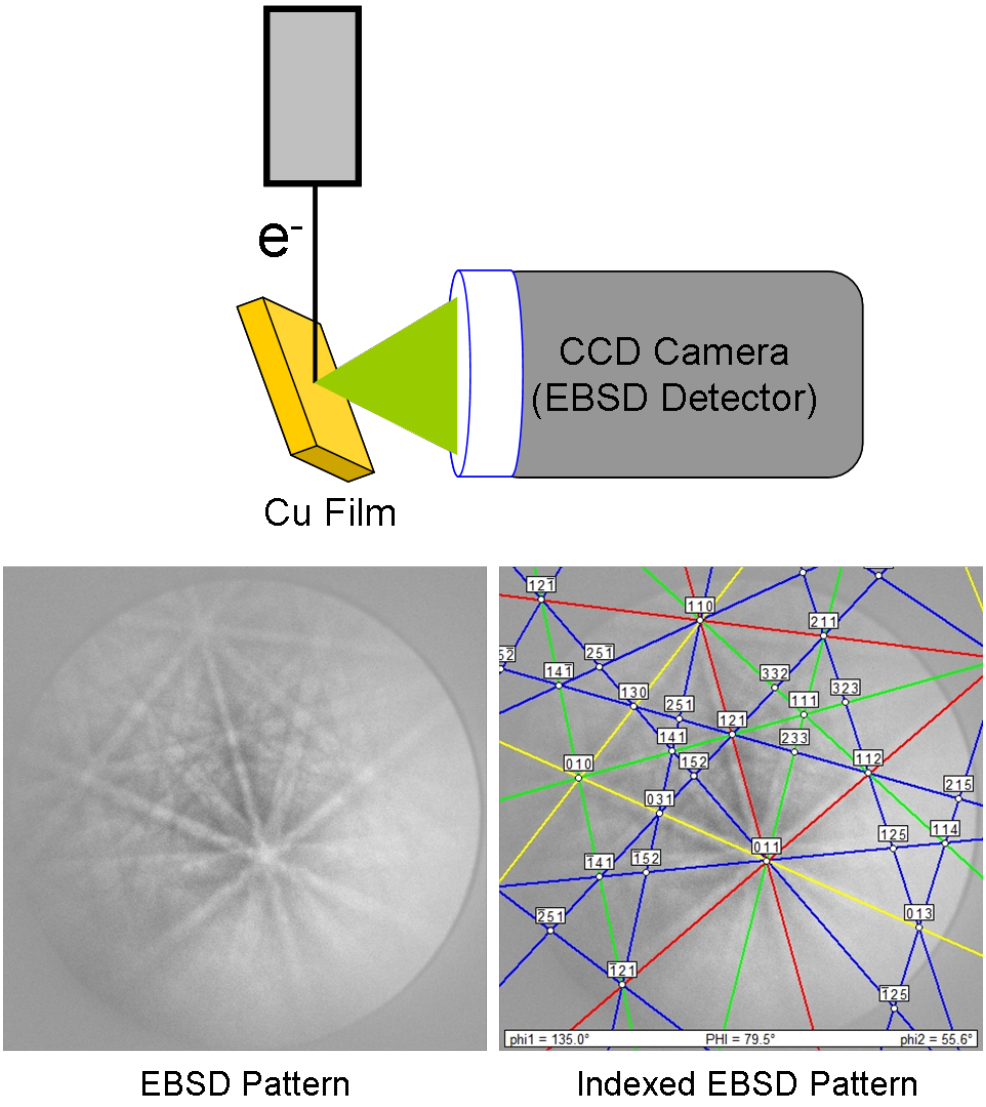

Figure 4.3: A schematic diagram of the EBSD technique. The EBSD pattern of Cu thin film and the indexed planes are also shown.

mA/cm^2. For the sample that was deposited at 40 mA/cm^2, another EBSD scan for a different 10 μm $\times$ 10 μm area was performed 49 hours after deposition with a 100 nm step size. To study the film texture, larger orientation maps (75 μm $\times$ 75 μm scan area) were collected after 8 days following the deposition for films that were deposited at 20, 30 and 40 mA/cm^2. In these maps, 100 nm step size was used. EDAX/TSL OIM$^{\text{TM}}$ software version 5.2 was employed to clean and analyze the EBSD datasets. The cleaning process for each case involves single iteration grain dilation. Here, any group of more than 5 scan points is considered a grain if their misorientation is within 5°. The grain dilation algorithm works only on points that do not belong to a specific grain but still have neighboring points that do belong to grains. In this case, the orientation of a specific point is changed to match that of the majority neighbours [130].

4.6 X-ray Diffraction Measurements

For the 1 μm-thick film deposited at 40 mA/cm^2, X-ray diffraction measurements were carried out using Rigaku Multiflex X-ray diffractometer (Cu-K_α source with 1 degree diffraction and scattering slits and 0.3 mm receiver slit). The operating beam voltage and current were 40 kV and 20 mA, respectively. The area of the film was 1 cm^2 and the standard sample holder was used. The XRD scan started 17 minutes after deposition in a continuous mode (40°-55° 2θ) with a scan speed of 2 degrees/min. The XRD scan was continuously repeated during the first 7 hours following deposition.

Chapter 5

Self-Annealing and Resistivity-Microstructure Correlation

5.1 Introduction

This chapter deals with the phenomenon of self-annealing that occurs at room temperature. In section 5.2, resistivity was used to describe self-annealing in 0.5-3 μm-thick films. The effect of deposition conditions on the process rate is discussed. Section 5.3 covers the in-situ observations of self-annealing by EBSD. The correlation between resistivity and the film microstructure is then discussed in section 5.4. The characteristics of the final microstructure and film texture are presented in section 5.5.

5.2 In-Situ Observation of Self-Annealing Using Resistivity Measurements

Table 5.1 shows the as-deposited resistivity and the expected average grain size of 3 μm-thick films deposited at 40 mA/cm^2 (6 samples). Here, the aver-

Table 5.1: A summary of the as-deposited resistivity and the expected grain size of 3 μm-thick films deposited at 40 mA/cm^2. The experiment was repeated 6 times.

Parameter	Mean	Standard deviation	Coefficient of variation×100
As-deposited resistivity ($\mu\Omega$.cm)	2.35	0.06	2.6
$(\rho_0 - \rho_T)/\rho_T \times 100$	40.8	3.6	8.8
Expected grain size (nm) (ω=0.2)	33.5	2.9	8.7
Expected grain size (nm) (ω=0.5)	133.8	11.6	8.7

Note: Coefficient of variation= Standard deviation/Mean.

age as-deposited resistivity is 2.35±0.06 $\mu\Omega$.cm which is around 41% higher than the bulk resistivity of copper. Since the bulk resistivity of copper is attained when the average grain size exceeds 1 μm, the high resistivity values of the as-deposited films indicate microstructures that consist of nanocrystalline grains. Using the Mayadas-Shatzkes model (Eq. 2.5) and considering the values of the grain boundary scattering coefficient that are available in the literature (i.e. ω=0.2-0.5), the expected average grain size that corresponds to the as-deposited resistivity is less than 150 nm.

The resistivity profiles as a function of time after deposition are shown in Fig. 5.1. Initially, there is a minor decrease in the resistivity of all films during the first one hour after deposition (incubation period). Following the incubation period, a sharp decrease in the resistivity is observed which indicates a significant increase in the average grain size and a decrease in the dislocation density due to recrystallization (i.e. self-annealing). After about 3-4 hours following the deposition, the resistivity starts to saturate when a

Table 5.2: A summary of the final resistivity and the time at 50% recrystallization of 3 μm-thick films deposited at 40 mA/cm^2.

Parameter	Mean	Standard deviation	Coefficient of variation×100
Final resistivity ($\mu\Omega$.cm)	1.82	0.06	3.3
$(\rho_0 - \rho_\infty)/\rho_0 \times 100$	22.62	0.70	3.1
Time at 50% recrystallization (h)	2.17	0.27	12.4

complete self-annealing is attained. Here, the average final resistivity is 1.82 $\pm$0.06 $\mu\Omega$.cm. The total drop in resistivity due to self-annealing is about 21-23%. The resistivity of the film is significantly affected by changes in the average grain size in the range of 0.1-1 μm and further increase in the average grain size has no significant effect on resistivity. In all cases, the incubation period and recrystallization stages can be distinguished based on the rate of resistivity drop.

The fraction recrystallized, f, can be estimated from resistivity using Eq. 2.17. As shown in Fig. 5.2, less than 0.1 fraction recrystallized is observed during the first hour after deposition and complete recrystallization (i.e. f=1) was achieved for all cases in less than 5 hours. As indicated in Table 5.2, the average time required to attain 50% recrystallization is 2.17$\pm$0.27 hours. The reason for the variability in the as-deposited resistivity and the time to attain 50% recrystallization is maybe related to some differences in the film thickness and to some fluctuations of the room temperature. Also, it is possible that there is some variability in the grain boundary reflection coefficient.

A dramatic effect of the film thickness on self-annealing rate was ob-

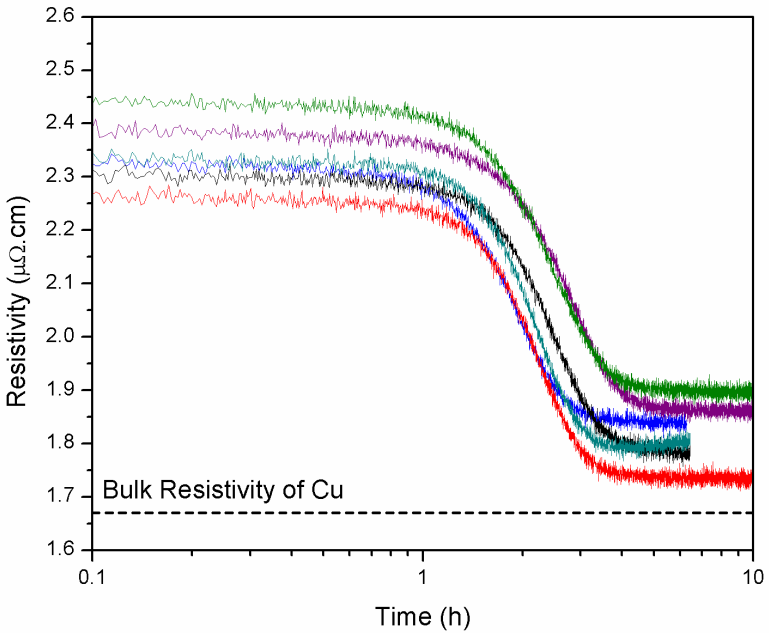

Figure 5.1: The resistivity of 3 μm-thick Cu films as a function of time after deposition for 6 samples. All of the films were deposited at 40 mA/cm^2.

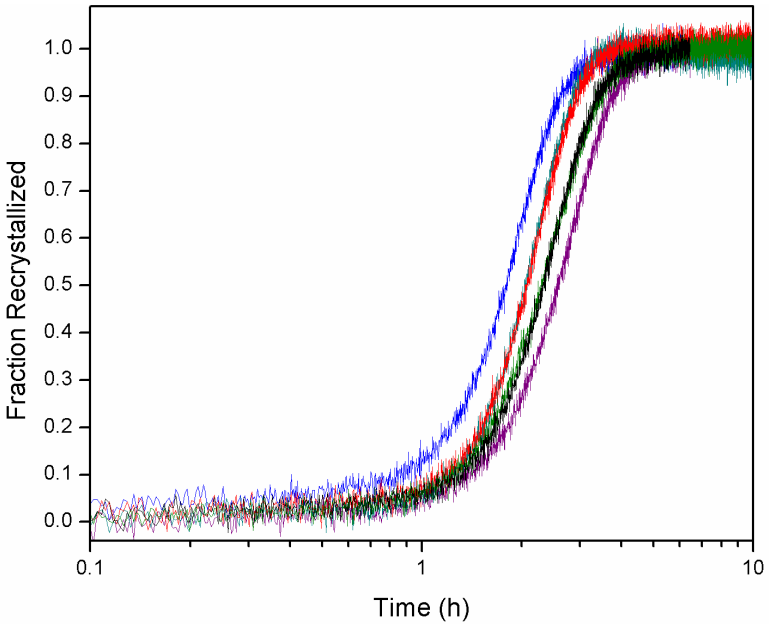

Figure 5.2: The fraction recrystallized of 3 μm-thick Cu films as a function of time after deposition. All films were deposited at 40 mA/cm^2.

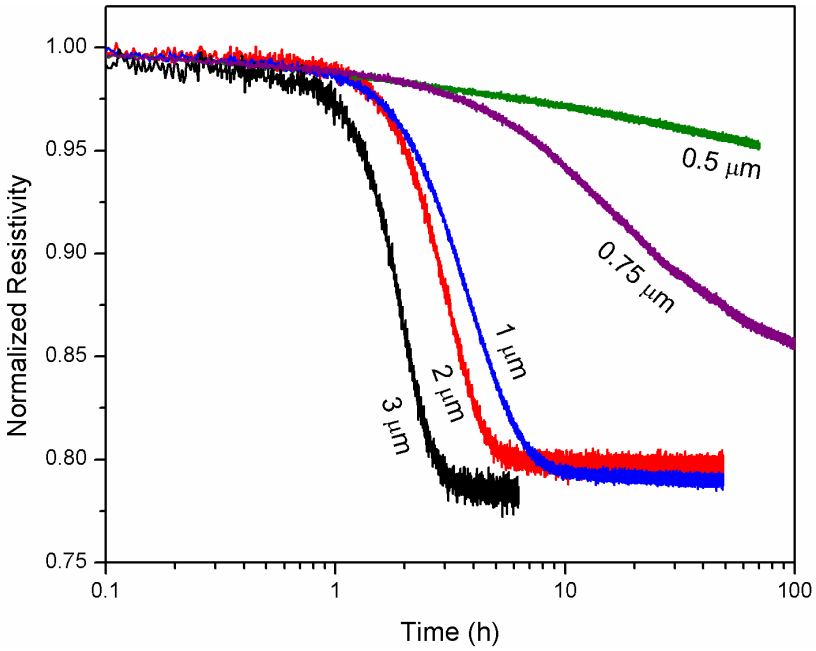

Figure 5.3: Effect of film thickness on the normalized resistivity profile of Cu films deposited at 40 mA/cm^2.

served even though the films were produced at the same deposition current density (i.e. same driving pressure for recrystallization). Here, the rate of self-annealing is accelerated as the film thickness is increased from 0.5 μm to 3 μm as illustrated in Fig. 5.3. The resistivity profile of the 0.5 μm-thick film indicates that the film underwent a very slow self-annealing and less than 5% resistivity drop was measured even after 80 hours following the deposition. The resistivity profile of the 0.75 μm-thick film shows faster self-annealing than the 0.5 μm-thick film but 100 hours were not sufficient to achieve complete self-annealing. As the film thickness is increased further, complete self-annealing is obtained in a relatively short time (i.e. 10 hours or less). While about 10 hours was enough to complete self-annealing for

Table 5.3: A summary of the as-deposited resistivity as a function of the deposition current density. For each deposition current density, the experiment was repeated for at least 5 times.

Parameter	current density (mA/cm^2)			
	10	20	30	40
As-deposited resistivity ($\mu\Omega$.cm)	2.02	2.14	2.31	2.26
Standard deviation	0.06	0.09	0.17	0.09
$(\rho_0 - \rho_T)/\rho_T \times 100$	21	28	38	35

the 1 μm-thick film, about half that time was sufficient for the 2 μm-thick film to reach the same stage. The self-annealing of 3 μm-thick film was completed in 3 hours following the deposition. Here, the effect of thickness on self-annealing rate is more pronounced for films that are 1 μm-thick or less. On the other hand, it can be observed that for the films which are completely recrystallized, (i.e. 1, 2 and 3 μm-thick films), the percentage drop in the resistivity appears to be independent on the film thickness (20-22%). Moreover, and from the initial minor resistivity drop, recovery occurred in all samples.

Table 5.3 shows the room temperature resistivity of as-deposited 1 μm-thick film as a function of the deposition current density. Here, the average film resistivity is about 21-38% higher than the nominal resistivity of bulk copper. It can be noticed that there is an increase in the as-deposited resistivity as the deposition rate is increased. The normalized resistivity profiles of 1 μm-thick films deposited at 5, 10, 20, 30 and 40 mA/cm^2 as a function of time after deposition are shown in Fig. 5.4. Compared with the 40 mA/cm^2 case, an extended incubation period and slower resistivity drop were observed for films deposited at 30, 20 and 10 mA/cm^2. While self-annealing

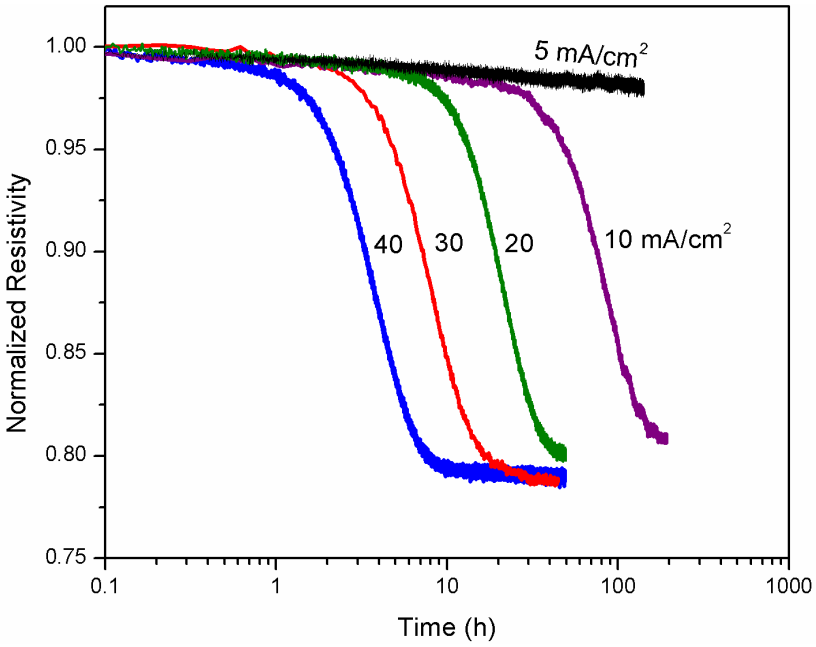

Figure 5.4: Normalized resistivity vs. time after deposition of 1 μm-thick Cu films deposited at different current densities.

is completed within 10 hours in the case of 40 mA/cm^2, approximately two days passed before detecting the onset of self-annealing for the deposition rate of 10 mA/cm^2. It is observed that the total resistivity drop for the films deposited at 40 mA/cm^2 and 30 mA/cm^2 was approximately the same ($\approx$ 22%). On the other hand, a somewhat lower resistivity drop was observed for the case of 10 mA/cm^2 but even 200 hours following the deposition, the final saturation plateau in the resistivity may have not yet been attained. For the lowest deposition current density studied here (i.e. 5 mA/cm^2), less than 3% resistivity drop was observed even after 6 days following the deposition.

The electrolyte age appears to be critical in the phenomenon of self-annealing. Figure 5.5 shows the effect of electrolyte aging on recrystallization

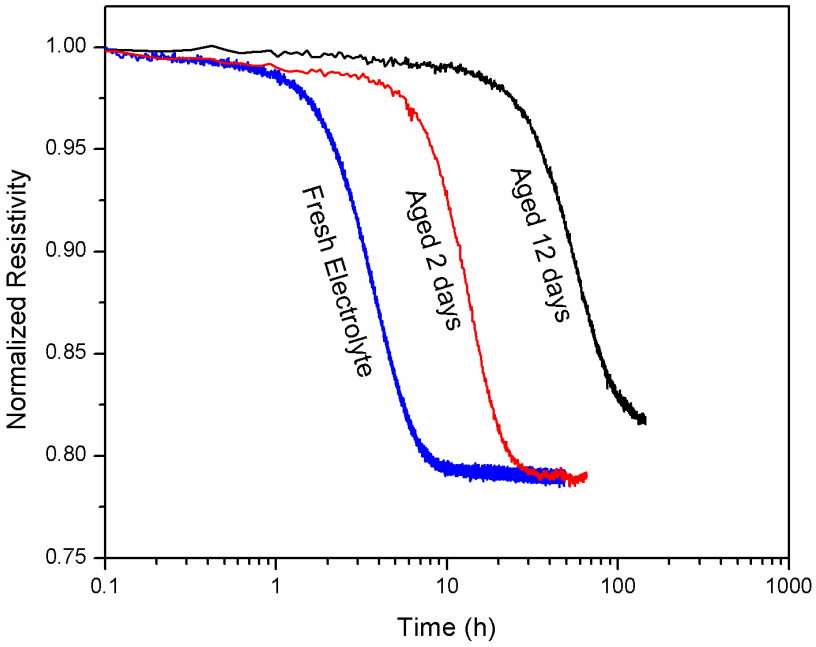

Figure 5.5: Effect of electrolyte age on self-annealing rate of 1 μm-thick films deposited at 40 mA/cm^2.

rate. For fresh electrolyte, the film recrystallized in about 10 hours. On the other hand, the resistivity profile for the film produced using an electrolyte that was aged for 2 days shows a complete recrystallization in 30 hours. For the film which was produced using an electrolyte which was aged for 12 days, the resistivity plateau was not observed even after 100 hours following the deposition (i.e. incomplete recrystallization). In all cases, the incubation period was observed but was extended with aging time. It is believed that the aging effect is a result of the decomposition of additives especially the brightener (i.e. SPS) [131, 132]. Gao [71] reported that an electrolyte aged for 5 hours can be used to minimize the aging effect. In this work, all the samples were produced from an electrolyte not aged more than 5 hours.

5.3 In-Situ EBSD Observation of Self-Annealing

A number of cases were selected for in-situ EBSD observation to represent low, medium and high deposition current density (i.e. 10 , 30 and 40 mA/cm^2, respectively). The EBSD orientation maps of 1 μm-thick film deposited at 10 mA/cm^2 are shown in Fig. 5.6. The as-deposited microstructure consists of nanocrystalline grains as can be seen in the grain size distributions in Fig. 5.7. For the initial microstructure (3 hours after deposition), the peak of the distribution appears to be around 200 nm with an average grain size of about 160 nm. The small grain size in this case is responsible for the high as-deposited resistivity. From the subsequent orientation maps, no significant change in the grain size was observed even after about 8 hours following the deposition. This indicates no self-annealing was occurring. As indicated by the resistivity results shown in Fig. 5.4, a long incubation period before the onset of recrystallization is expected for films produced at low deposition rate (as of 10 mA/cm^2). For this case, further in-situ EBSD scanning was not possible after the 8$^{\text{th}}$ scan because of the increase of carbon contamination at the sample surface.

In contrast, significant changes in the microstructure were observed for the film deposited at 40 mA/cm^2 as can be seen from the in-situ EBSD orientation maps shown in Fig. 5.8. Initially (2 hours after deposition), the majority of the grains in the microstructure are smaller than 400 nm in diameter with an average grain size of about 140 nm as shown in the grain size distribution in Fig. 5.9. However, some grains appear to be larger than the

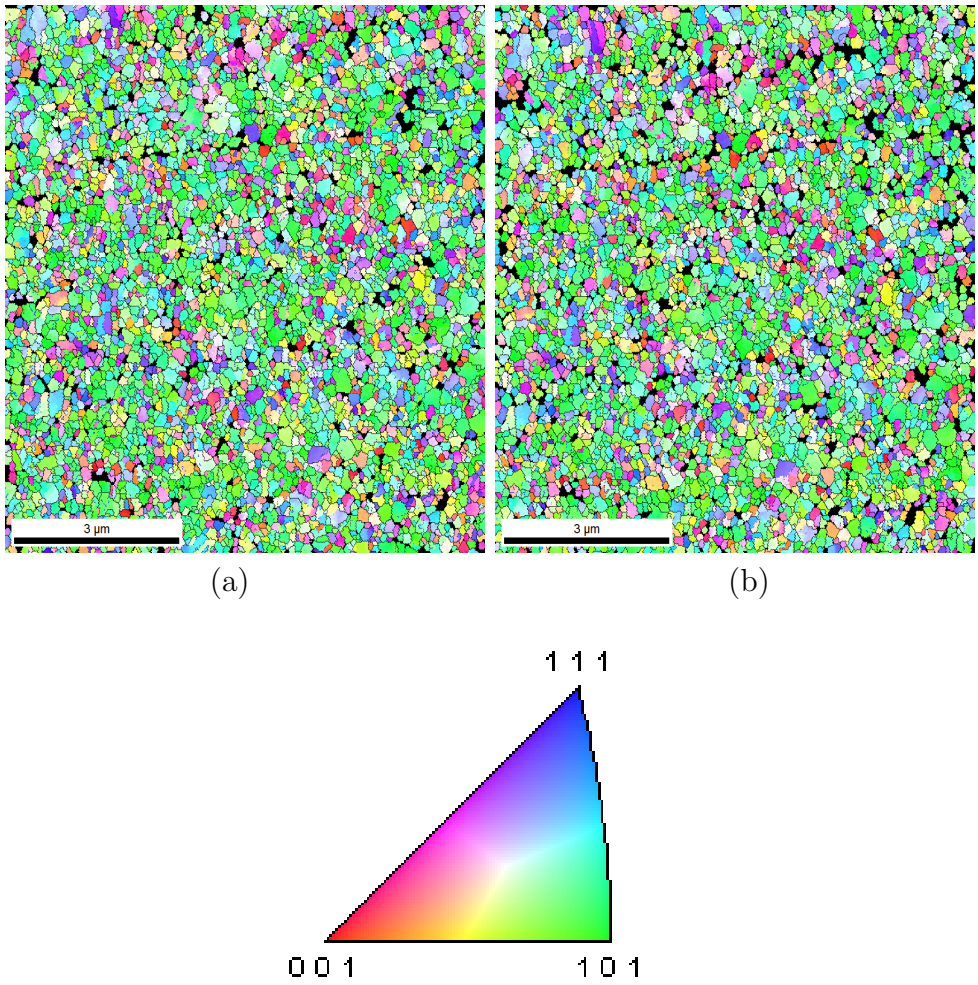

(a) (b)

(c)

Figure 5.6: EBSD orientation maps of 1 μm-thick Cu film deposited at 10 mA/cm^2. The scan started at (a) 3 (b) 5 hours after deposition. The orientation map color code in terms of the out-of-plane inverse pole figure is shown in (c).

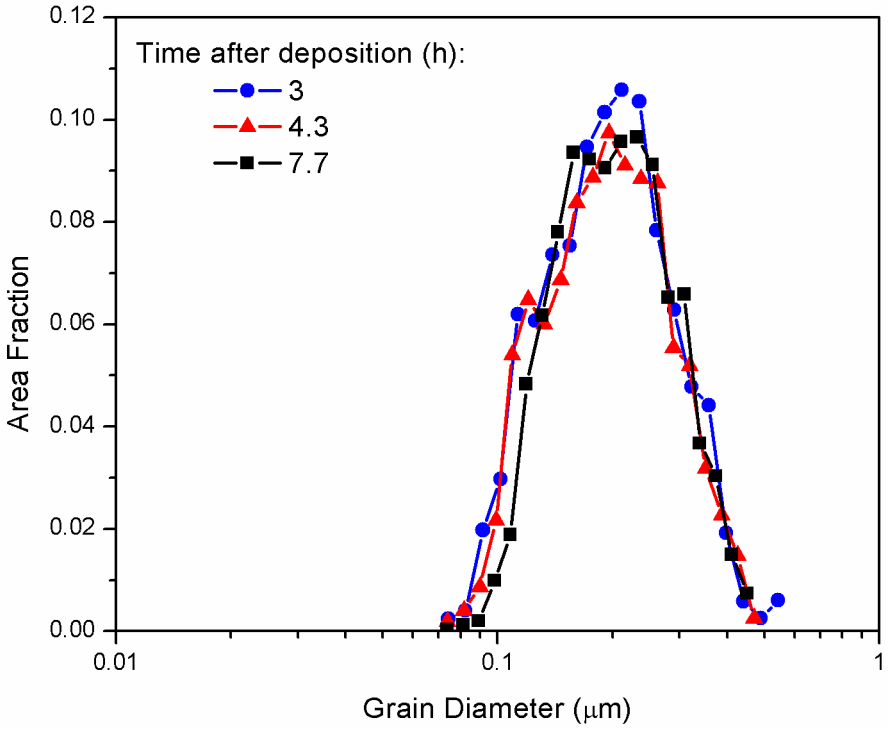

Figure 5.7: Grain size distribution as a function of time after deposition of 1 μm-thick film deposited at 10 mA/cm^2.

average as shown near the lower left corner of the map in Fig. 5.8-(a). These grains seem to be the first indication of recrystallization. In the next map (Fig. 5.8-(b) at about 2.9 hours after deposition), these recrystallized grains grow to consume the nonrecrystallized grains while other recrystallization events occur throughout the scanned area. Self-annealing then continues to proceed towards completion as can be seen from the maps in Fig. 5.8 (c)-(f). The progress of self-annealing can be also observed from the changes in the grain size distribution where grains of diameters greater than 1 μm start to dominate the microstructure at the expense of the small nonrecrystallized grains (see Fig. 5.9). Here, some grains that are larger than 2 μm in diameter

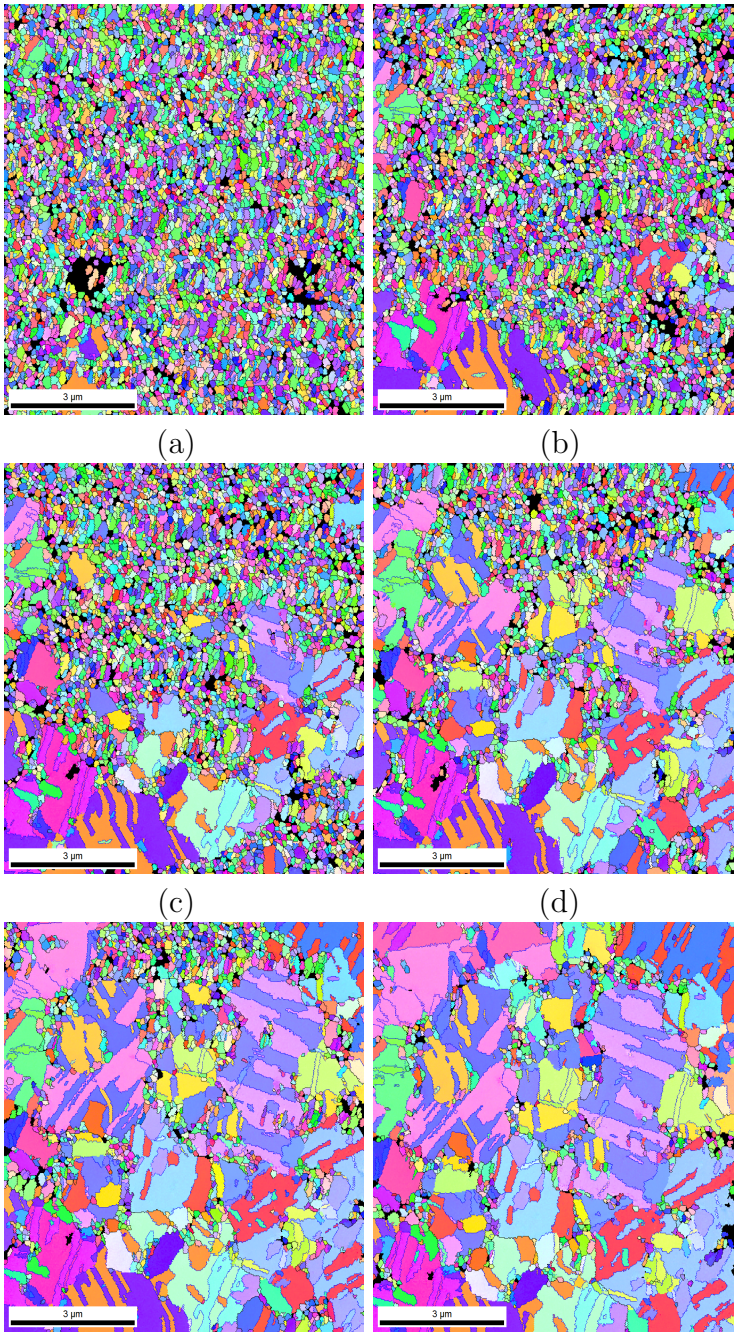

Figure 5.8: EBSD orientation maps of 1 μm-thick Cu film deposited at 40 mA/cm^2. The scan started at (a) 2, (b) 2.9, (c) 3.8 (d) 4.8 (e) 5.7 (f) 7.5 hours after deposition. [133]

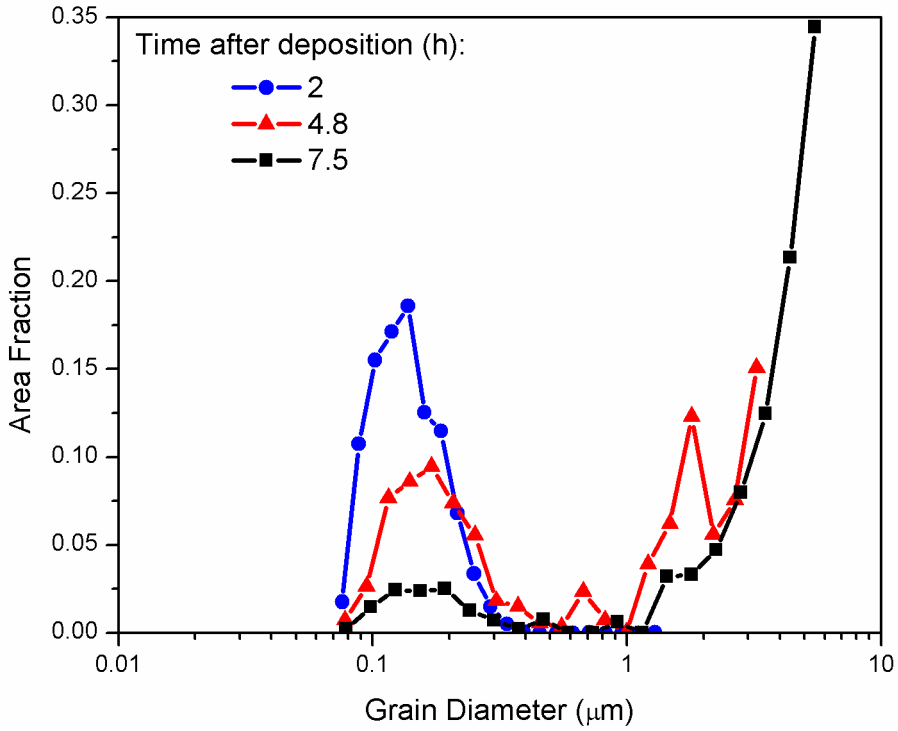

Figure 5.9: Grain size evolution as a function of the time after deposition of 1 μm-thick film shown in Fig. 5.8.

appear after 4.8 hours following the deposition while grains with diameters larger than 4 μm appear after 7.5 hours. Although the majority of the grains were recrystallized after 7.5 hours, some small grains (i.e. nonrecrystallized) are still present between the recrystallized grains.

A closer look at the time evolution of the film microstructure in Fig. 5.8 reveals that as self-annealing proceeds, twinning occurs. Twin boundaries are special boundaries, i.e. $\Sigma 3$ boundaries, that are identified by a rotation angle of 60° around the <111> axis in FCC materials. To extract the twin boundaries from the EBSD map, 5° tolerance from the 60° criterion was used. For example, in the almost fully recrystallized microstructure (7.5 hours after

deposition at 40 mA/cm^2), 52% of all boundaries are twin boundaries compared with only 11% in the as-deposited microstructure (i.e. 2 hours after deposition).

In addition to the orientation map, the recrystallization progress can be tracked by observing the evolution of EBSD image quality (IQ). In the EDAX/TSL OIM^{TM} system, the bands in the EBSD pattern are detected by a Hough Transform procedure where the bands are transformed to intensity peaks. The average height of the intensity peaks represents the image quality [134]. Other image quality metrics were also proposed (e.g. the intensity mean of the EBSD pattern itself [134,135]). The IQ is a measure of the quality of the diffraction pattern. Defects like dislocations produce a distortion effect on the Kikuchi bands which lowers the IQ value [136]. Moreover, the image quality is sensitive to other factors including the presence of other phases and the quality of the sample surface. Figure 5.10 shows the gray scale representation of the IQ maps for the film deposited at 40 mA/cm^2 which corresponds to the same orientation maps shown in Fig. 5.8. The dark areas in the IQ map show scan points with poor image quality which is consistent with what is expected from a nanocrystalline microstructure (poor image quality may also indicate high density of dislocations). On the other hand, the bright regions in the IQ map relate to points with high image quality which may be an indication of the presence of a low dislocation density (i.e. recrystallized points). As self-annealing proceeds, the fraction of points with high IQ values continues to increase. The IQ evolution appears to correlate with the increase in the grain size as concluded from the orientation maps in Fig. 5.8.

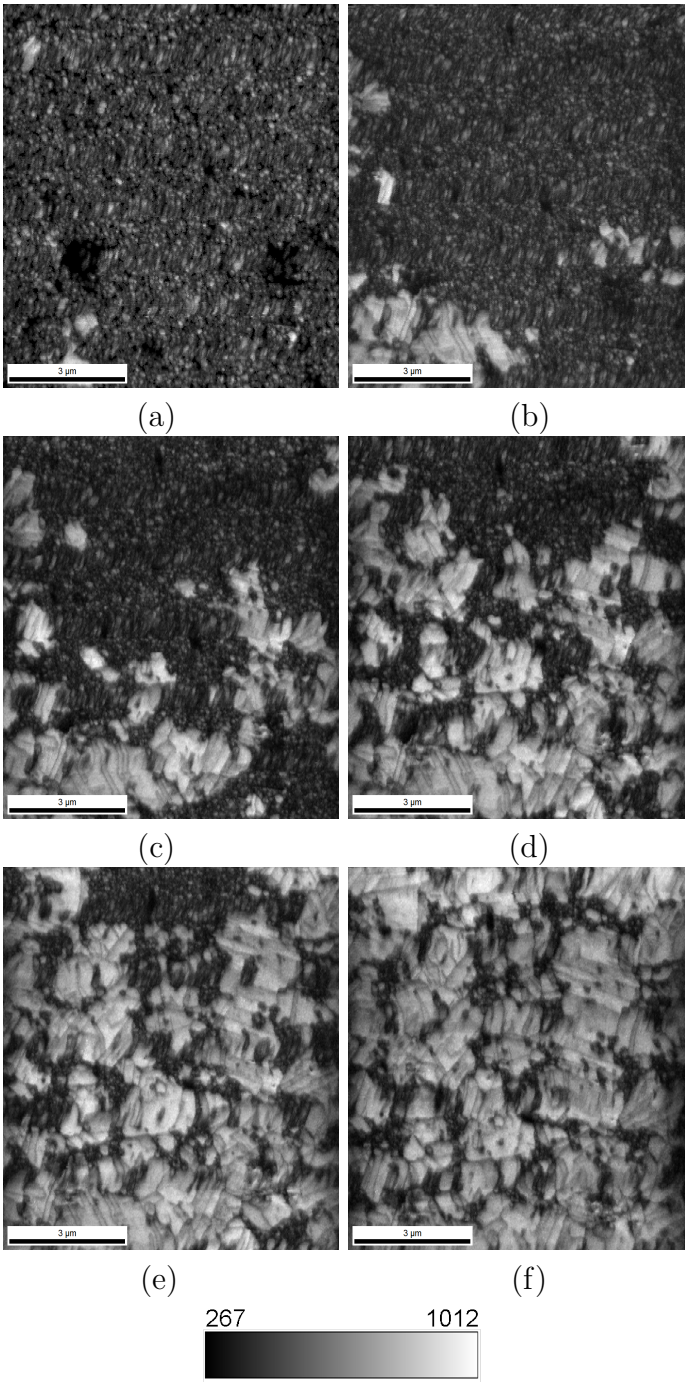

Figure 5.10: The corresponding image quality for the orientation maps shown in Fig. 5.8. [133]

Figure 5.11 shows the image quality across the boundary between a recrystallized grain and nonrecrystallized grains. It can be seen that there is a significant difference between the image quality between recrystallized and nonrecrystallized areas. Moreover, the transition in IQ across the interface is gradual and the thickness of this transition is about 0.15 μm. This indicates that points located near the boundaries have lower image quality values compared with points far away from the boundary (i.e. inside a recrystallized grain). This is due to the overlapping of Kikuchi patterns that originate from two or more adjacent grains with different orientations (IQ is also affected by the surface roughness). The orientation map and the corresponding IQ map after 49 hours following the deposition (shown here in Fig. 5.12) indicate a completely recrystallized microstructure (dark areas in the IQ map correspond to grain and twin boundaries). Here, the grain size is much bigger than the initial grain size (i.e. 2 hours after deposition). The changes in the image quality correlate with the progress of recrystallization as indicated from the sequential orientation maps. In contrast, no significant changes in the image quality was detected for the films that did not show self-annealing as in the case of the film deposited at 10 mA/cm^2 during the first 8 hours following the deposition.

For the intermediate deposition current density of 30 mA/cm^2, self-annealing was observed at the film surface (see Fig. 5.13) . Similar to the film deposited at 40 mA/cm^2, the recrystallized grains appear with diameters exceeding 1 μm (i.e. larger than the film thickness). Also, a similar IQ trend was observed as self-annealing progresses. In this case, even 10 hours after deposition, a fully recrystallized microstructure was not observed. On the other hand,

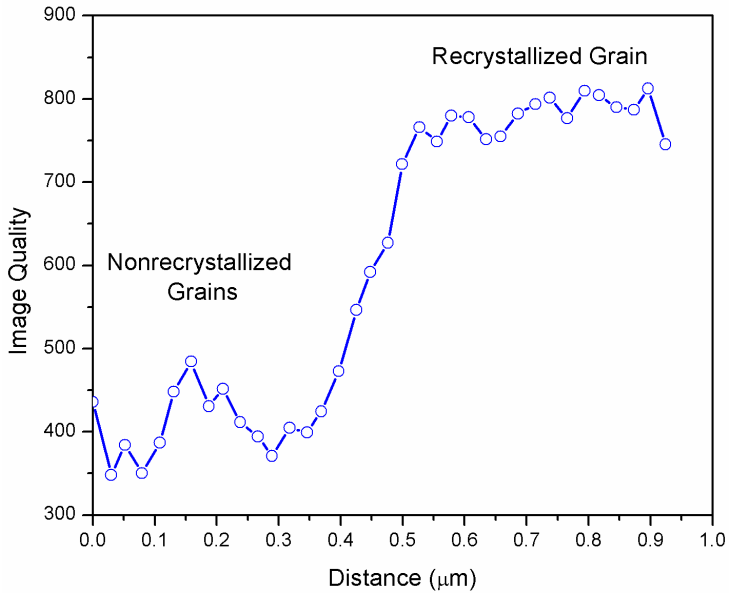

Figure 5.11: An example of the transition in the IQ across the boundary between a recrystallized and nonrecrystallized grains.

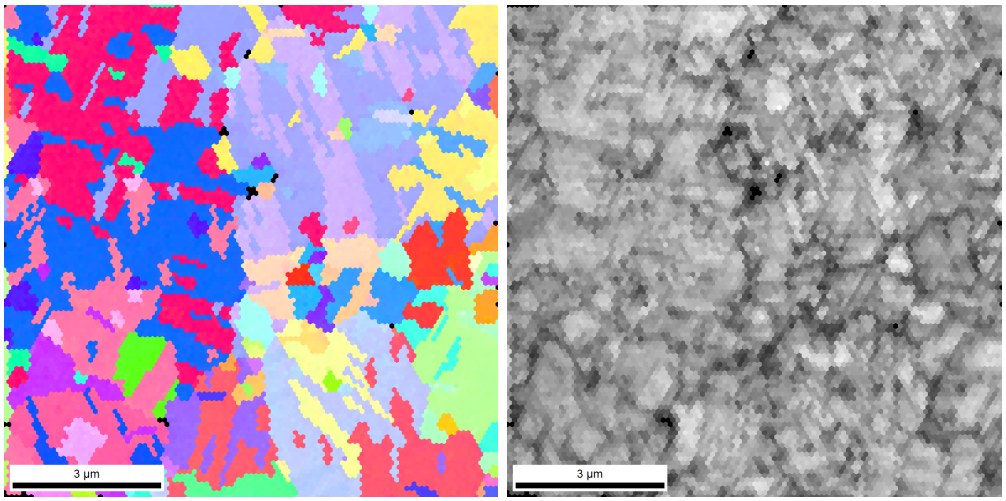

(a) (b)

Figure 5.12: (a) The orientation map and (b) the corresponding image quality map of 1 μm-thick film deposited at 40 mA/cm^2 scanned 49 hours after deposition.

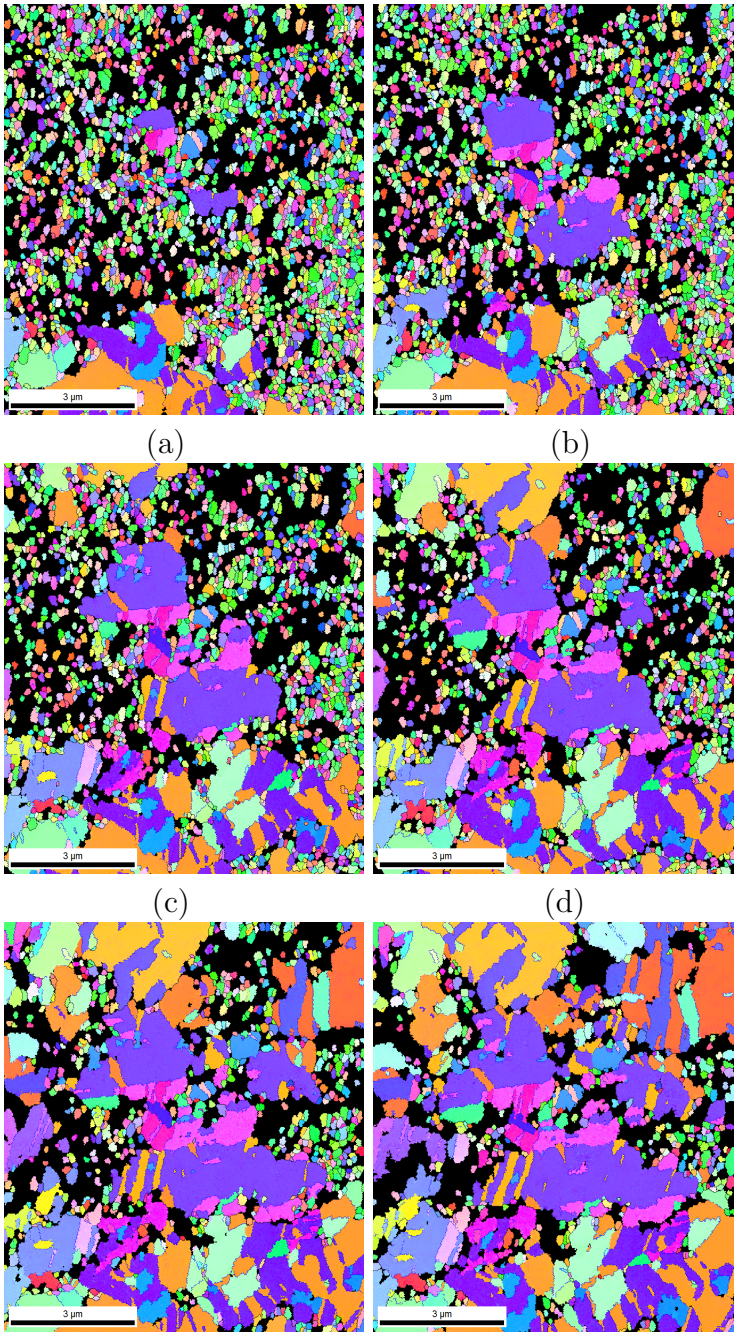

Figure 5.13: EBSD orientation maps of 1 μm-thick Cu film deposited at 30 mA/cm^2. The scan started at (a) 5.4 (b) 6.3 (c) 7.3 (d) 8.2 (e) 9.1 and (f) 10 hours after deposition.

in-situ EBSD seems to be able to capture the stages of self-annealing until about completion for the case when a fast self-annealing rate is expected (e.g. deposition rate of 40 mA/cm^2).

Figure 5.14 shows the orientation map and the corresponding grain size distribution of the film deposited at 5 mA/cm^2. In this case, no indication of recrystallization was observed even after 8 days following the deposition. The majority of the grains are between 0.1 and 0.6 μm in diameter with an average grain size of 174 nm. From the grain size distribution, less than 1% of the scanned area is related to grains with diameters greater than 0.6 μm. Moreover, the microstructure contains a low density of $\sum 3$ twins (11.2%).

For the case of thicker films, a completely recrystallized microstructure was observed for 2 μm-thick film that was deposited at 40 mA/cm^2 even at the first EBSD scan (2.9 hours after deposition). Here, grains with diameter greater than 5 μm dominate the microstructure. No further change in the grain size was detected afterward as shown in Fig. 5.15. On the other hand, the 0.5 μm-thick film that was deposited at 40 mA/cm^2 showed an average grain size of 175 nm after about 2 hours following the deposition. For this case and as shown in Fig. 5.16, no self-annealing during the first 7 hours after deposition was observed. This observation agrees with the very slow resistivity drop that was measured for 0.5 μm-thick film (see Fig. 5.3).

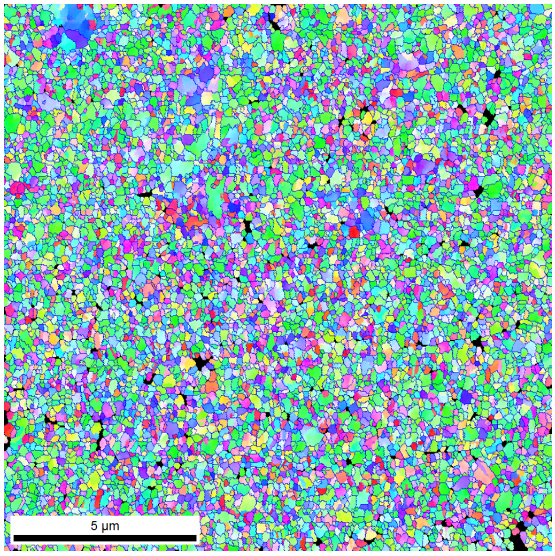

(a)

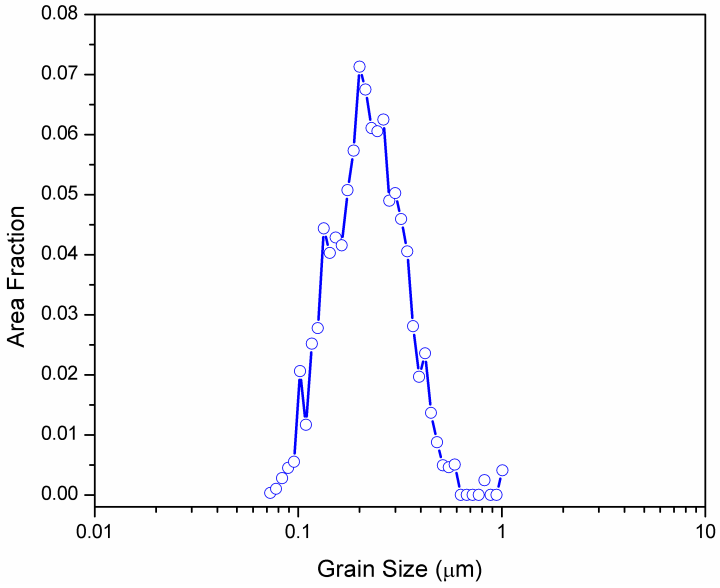

(b)

Figure 5.14: (a) EBSD orientation map (30 nm step size) of 1 μm-thick film deposited at 5 mA/cm^2 and held at room temperature for 8 days (b) the corresponding grain size distribution.

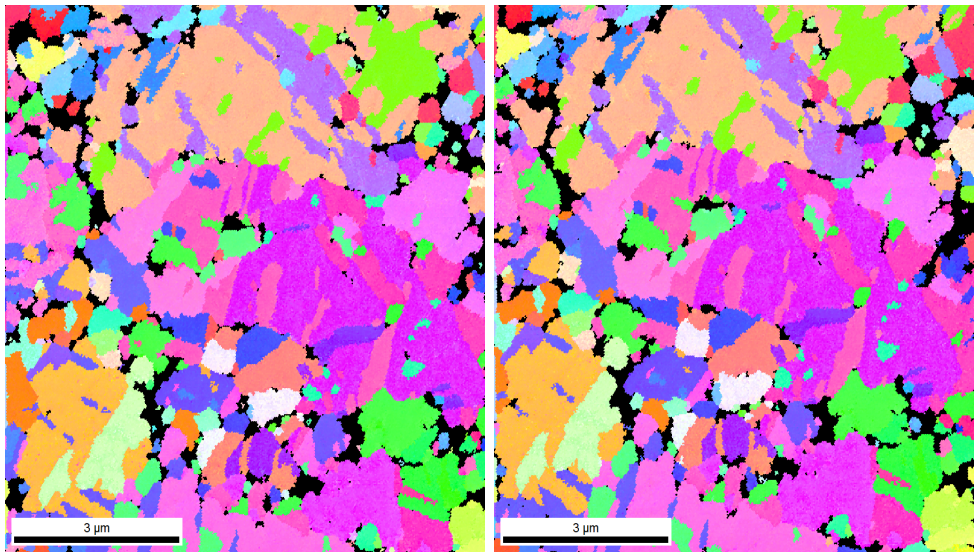

(a) (b)

Figure 5.15: EBSD orientation maps of 2 μm-thick Cu film deposited at 40 mA/cm^2 (a) 2.9 (b) 3.6 hours after deposition.

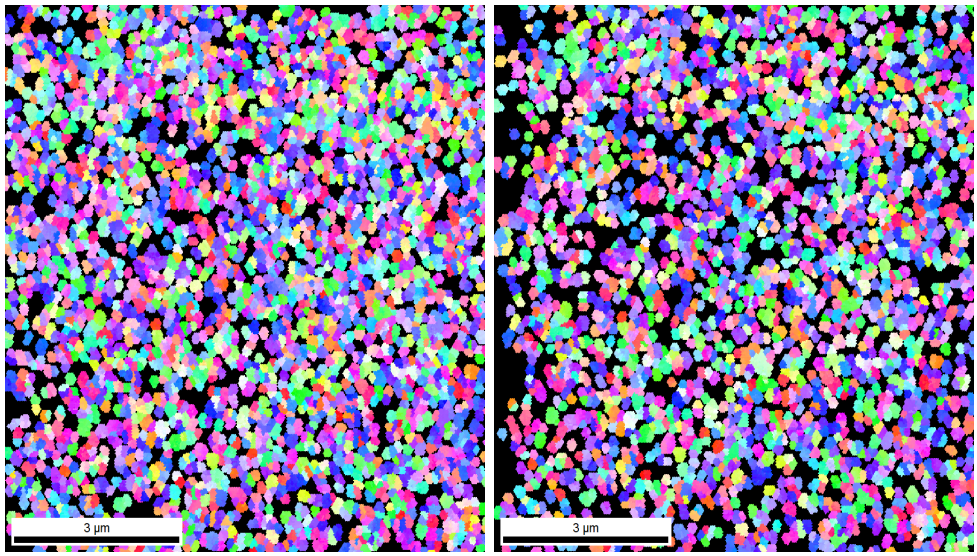

(a) (b)

Figure 5.16: EBSD orientation maps of 0.5 μm-thick Cu film deposited at 40 mA/cm^2 (a) 1.8 (b) 6.4 hours after deposition.

5.4 Resistivity-Microstructure Correlation During Self-Annealing

To obtain the fraction recrystallized from the microstructure, it is first essential to distinguish the recrystallized points from those that did not recrystallize. Actually, there exists no unique criterion to obtain the fraction recrystallized from EBSD data. For example, grain size threshold above which a grain is considered recrystallized can be used for this purpose. When calculating the grain size from EBSD maps, the twins were ignored. By analysing the grain size distribution for the sample grown at 40 mA/cm^2 current density, 400 nm can be chosen as a reasonable threshold. The fraction recrystallized is then simply obtained by adding the area fractions of those grains above the selected threshold. The same threshold value can be adopted for the film deposited at 30 mA/cm^2.

Image quality (IQ) can also be used as a criterion for recrystallization assessment. Tarasiuk et al. [137] developed a technique to distinguish recrystallized areas from the nonrecrystallized based on the difference between IQ values associated with the as-deformed state and that with the recrystallized (or partially recrystallized) state. As pointed out by Humphreys [138], there is always a concern since IQ values are orientation-dependant and an accurate assessment of IQ maps for different samples becomes difficult. As shown in the IQ maps in Fig. 5.10, the recrystallized areas can be visually distinguished from the nonrecrystallized. The IQ distribution as a function of time after deposition for the film deposited at 40 mA/cm^2 is shown in Fig. 5.17. Initially, the IQ distribution appears to be Gaussian with the

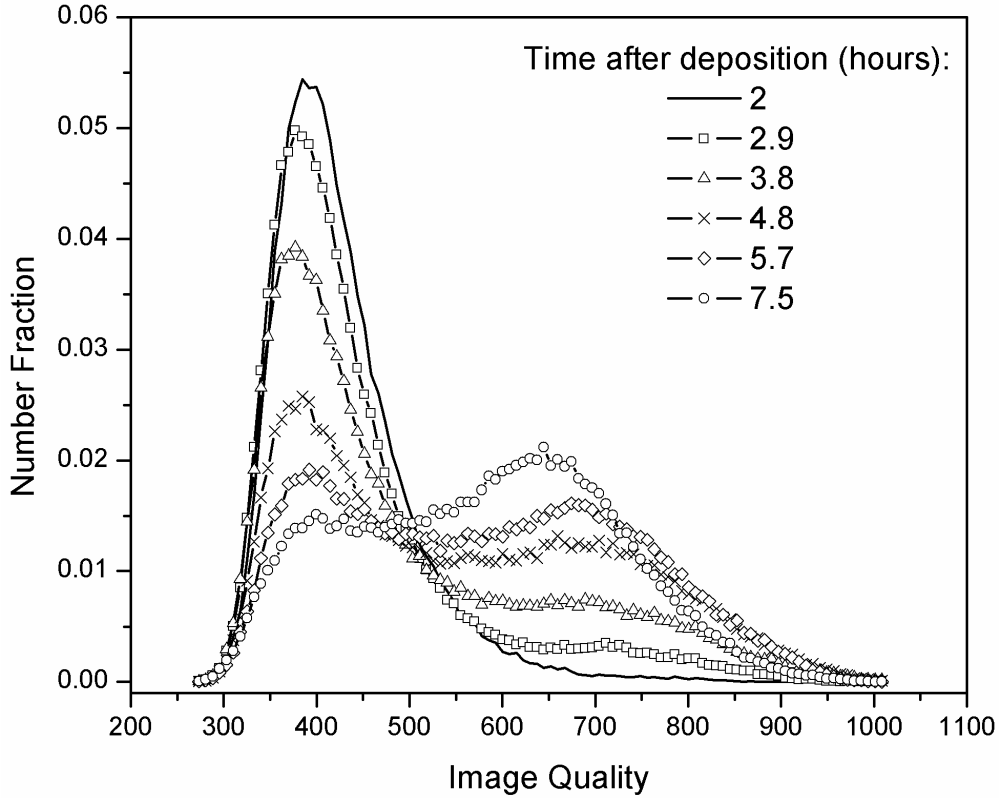

Figure 5.17: The image quality distribution of 1 μm-thick film deposited at 40 mA/cm^2 as a function of time after deposition. [133]

peak of the distribution curve at an IQ value of around 400. The majority of points in the initial scan have IQ values lower than 500. As recrystallization proceeds, the number fraction of points with IQ higher than 500 increases at the expense of the points that have lower IQ values (i.e. nonrecrystallized points or those that relate to the grain and twin boundaries). At 7.5 hours after deposition, the IQ distribution consists of two distinct peaks: one for nonrecrystallized points and the other peak relates to those which are recrystallized. Humphreys [138] suggested that a scan point can be classified

as recrystallized if its IQ value is 50% greater than the mean. For the cases studied here, the IQ distribution profile during recrystallization can be fit using a double peak Gaussian function, i.e.

$$f(x) = a_1 \times \exp\left(-\left(\frac{x-b_1}{c_1}\right)^2\right) + a_2 \times \exp\left(-\left(\frac{x-b_2}{c_2}\right)^2\right) \qquad (5.1)$$

Here, a_1, b_1 and c_1 are the fit parameters for the first peak (nonrecrystallized peak in the IQ profile) while a_2, b_2 and c_2 are the fit parameters for the second peak (recrystallized peak in the IQ profile). An example of applying this procedure is shown in Fig. 5.18. Here, the double peak Gaussian function can describe the data reasonably well. In this work and similar to the grain size cut-off approach, an IQ value at the intersection of the two peaks can be assigned as a threshold to distinguish the recrystallized points in the distribution. From Table 5.4, the IQ at the intersection of the two distributions is between 459 and 531. Here, the average of these values can be taken as a threshold to distinguish the recrystallized points in the microstructure (i.e. $IQ_{threshold}$ =488).

Another method for obtaining the fraction recrystallized is to combine the grain size and image quality (i.e. grain average image quality GAIQ). For a specific grain, the GAIQ is calculated by adding the image quality for all the data points within that grain and then divide by the total number of points [130]. Figure 5.19 shows the relationship between the GAIQ and grain size (GS) for the film deposited at 40 mA/cm^2 at the initial and the final stages of self-annealing. For 2 hours after deposition, the majority of grains

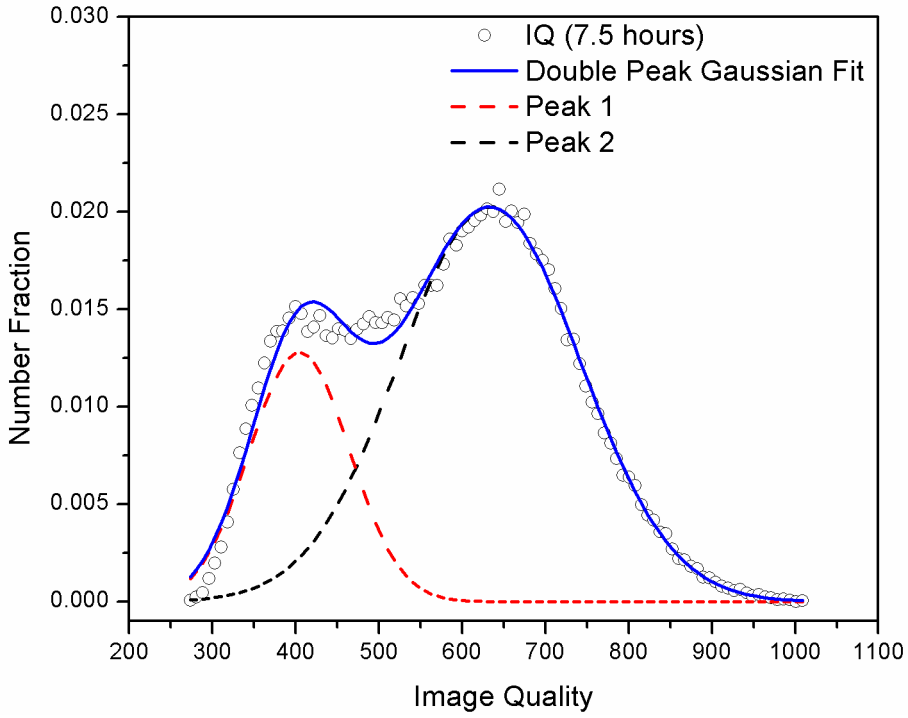

Figure 5.18: An example of fitting the IQ distribution profile using a double peak Gaussian Fit (nonlinear least square method was used to fit the data). [133]

Table 5.4: A summary of double peak Gaussian fit parameters for the IQ profiles shown in Fig. 5.17.

Fit parameter/result	Time after deposition (h)					
	2.9	3.8	4.8	5.7	6.6	7.5
a_1	0.0478	0.0351	0.0219	0.0173	0.0146	0.0128
b_1	397	387	389	409	413	405
c_1	73.5	63.4	65.4	88.4	92.6	85.2
a_2	0.00353	0.00888	0.0130	0.0162	0.0185	0.0203
b_2	721	587	637	668	657	633
c_2	226	233	222	166	154	155
R^2 (Goodness of the fit)	0.96	0.97	0.96	0.96	0.98	0.99
IQ at intersection of the two distributions	531	468	459	500	498	472

are below 0.4 μm in diameter and appear to have low GAIQ values (i.e. 300 $<$ GAIQ $<$ 550). This low GAIQ range corresponds to the nonrecrystallized grains. Only one grain appears to have a diameter larger than 1 μm with a GAIQ value higher than 550 (i.e. onset of recrystallization). In contrast, several grains are visible in the same range (i.e. grain size $>$ 1μm and GAIQ $>$ 550) at 7.5 hours after deposition.

From the EBSD orientation maps, statistical analysis of the orientation gradient such as local orientation spread (LOS) can be useful to assess the progress of recrystallization (see the example shown in Fig. 2.13). In calculating LOS values for copper thin film discussed here, a 3rd neighbour kernel was considered. Here, the misorientation between each point in the kernel and all other points is calculated. The average misorientation value is then assigned as a LOS value [130]. In this calculation, points with misorientation greater than 5° in the kernel were ignored (i.e. points with misorientation

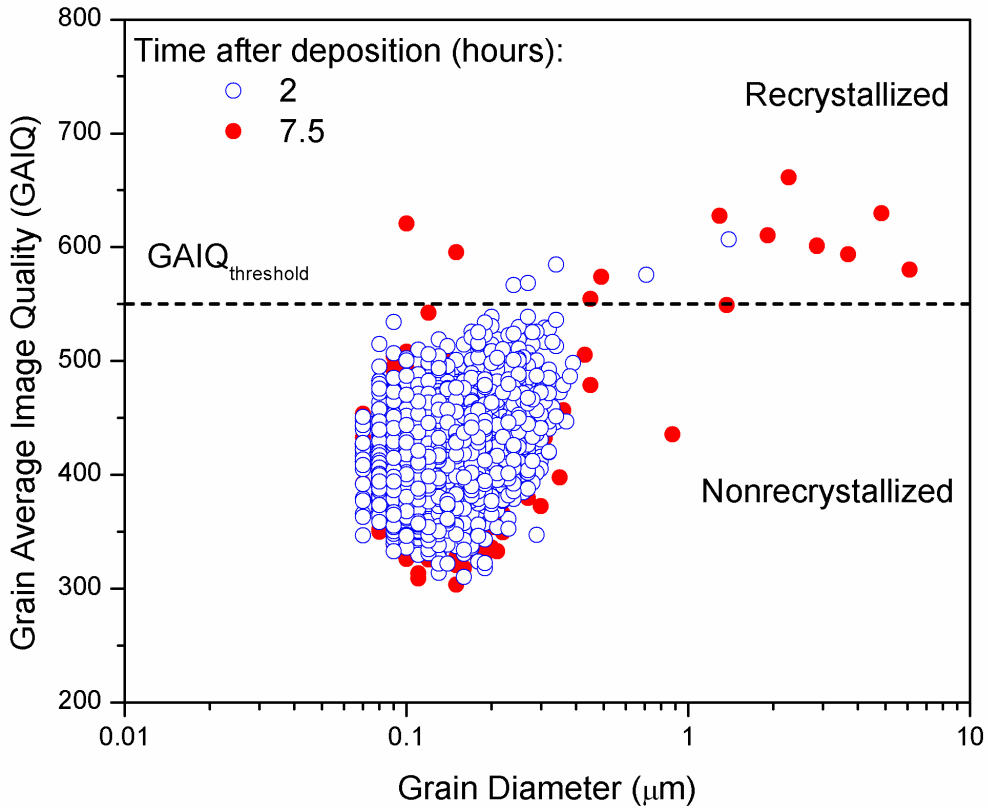

Figure 5.19: The image quality distribution of 1 μm-thick film deposited at 40 mA/cm^2 as a function of time after deposition.

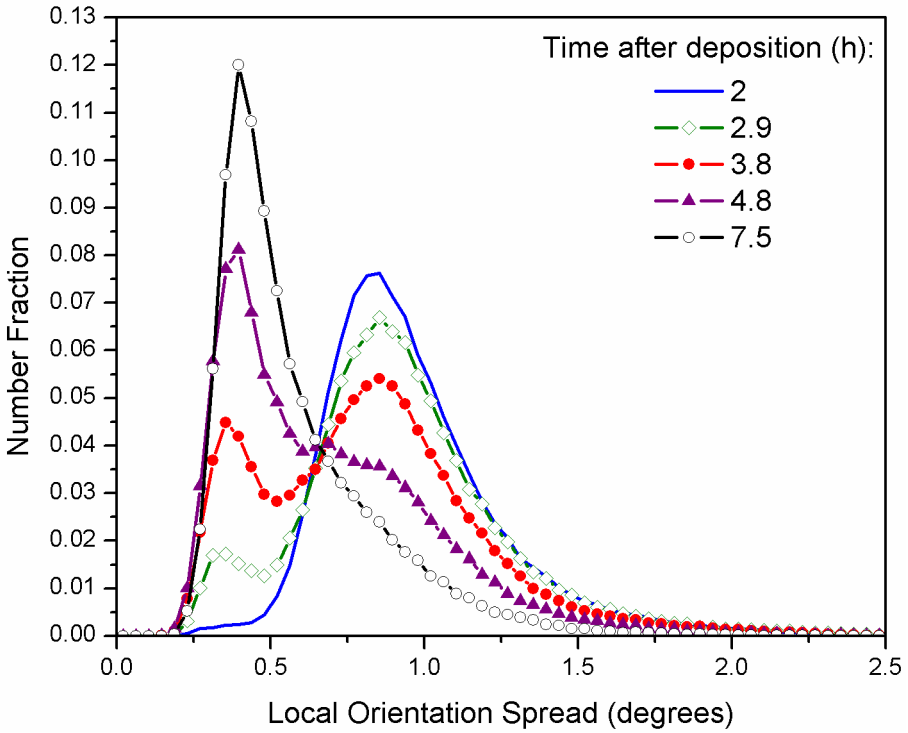

Figure 5.20: The local orientation spread (LOS) distribution of 1 μm-thick film deposited at 40 mA/cm^2 as a function of time after deposition.

greater than 5° belong to a different orientation that can be another grain or a twin within the recrystallized grain). For the case of 1 μm-thick film deposited at 40 mA/cm^2, the initial microstructure (i.e. 2 hours after deposition) has a LOS Gaussian distribution with the majority of points were found to have a LOS value of greater than 0.7° (see Fig. 5.20). As recrystallization proceeds, a distinct peak is observed for points with LOS values less than 0.7°. The intensity of this peak increases with the progress of self-annealing at the expense of points with higher LOS values. The local orientation spread gives a relative indication but not the absolute dislocation density in the grain. Also, LOS calculation may be affected by the fact that the EBSD step size

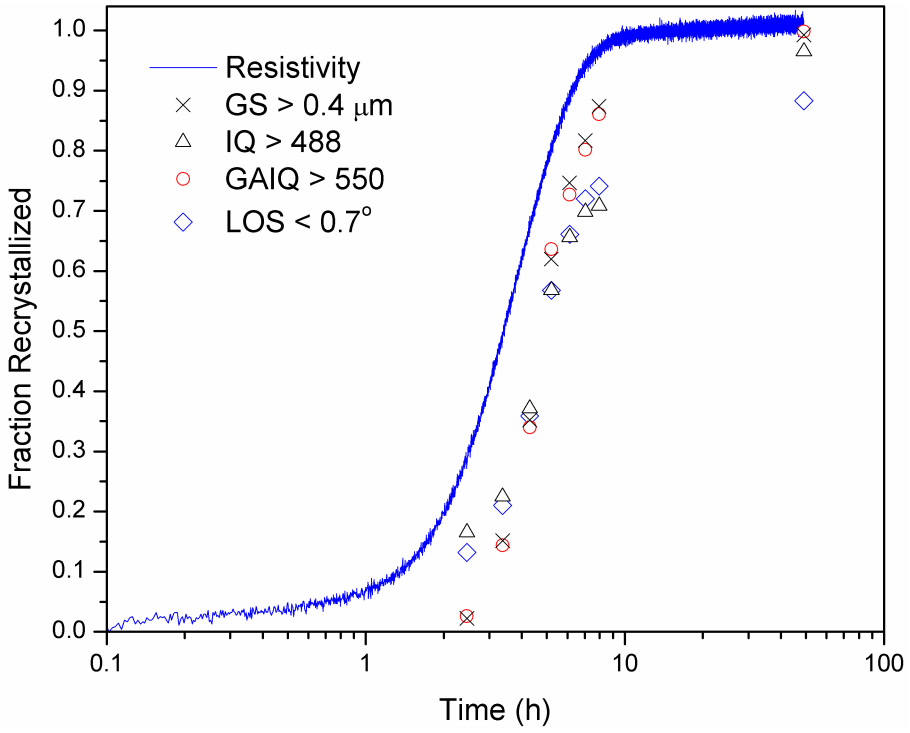

Figure 5.21: Comparison between the fractions recrystallized for 1 μm-thick film deposited at 40 mA/cm^2 obtained from resistivity and that obtained from EBSD using the following methods: grain size (GS), image quality (IQ), grain average image quality (GAIQ) and local orientation spread (LOS). [133]

used here (30 nm) is comparable to the initial grain size. In the case studied here, a LOS value of 0.7° can be considered as a threshold to distinguish recrystallized points from those that did not recrystallize.

Figure 5.21 shows the comparison of the fraction recrystallized profiles obtained from resistivity and EBSD using the four methods described above: GS, IQ, GAIQ and LOS for the film deposited at 40 mA/cm^2. From resistivity, the fraction recrystallized increases with time and self-annealing is completed in 10 hours after deposition ($f \approx 1$ at $t = 10$ hours). From EBSD,

all criteria used to asses the fraction recrystallized show an increase in f with time after deposition. At 49 hours after deposition, GS, IQ and GAIQ show almost complete recrystallization (f>0.95) while LOS shows somewhat less complete recrystallization ($f \approx 0.88$). Overall, all four EBSD criteria describe the trend of the resistivity curve reasonably well. The GS and GAIQ criteria replicate recrystallization more accurately than the IQ and LOS criteria due to the lower image quality near grain boundaries independent of the state of recrystallization. Thus the grain size related criteria, GS and GAIQ, are proposed as a more reliable method to determine the fraction recrystallized from the EBSD maps. Moreover, it appears that there is a time lag between the EBSD fraction recrystallized profile as compared to that obtained from resistivity. This suggests that recrystallization may initiate in the bulk of the film or near the substrate-film boundary. The recrystallized grains then grow and proceed to the film surface where the growth of these grains continues in the lateral direction. The agreement between the fraction recrystallized from resistivity and microstructure appears to improve as recrystallization proceeds to completion. Further, resistivity measurements record the recovery stage that cannot be inferred from the EBSD maps.

In Fig. 5.22, the fraction recrystallized profiles are compared for the samples grown at 30 and 40 mA/cm^2. The grain size criterion was used here (i.e. GS $>$ 0.4 μm). Similar to the 40 mA/cm^2 case, a reasonable correlation was observed between resistivity and grain size for the film grown at 30 mA/cm^2. Initially, there is some discrepancy between the two fraction recrystallized curves but for higher fractions (i.e. f>0.5), the agreement between the two profiles is significantly improved.

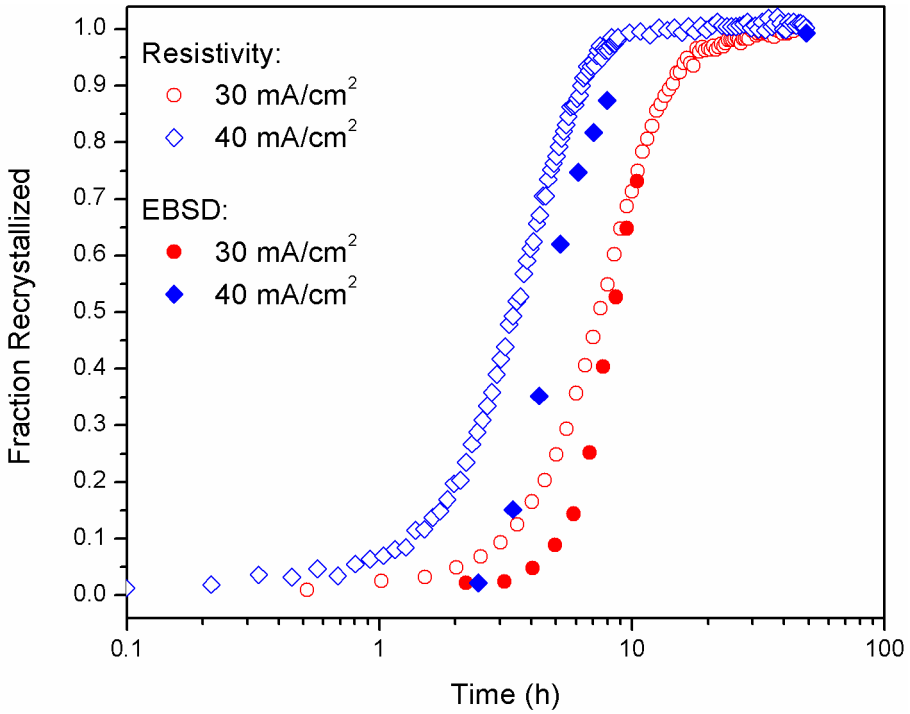

Figure 5.22: Comparison between the fraction recrystallized obtained from resistivity and that obtained from EBSD for 1 μm-thick films deposited at 30 and 40 mA/cm^2. The grain size ($>$ 0.4 μm) was used to obtain the fraction recrystallized from the EBSD maps. [133]

5.5 Final Microstructure and Texture

The EBSD orientation map of the film surface and the corresponding grain size distribution for the completely self-annealed 1 μm-thick films that were deposited at 20, 30 and 40 mA/cm^2 are shown in Figs. 5.23-5.25. All films were scanned at 100 nm step size instead of 30 nm since a big grain size is expected for a completely recrystallized microstructure (8 days after deposition). Here, larger orientations maps are helpful to get better statistics of grain size distribution and texture. In all three cases, the majority of grains

are much larger than the film thickness. While grains with diameters as large as 12 μm can be observed in the case of films deposited at 20 and 30 mA/cm^2, grains with diameters as large as 17 μm are observed for the film deposited at 40 mA/cm^2.

The misorientation profiles for the three films are shown in in Fig. 5.26. In all the three profiles, the strong peak that appears around 60° indicates the presence of high density of $\sum 3$ twins. Here, the corresponding $\sum 3$ twin density for the films deposited at 20 and 40 mA/cm^2 is 56% and 50%, respectively. On the other hand, the film deposited at 30 mA/cm^2 showed less $\sum 3$ twins fraction (33%). For the case of deformed copper subjected to annealing at 400 °C for 1 hour, Field et al. [139] found that the twin density is 29-38%. It appears that the twin density for the case of self-annealed copper film can be significantly higher than the twin density in conventionally recrystallized copper. In addition to $\sum 3$ twins, $\sum 9$ boundaries can be observed ($\sum 9$ boundaries are secondary recrystallization twins and, in FCC materials like copper, are characterized by 38.9° rotation around the <110> axis). However, the density of these twins is less than 5% in all three cases (i.e. the majority of twins that are present in the microstructure are $\sum 3$ twins). The fact that the electrodeposited copper thin film contains a high density of $\sum 3$ twins was attributed to sulfur that is present in grain boundaries which lowers the stacking fault energy for copper [140].

The inverse pole figure of the out-of-plane direction shows a (101) texture for the film which was deposited at 20 mA/cm^2 with a strong (111) texture also being present (see Fig. 5.27). On the other hand, (111) texture is observed for the films deposited at 30 and 40 mA/cm^2 current density.

However, the film deposited at 40 mA/cm^2 showed a stronger (111) texture compared with the film deposited at 30 mA/cm^2 (see Fig. 5.27-c). The (001) texture is present in the films deposited at 20 and 40 mA/cm^2 but not in the film deposited at 30 mA/cm^2.

In addition to resistivity and EBSD, the phenomenon of self-annealing is associated with changes in the X-ray diffraction (XRD) pattern. Here, in-situ XRD diffraction was performed for 1 μm-thick film deposited at 40 mA/cm^2. The XRD scans are shown in Fig. 5.28. Initially, there is a strong (111) peak with weak (200) peak is also present. As self-annealing progresses, the intensity of the (111) and (200) peaks increases with time after deposition. However, the (111) peak remains stronger than the (200) peak. The strong (111) peak and the presence of the (200) peak in the XRD pattern is in agreement with the EBSD inverse pole figure presented in Fig. 5.27-c.

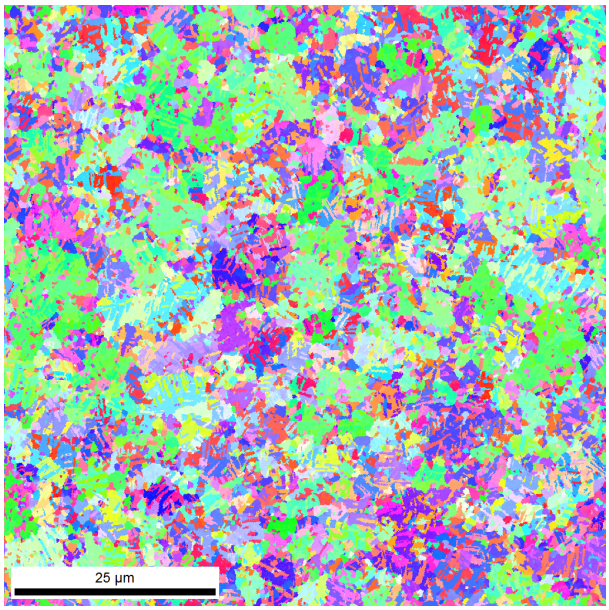

(a)

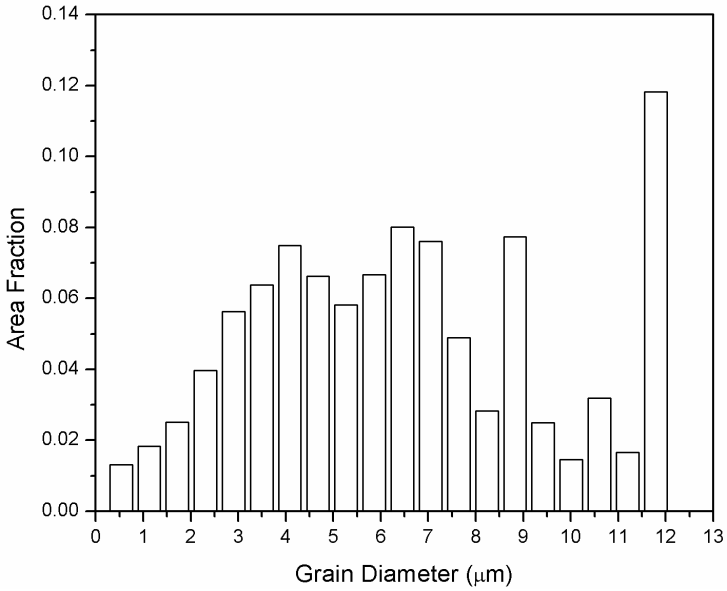

(b)

Figure 5.23: (a) EBSD map of a completely self-annealed 1 μm-thick Cu film deposited at 20 mA/cm^2 (b) the corresponding grain size distribution. The EBSD scan was performed 8 days after deposition.

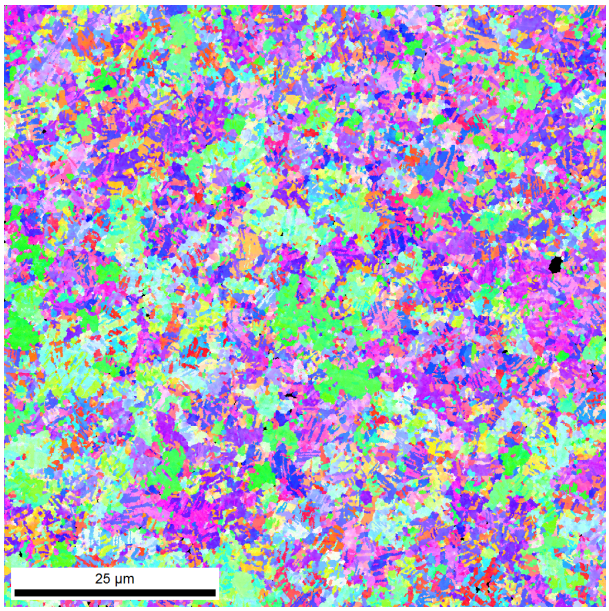

(a)

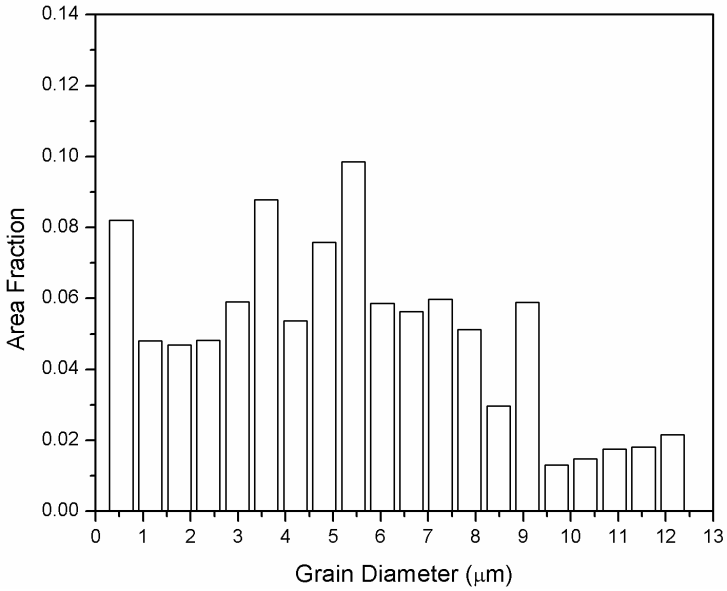

(b)

Figure 5.24: (a) EBSD map of a completely self-annealed 1 μm-thick Cu film deposited at 30 mA/cm^2 (b) the corresponding grain size distribution. The EBSD scan was performed 8 days after deposition.

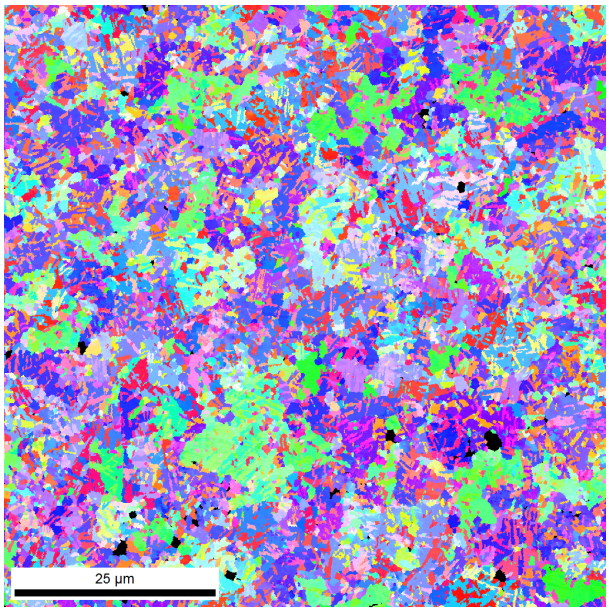

(a)

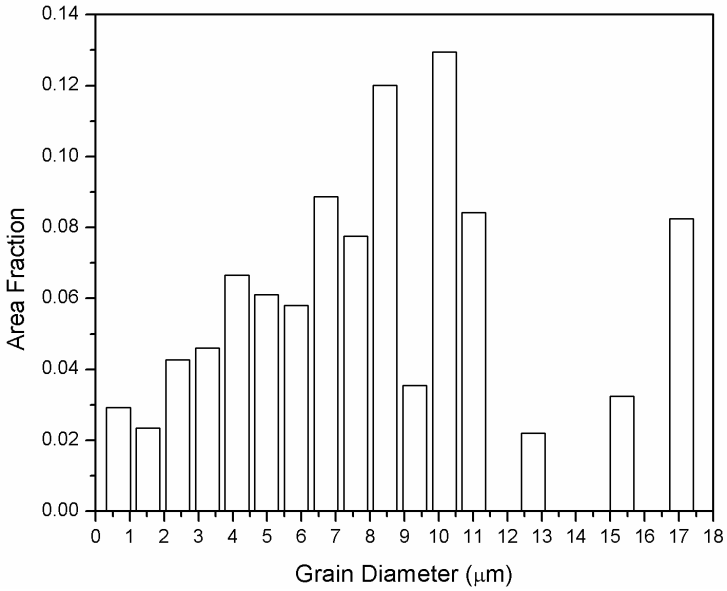

(b)

Figure 5.25: (a) EBSD map of a completely self-annealed 1 μm-thick Cu film deposited at 40 mA/cm^2 (b) the corresponding grain size distribution. The EBSD scan was performed 8 days after deposition.

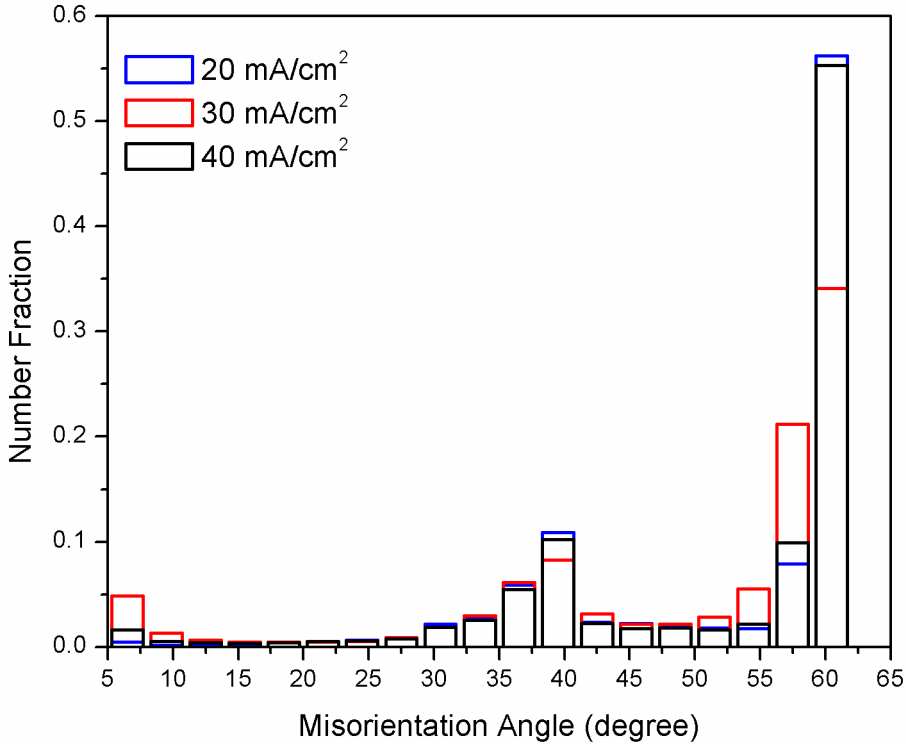

Figure 5.26: The misorientation profiles for completely recrystallized 1 μm-thick films that correspond to the orientation maps shown in Figs. 5.23-5.25.

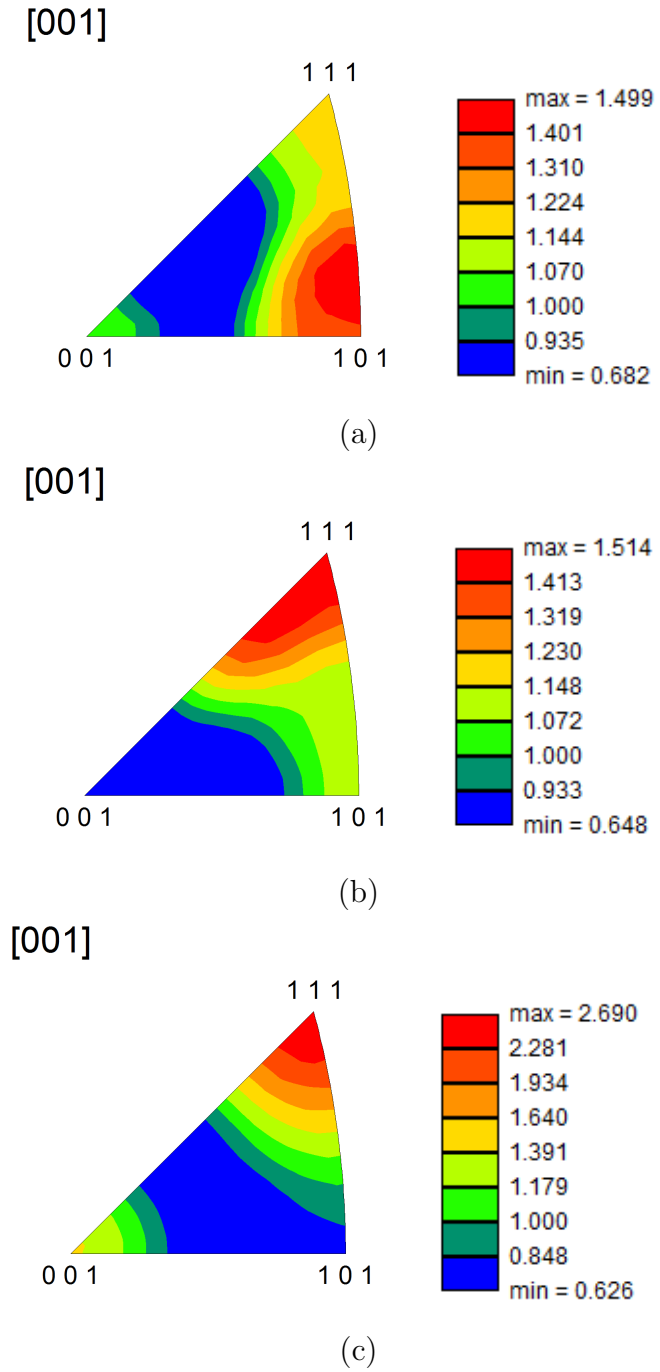

Figure 5.27: [001] Inverse pole figure of 1 μm-thick film that corresponds to the orientation maps shown in Figs 5.23-5.25 (a) 20 mA/cm^2 (b) 30 mA/cm^2 (c) 40 mA/cm^2.

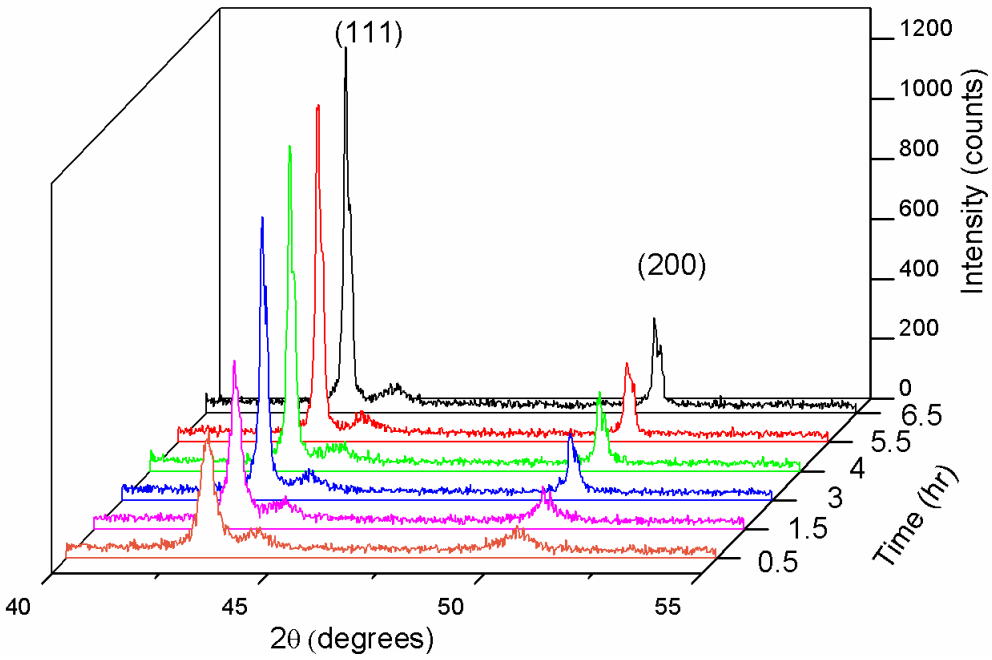

Figure 5.28: XRD profile of 1 μm-thick film deposited at 40 mA/cm^2 as a function of time after deposition.

5.6 Discussion

Table 5.5 compares the as-deposited resistivity and grain size as a function of the deposition current density. Here, the resistivity measurement shows that the as-deposited resistivity for the film deposited at 10 mA/cm^2 is lower than that for films deposited at 30 and 40 mA/cm^2. The EBSD maps show the trend that the initial grain size decreases as the deposition current density increases but the variation in the grain size is not very significant (grain size is approximately 150 nm). Using the Mayadas-Shatzkes model, the measured initial grain size for the films deposited at 10 and 40 mA/cm^2 are within the expected range. On the other hand, the EBSD grain size corresponding to the 30 mA/cm^2 deposition current density appears to be 8% higher than what is expected from MS model (this is insignificant since the coefficient of variation for resistivity measurement for this case is about 7%, see Table 5.3). The fact that the resistivity is sensitive to the deposition current density may be related to the presence of high defect density in the as-deposited microstructure for films produced at high deposition density.

The minor decrease in resistivity during the incubation period is due to the recovery process which seems to commence immediately after deposition for the cases presented here. During this stage, dislocations start to annihilate. It is possible that the organic additives incorporated in the film start to decompose and diffuse away from the bulk of the film toward the surface, which may alter the grain boundary properties and the associated electron scattering. The work of Stangl et al. [47] seems to support this theory where the researchers found an increase of carbon concentration at the film surface during the incubation period. The drop in resistivity during the incubation

Table 5.5: A summary of the resistivity and initial grain sizes for the 1 μm-thick film studied in this work.

Current density (mA/cm^2)	ρ_0 ($\mu\Omega$.cm)	G (nm) (EBSD)	G (nm) (MS model)	
			$\omega = 0.2$	$\omega = 0.5$
10	2.02	160	65	260
30	2.31	155	36	143
40	2.26	140	39	156

period, ρ_{inc}, seems to be linear with $\ln(t)$ and the model that was developed by Stangl and Militzer [65], i.e. $\rho_{inc} = 0.9939 - 0.0043\ln(t)$, appears to describe this behavior well for the results presented here despite the fact that the bath chemistry that was used in this study is different than that used by Stangl and Militzer (see Fig. 5.29). The onset of recrystallization can be determined from the point where the resistivity profile deviates from ρ_{inc}. Here, the length of the recovery stage is 28, 7.5, 2.0 and 0.8 hours for films deposited at 10, 20, 30 and 40 mA/cm^2, respectively.

Self-annealing, when described as a recrystallization phenomenon, can be explained by the tendency of the system to minimize the stored energy. Nuclei that are dislocation-free form and then grow due to the difference between the stored energy across both sides of the boundary. As the recrystallized grains increase in size, grain boundaries are eliminated that are associated with the small nonrecrystallized grains. This leads to a sharp drop in the resistivity since the electron scattering contribution from grain boundaries is reduced. The self-annealing rate dependence on the deposition current density, shown in Fig. 5.4, indicates that the driving pressure for self-annealing increases with the deposition rate.

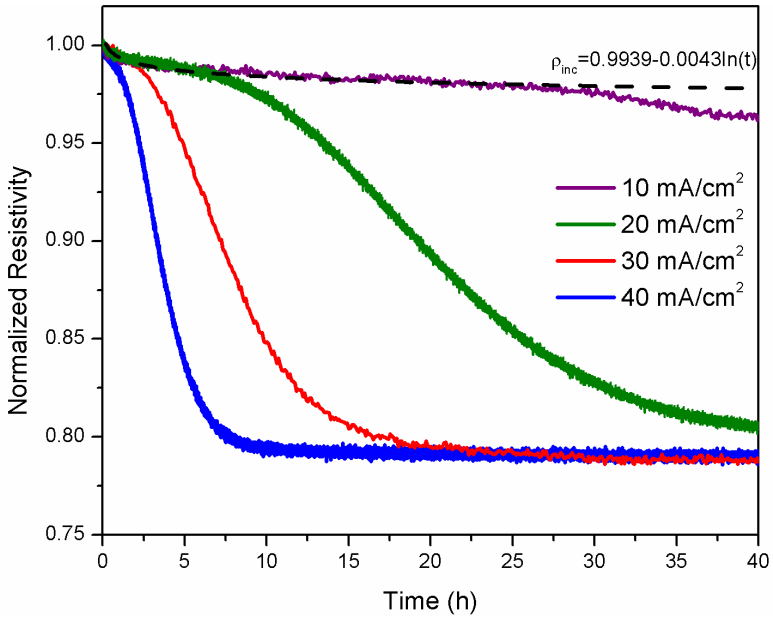

Figure 5.29: The determination of the onset of recrystallization as a function of the deposition current density.

Lagrange et al. [67] explained the strong effect of the film thickness by the fact that grain boundaries in thin films (e.g. 0.25 μm) can be easily pinned by particles while the grains in thicker films are not significantly affected by these particles (i.e. pinning is more effective in 2D). The researchers found that the initial stress is not dependent on the film thickness but the thinner films (as of 0.25 μm) showed larger stress change compared with the 0.75 and 1 μm-thick films. In contrast, the work of Lee and Park [93] showed that the residual stress increases from 0.1 to 0.6 GPa as the film thickness increases (0.25-2.5 μm). The researchers found that the residual stress is due to the trapped PEG in the grain boundaries and suggested that the high strain around the PEG sites results in faster recrystallization in thick films (i.e. more nucleation sites for recrystallization for thicker films). Stress seems to have a

strong effect on microstructure evolution processes. For example, Mompiou et al. [141] performed in-situ straining experiments on nanocrystalline and fine grain Al samples at room and at intermediate temperatures and found significant stress-assisted grain growth. The dependance of self-annealing rate on film thickness (as shown in Fig. 5.3) is maybe due to different stress levels in the thin film samples.

The EBSD results presented here prove that self-annealing can be observed at the surface of the film and in-situ EBSD technique is powerful to track the different stages of this phenomenon. However, due to the limited scan speed and the carbon contamination issue, the recrystallization progress can not be tracked when very fast or very slow self-annealing is expected. In-situ EBSD provides the details of grain size evolution during self-annealing and a complete quantitative assessment of recrystallization can be obtained. Although XRD provides some texture information, the details of the microstructure (e.g. twins and local orientation spread) can only be obtained from EBSD. While the resistivity measurement describes the microstructure evolution in a larger volume of the film compared with a relatively small surface area in the case of EBSD, the correlation between the self-annealing rates in both cases seems to be reasonable. The size of the EBSD map, however, is limited (length scale of micrometer) which results in a reduced statistics. Moreover, EBSD provides only information about the surface of the sample and cannot record the recovery stage. On the other hand, resistivity is a volume measurement and provides better statistics (length scale of millimeter). Furthermore, the recovery and recrystallization stages can be distinguished based on the rate of resistivity change. The resistivity, how-

ever, does not provide insight into the microstructure phenomena that occur during self-annealing. The fact that recrystallization seems to initiate near the film/substrate boundary suggests that there are some preferred nucleation sites in the film (it may be possible that the residual stress plays a role to determine these sites as suggested by Lee and Park [93]).

5.7 Summary

Self-annealing was captured by in-situ EBSD and resistivity measurements for thin film electrodeposited copper. The resistivity shows a strong effect of the deposition current density and film thickness on self-annealing rate. Films that are less than 1 μm-thick undergo very slow self-annealing. The resistivity showed that self-annealing occurs in the first 200 hours following the deposition when the current density is 10 mA/cm^2 or higher. On the other hand, no indication of self-annealing was observed for the film deposited at 5 mA/cm^2 even after about 1 week following the deposition. In-situ EBSD results confirmed that the observed drop in resistivity is accompanied by significant changes in the film microstructure. During self-annealing, changes in grain size, image quality and local orientation spread were observed. The changes in grain size and grain average image quality correlate well with the change in resistivity. The agreement between in-situ EBSD and resistivity data improves as the fraction recrystallized increases. This finding suggests that recrystallization appears to start near the substrate and then proceeds towards the film surface. The evolution of the Cu (111) peak from XRD agrees with the texture information that are obtained from EBSD.

Chapter 6

Recrystallization of Electrodeposited Copper Thin Films During Annealing

6.1 Introduction

In this chapter, recrystallization of 1 μm-thick copper films was studied during isothermal and continuous annealing treatments. In section 6.2, the effect of isothermal annealing on recrystallization rate is discussed. The continuous annealing treatment (resistivity-time and resistivity-temperature profiles) is covered in section 6.3 along with the effect of heating rate on recrystallization temperature. Section 6.4 deals with the activation energy for recrystallization. The information about the activation energy was then used to develop a phenomenological model to describe recrystallization during annealing. This model (presented here in section 6.5) was then used to develop a process map to describe recrystallization in electrodeposited copper thin films.

6.2 Isothermal Annealing

The normalized resistivities of 1 μm-thick films at three different temperatures are shown in Fig. 6.1. Here, the resistivity profile is normalized by the initial resistivity value at the corresponding holding temperature. It can be seen that the incubation period ranges from a few minutes to several hours depending on the holding temperature. After the incubation period, recrystallization is observed. The change in resistivity due to recrystallization is usually about 20%. The initial resistivity at 60 °C is higher than that at 40 °C and 20 °C, which slightly reduces the relative resistivity drop. The trend of the initial resistivity is complicated by the fact that the resistivity increase with temperature may in part be mitigated by recovery occurring during the heating stage. Increasing the temperature from 20 °C to 60 °C results in a reduction in the incubation period and acceleration of the recrystallization process. Approximately 20 min are required to achieve 50% recrystallization at 60 °C compared with 20 h at 20 °C. However, recrystallization at 20 °C occurs without introducing heat to the sample (i.e., the sample undergoes self-annealing).

6.3 Continuous Annealing

An example of resistivity measurement during continuous heating and cooling cycle is shown in Fig. 6.2. During the initial stage of continuous heating, the film resistivity increases linearly with temperature due to the increase in electron scattering. Subsequently, the resistivity decreases gradually, indicating an increase in the average grain size of the film due to recrystallization.

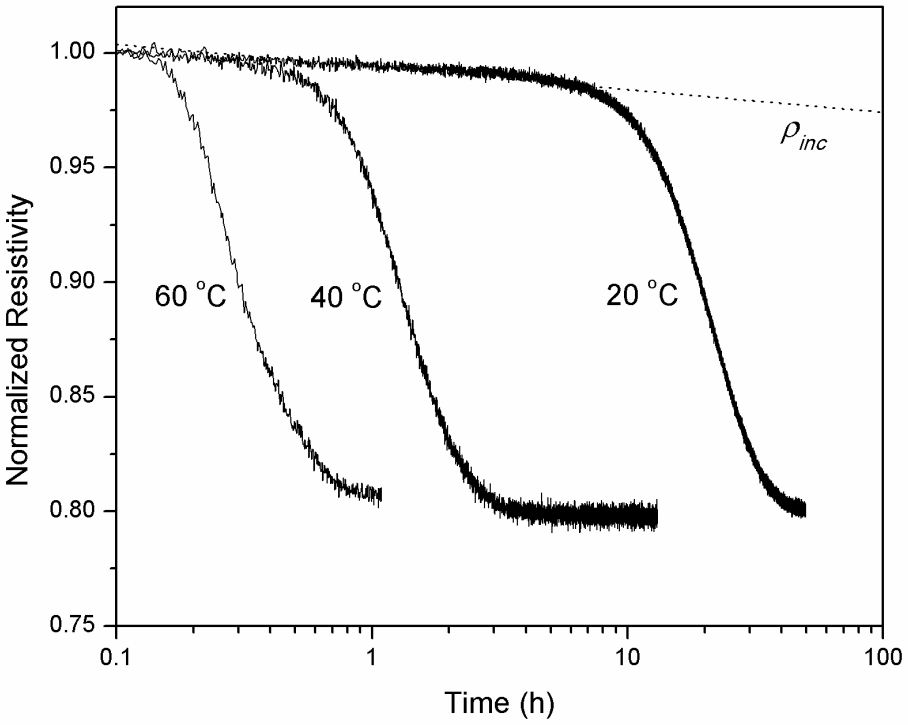

Figure 6.1: Normalized resistivities as a function of time after deposition of 1 μm-thick copper films that were deposited at 20 mA/cm^2 and then isothermally annealed at different temperatures. [142]

After recrystallization is complete, the resistivity resumes its linear increase with temperature. Upon cooling, the resistivity decreases linearly, reaching a level that is comparable to the nominal resistivity at room temperature. However, the change in film resistivity that occurs during heating is irreversible (Fig. 6.3). It was observed that there is a difference between the slope of resistivity-temperature profile during heating and that during cooling. The slope during heating for the case of the film deposited at 20 mA/cm^2

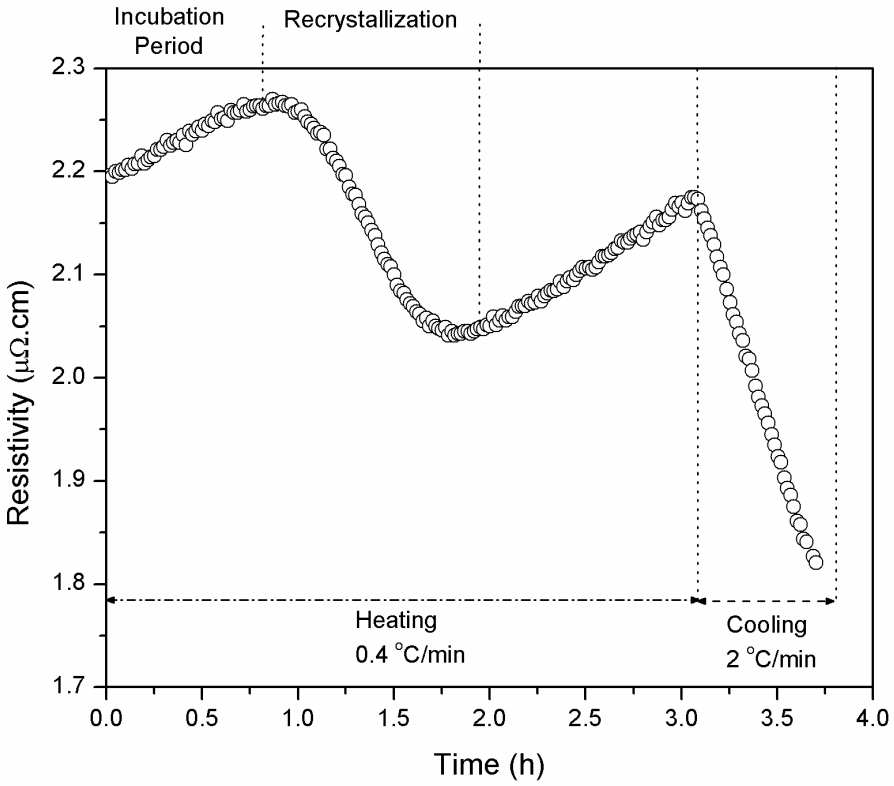

Figure 6.2: Resistivity-time profile during continuous heating/cooling treatment 1 μm-thick copper film deposited at 40 mA/cm^2. [142]

(line A in Fig. 6.3) was 0.0029 $\mu\Omega$.cm/ °C compared with 0.0043 $\mu\Omega$.cm/ °C when recrystallization is complete (line B in Fig. 6.3). Here, the difference in the slope before and after recrystallization is due to the recovery process that was also observed during the incubation period of isothermally annealed samples.

Similar to the trend shown in the self-annealed films in Fig. 5.4, the recrystallization kinetics during annealing is sensitive to the deposition con-

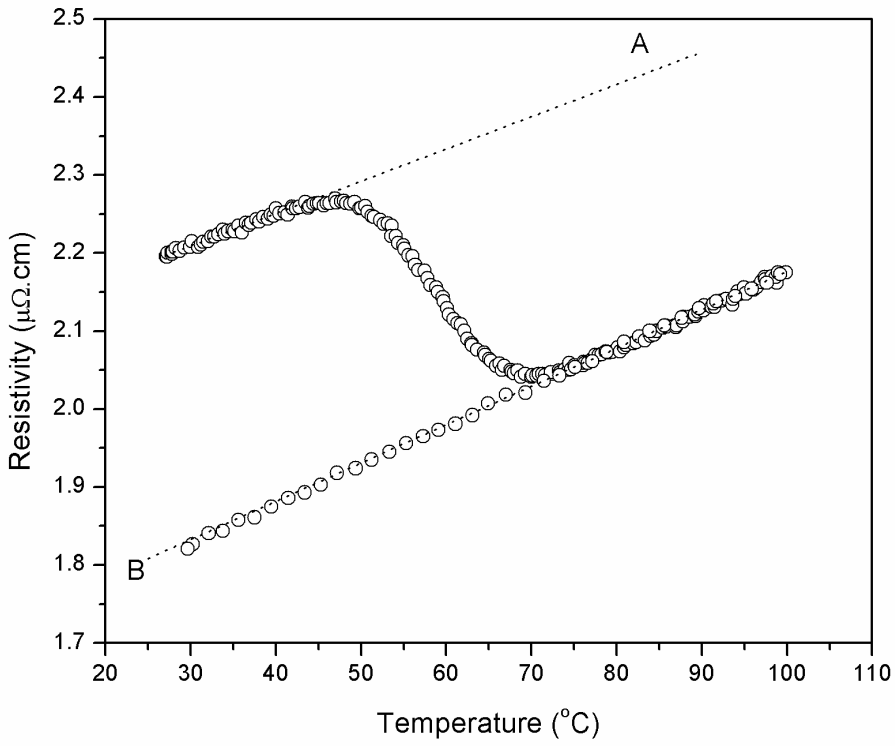

Figure 6.3: The corresponding resistivity-temperature profile for Fig. 6.2. [142]

ditions. This is illustrated in Fig. 6.4 where films electrodeposited using higher current density show faster recrystallization during continuous heating, which is also consistent with the TEM observations of Lee et al. [66]. Here, the stored energy difference is responsible for the variation in the recrystallization temperature. The fraction recrystallized during continuous heating is calculated from the law of mixture taking the effect of temperature on resistivity into account, i.e.

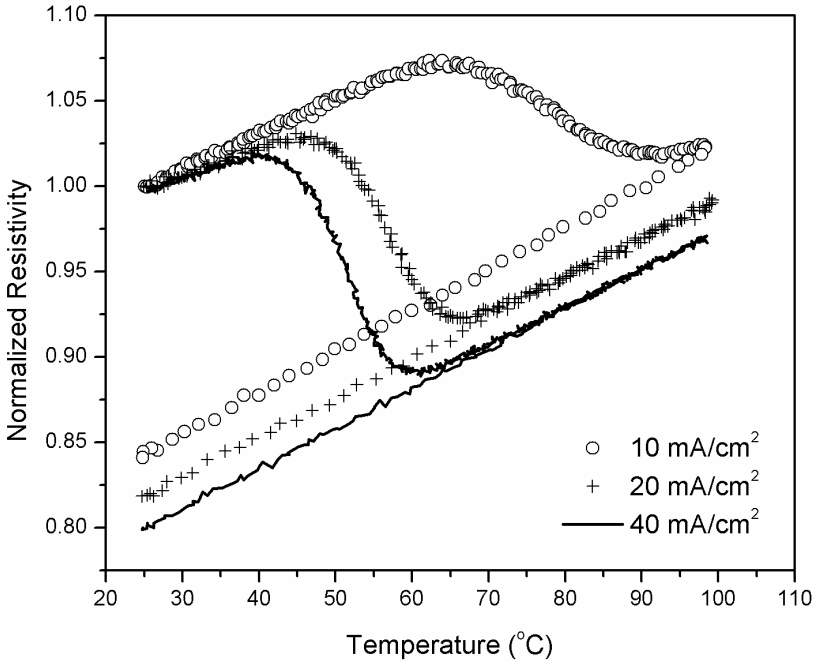

Figure 6.4: Effect of deposition current density on the resistivity of 1 μm-thick copper films during continuous annealing. The films were heated at 0.4 °C/min to 100 °C and then air-cooled to room temperature. [142]

$$f = \frac{\rho_0(T) - \rho(T)}{\rho_0(T) - \rho_\infty(T)} \tag{6.1}$$

where $\rho_0(T)$ is the resistivity of the nonrecrystallized material, i.e., line A in Fig. 6.3, and line B represents $\rho_\infty(T)$. The recrystallization of copper thin films also depends on the heating strategy. For copper interconnects, it is crucial to achieve a stable (i.e., recrystallized) microstructure within a reasonable time period. For thin films produced from the same chemical bath and at the same deposition conditions, it was observed that the heating rate has a strong influence on the recrystallization temperature. This effect is shown in Fig. 6.5 for different heating rates when the temperature is ramped

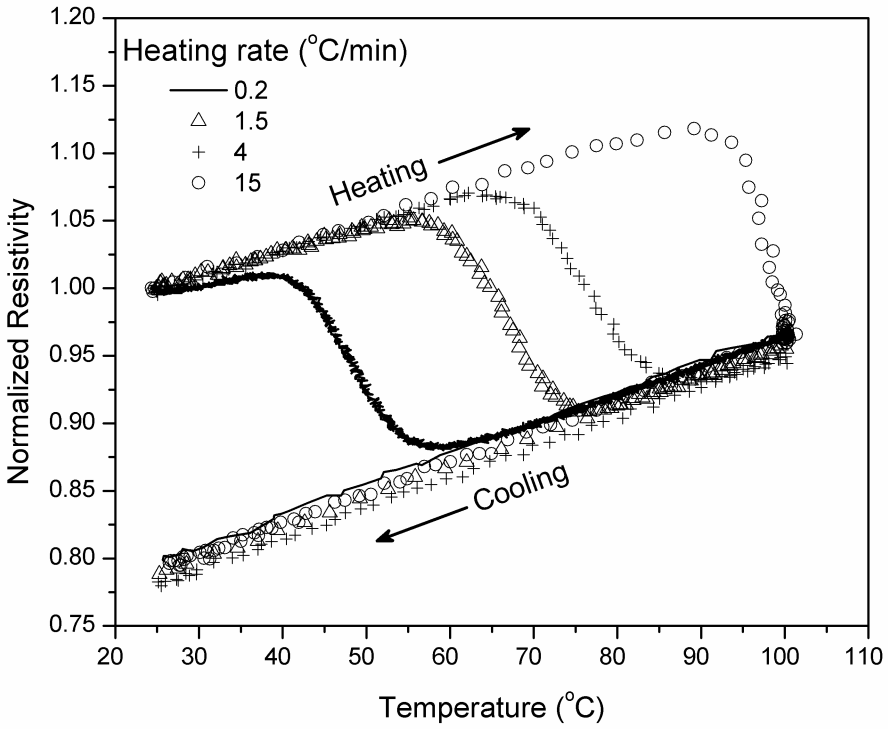

Figure 6.5: Normalized resistivity of 1 μm-thick Cu films continuously annealed at different heating rates. After reaching 100 ℃, all samples were air-cooled at a rate of 10 ℃/min. [142]

from 25 ℃ to 100 ℃. The temperatures for the onset and completion of recrystallization increase with increasing heating rate. At a low heating rate of 0.2 ℃/min, recrystallization occurs between 40 ℃ and 60 ℃, whereas for the highest heating rate employed in this study (15 ℃/min), recrystallization takes place between 90 ℃ and 100 ℃. This trend is summarized in Table 6.1, which gives the temperatures for 50% recrystallization. Furthermore, the relative change in resistivity that results from the recrystallization does

Table 6.1: Effect of heating rate on the recrystallization temperature and time of 1 μm-thick films deposited at 20 mA/cm^2. [142]

Heating Rate (°C/min)	Time$_{50\%Rex}$ (h)	Temperature$_{50\%Rex}$ (°C)
0.2	1.95	48
1.5	0.48	67
2	0.38	69
3	0.28	75
4	0.22	77

not depend on the heating rate (20%).

6.4 Activation Energy for Recrystallization

Using Eq. 2.11, the apparent activation energy for recrystallization can be computed from the isothermal resistivity profiles in Fig. 6.1. A plot of $\ln(t_{50\%})$ versus $1/k_BT$ gives a straight line with slope of Q. The value of Q obtained using this method is 0.89 eV (see Fig 6.6). Mathematically, $t_{50\%}$ (in hours) is described by

$$t_{50\%}\,(h) = 8.38 \times 10^{-15} \exp\left(\frac{10,328K}{T}\right) \tag{6.2}$$

The activation energy can also be computed from the continuous heating experiments. Similar to analysing differential scanning calorimetry (DSC) data, the Kissinger's analysis (Eq. 2.16) can be applied to compute the activation energy for recrystallization of electrodeposited thin films based on resistivity measurements. In doing so, T_P is taken as the temperature at which 50% recrystallization is achieved, as shown in Table 6.1. As illustrated in Fig. 6.7, the activation energy for Cu recrystallization is 0.93 eV, which

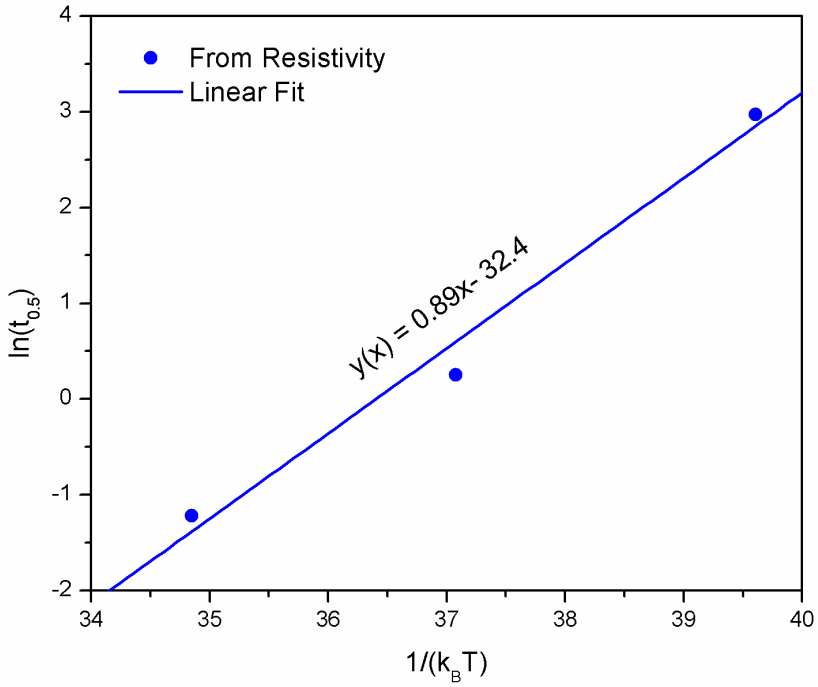

Figure 6.6: The relation between the time for 50% recrystallization and holding temperature. The activation energy for recrystallization is obtained by fitting the resistivity data.

compares well to the activation energy obtained from isothermal data (0.89 eV). Furthermore, this activation energy is similar to that of grain boundary self diffusion in Cu (0.92 eV) [108] and agrees well with the work of Detavernier et al. [88] (0.92 eV for films continuously annealed at 0.01-10 °C/min) and Cabral et al. [143] (0.92 ± 0.19 eV for films annealed at 10-280 °C/min) on 970 nm-thick Cu films.

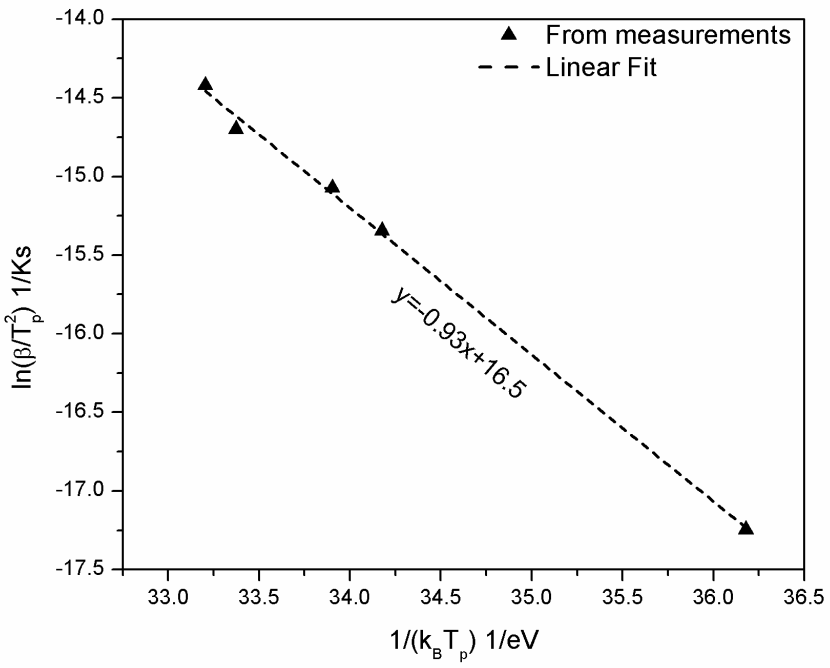

Figure 6.7: Applying Kissinger's analysis to compute the activation energy from continuous annealing resistivity measurements. [142]

6.5 Modelling of Recrystallization During Annealing

Similar to the models available in the literature which describe self-annealing using the JMAK model (i.e. Eq. 2.19), the recrystallization in Cu films during isothermal annealing can be described using the JMAK model. Here, the parameter b will be temperature-dependent, i.e.

$$f = 1 - \exp\left(-b\left(T\right)t^{n}\right) \tag{6.3}$$

The rate parameter $b(T)$ is frequently described by an Arrhenius relation, i.e.,

$$b(T) = b_0 \exp\left(-\frac{Q_{rex}}{k_B T}\right) \tag{6.4}$$

Here Q_{rex} represents another effective activation energy for recrystallization that is related to Q by $Q_{rex} = nQ$, and b_0 is a pre-exponential factor. To calculate the fraction recrystallized during continuous annealing treatment, the additivity rule needs to be verified for the reaction. This rule states that a nonisothermal path can be discretized into many isothermal stages with small time duration such that the fraction recrystallized, f, is attained at time t_f when

$$\int_{t_0}^{t_f} \frac{dt}{\tau(T)} = 1 \tag{6.5}$$

where $\tau(T)$ is the the time required to achieve a certain fraction recrystallized isothermally, and t_0 is the initial time. Cahn [144] proposed that any isokinetic reaction is additive (i.e., when the reaction rate depends on either its nucleation or growth rate, or the nucleation and growth rates have the same temperature dependence). The work of Donthu et al. [106] revealed that nucleation in electrodeposited copper thin films is site saturated; the reaction is thus growth controlled. This is consistent with the same activation energies obtained in the present study for isothermal and continuous heating experiments; i.e., additivity is expected to apply for recrystallization in electrodeposited Cu films. Mathematically, the additivity rule is valid if the transformation rate can be written in terms of two separate functions, $g(T)$ and $u(f)$, such that

$$\frac{df}{dt} = g\left(T\right) u\left(f\right) \tag{6.6}$$

The transformation rate can be obtained from Eq. 6.3, i.e.,

$$\frac{df}{dt} = nb^{\frac{1}{n}} \left(1 - f\right) \left(\ln\left(\frac{1}{1-f}\right)\right)^{\frac{n-1}{n}} \tag{6.7}$$

Comparing Eq. 6.6 with Eq. 6.7, a JMAK reaction is additive if the exponent n is constant over the entire temperature range. Starting from the additivity principle, Ferry et al. [145] developed a model to describe the recrystallization kinetics during a heating–holding–cooling cycle. The model is described by

$$f = 1 - \exp\left(-X^n\right) \tag{6.8}$$

where

$$X = \int_{T_0}^{T_1} \frac{b\left(T\right)^{\frac{1}{n}}}{\beta_h} dT + b\left(T_h\right)^{\frac{1}{n}} t_h + \int_{T_1}^{T_2} \frac{b\left(T\right)^{\frac{1}{n}}}{\beta_c} dT \tag{6.9}$$

Here, β_h and β_c are the heating and cooling rates, while t_h is the holding time at temperature T_h. The first term in X represents the contribution during heating, the second term represents the contribution of the holding stage, and the third term describes the effect of the cooling stage on the fraction recrystallized. Similar to the procedure used by Uedono et al [111] and Hau-Riege et al. [92], the JMAK parameter n can be obtained from the isothermal profiles by applying Eq. 2.20 for each temperature profile (i.e. plotting $\ln[-\ln(1-f)]$ versus $\ln(t)$). As summarized in Table 6.2, the n value increases somewhat with temperature, i.e., from 2.1 at 20 °C to 2.6 at 60 °C. For self-annealed samples, Stangl and Militzer [65] suggested that n is

Table 6.2: JMAK parameters obtained from isothermal resistivity profiles in Fig. 6.1. [142]

Temperature (°C)	n
20	2.1
40	2.2
60	2.6

less than 3 due to the heterogeneous distribution of stored energy in the film, which tends to lower the overall value of n. The observation of an increasing value of n with temperature may then indicate that extended recovery during the heating stage may reduce the degree of heterogeneity of the stored energy distribution. However, from the results in Table 6.2 , it is still reasonable to adopt an average n value ($n = 2.3$) independent of temperature. Assuming $n = 2.3$, the rate parameter $b(T)$ in Eq. 6.3 can be expressed in terms of $t_{50\%}(T)$ by

$$b\left(T\right) = -\frac{\ln\left(0.5\right)}{\left(t_{50\%}\left(T\right)\right)^{n}} \tag{6.10}$$

where $t_{50\%}\left(T\right)$ is described by Eq. 6.2. This overall JMAK model provides a reasonable description of the fraction recrystallized for all temperatures, as shown in Fig. 6.8 . Assuming a constant n value over the temperature range of interest, the additivity principle can be applied to predict the nonisothermal fraction recrystallized based on the isothermal results. The simulated fraction recrystallized is compared in Fig. 6.9 with the experimental results obtained during continuous heating. This comparison reveals that the recrystallization in electrodeposited copper films can, to a good approximation, be predicted using the additivity principle for the temperature range between 25

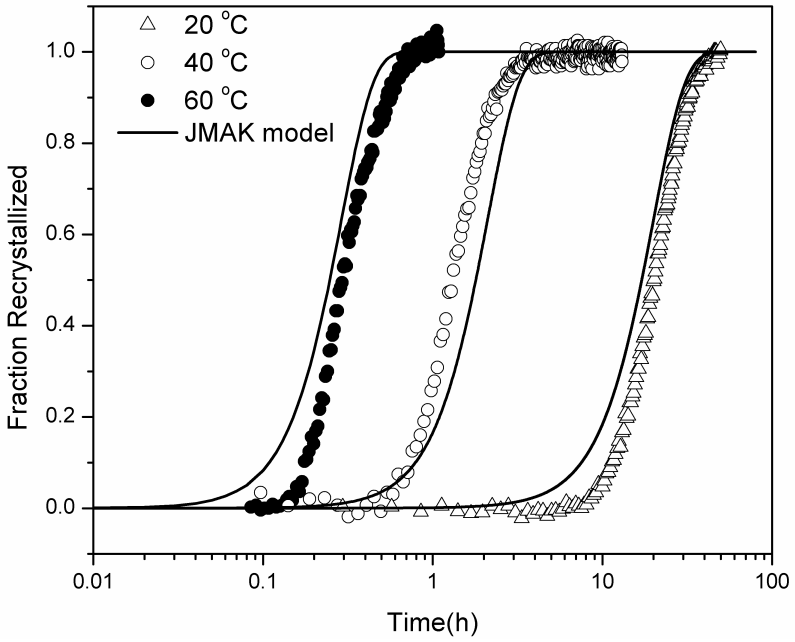

Figure 6.8: Comparison between the fraction recrystallized as obtained from isothermal experiments and as predicted by the JMAK model. [142]

°C and 100 °C. The difference between the model prediction and the experimental results for the high heating rate of 15 °C/min may be attributed to the assumption of constant n. The results in Table 6.2 indicate an increase of n with temperature. Furthermore, the JMAK parameters n and $b(T)$ were determined for temperatures up to 60 °C, whereas for the highest heating rate, recrystallization occurs above 80 °C.

Figure 6.10 shows the model prediction for the time required to complete recrystallization (i.e., $f = 0.95$) as a function of heating rate and annealing temperature. This figure can be useful as a process map to evaluate recrystallization during a continuous treatment that includes heating to an annealing temperature and followed by a holding stage. The time required for recrystal-

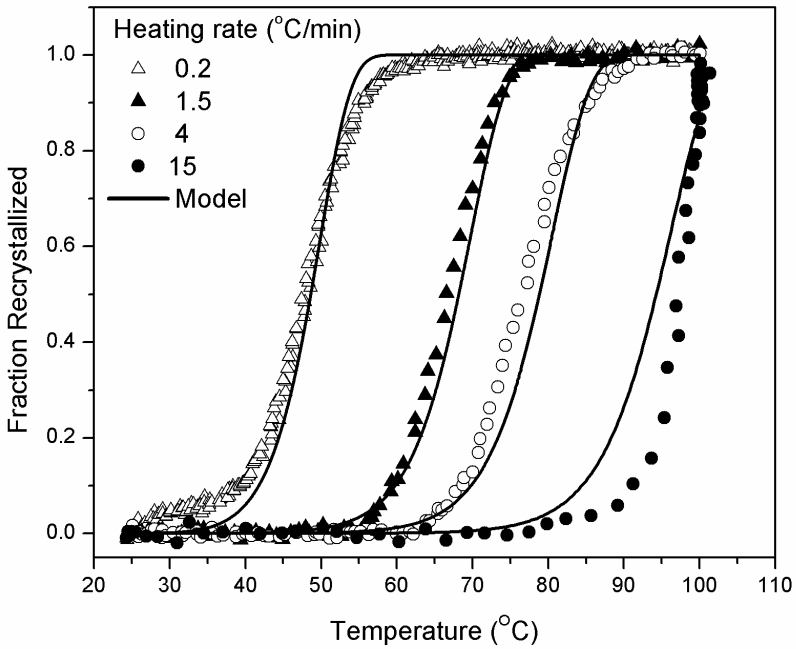

Figure 6.9: Comparison between the fraction recrystallized as obtained from nonisothermal resistivity measurements and the model predictions. [142]

lization varies from 0.1 h to 8 h for the range of heating–annealing strategies depicted. For heating rates and temperatures below curve A, no recrystallization occurs during continuous heating and complete recrystallization will occur during holding. Above curve B, recrystallization is complete before the annealing temperature is reached. However, the map should be specified for each deposition condition (deposition current density, bath chemistry, and film thickness) for a complete description of recrystallization in thin films. Furthermore, it is still necessary to evaluate whether or not additivity holds for a wider range of heating rates and temperatures above 100 °C. This will

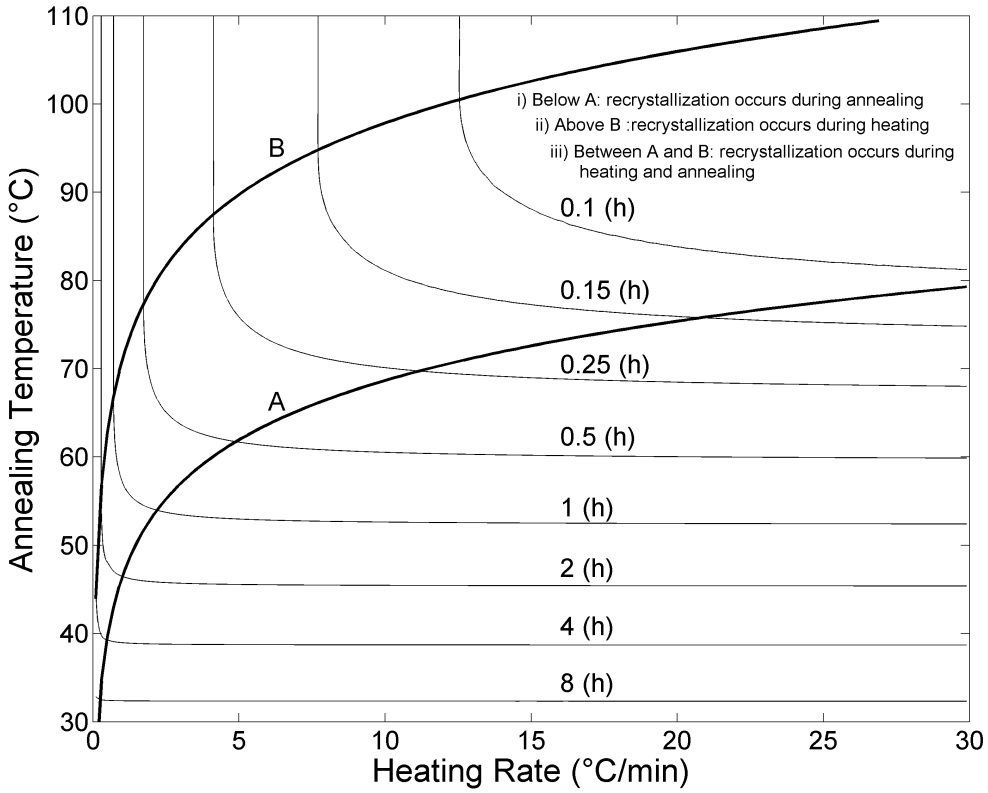

Figure 6.10: Contour plots of the model predictions for the total time (in hours) required for complete recrystallization (i.e., $f = 0.95$) as a function of heating rate and annealing temperature. [142]

be quite useful for industrial processes, which may involve temperatures as high as 400 ℃ [105].

6.6 Summary

In this chapter, recrystallization of 1 μm-thick electrodeposited copper thin films was investigated during isothermal and during continuous heating. The

recrystallization rate can be significantly accelerated by moderate annealing treatment (40-100 °C). There is a difference in the slope of the resistivity-temperature profile during heating and that when recrystallization is complete. This difference is attributed to the recovery process that takes place during heating. The activation energy for recrystallization can be extracted from the isothermal or continuous heating profiles and is determined to be in the range of 0.89-0.93 eV. The heating rate in the continuous annealing treatment plays a key role in determining the recrystallization temperature. Using the isothermal data, a JMAK model was developed and then, adopting additivity, applied to continuous annealing conditions. The model produced a reasonable prediction when compared with the experimental results. These results suggest that the recrystallization in Cu thin films during annealing is additive. A process map was then developed to describe the total recrystallization time as a function of heating rate and holding temperature. A complete process map should involve other variables including the film thickness and deposition current density.

Chapter 7

Recrystallization of Electrodeposited Copper Thin Films Produced by Novel Deposition Strategies

7.1 Introduction

In the Damascene process, copper superfilling is normally achieved by deposition at low current density. Chang et al. [146] observed optimum filling (superconformal deposition) at 3.33 mA/cm^2 deposition current density but poor filling quality was observed at 10 or 13.33 mA/cm^2 deposition current densities. As explained by the researchers, the high current densities result in a deposition rate that is too high at the shoulder of vias and trenches. From the resistivity data shown in chapter 5, films that are deposited using low current density undergo a very slow self-annealing process (8 days are not enough to detect the onset of recrystallization when the film is deposited at 5 mA/cm^2 current density). As a result, annealing treatment at elevated temperatures (e.g. 400 °C) is normally required in the processing of copper

interconnects to obtain a recrystallized microstructure in a reasonable time. As the interconnect line width continues to decrease, even lower current densities are expected to be used in the Damascene process such that higher annealing temperature (or longer annealing time) may be required. The processing temperature for the low-K dielectric materials is often limited. Thus, a method to accelerate the recrystallization process without increasing the processing temperature will be of significance. Section 7.2 of this chapter deals with a proposed deposition method to accelerate recrystallization in copper interconnects. The method is based on the deposition of a capping layer on top of Cu metal layer.

Since silver is being investigated as a potential alloying element to further improve the strength and electromigration resistance of copper, section 7.3 deals with the effect of adding silver to the deposition bath on the microstructure evolution in Cu films. The idea here is to investigate whether recrystallization can still occur in Cu alloys. For this purpose, resistivity measurement was used to study recrystallization rate in the presence of silver at room and elevated temperatures.

7.2 Acceleration of Recrystallization by Variable Current Deposition

To investigate recrystallization in copper thin films using variable current densities, different samples were prepared using one or two deposition current densities. In sample 1, a 1 μm-thick film was entirely deposited at 5 mA/cm^2. Samples 2-4 were 1 μm-thick films that were deposited using two sequential

Table 7.1: A summary of the as-deposited resistivity as a function of the thickness of the 40 mA/cm^2 layer. The total film thickness was 1 μm.

Sample	Thickness of the 40 mA/cm^2 layer (μm)	As-deposited resistivity ($\mu\Omega$.cm)
1	0	1.99
2	0.2 (Top)	2.03
3	0.5 (Top)	2.12
4	0.8 (Top)	2.15
5	0.2 (bottom)	2.12
6	0.5 (bottom)	2.22
7	0.8 (bottom)	2.26

deposition procedures. First, a layer was deposited at low current density (here, 5 mA/cm^2) for a specified fraction of the total film thickness. In the second step, a layer was deposited at high current density (here, 40 mA/cm^2) until the total film thickness is achieved. Samples 5-7 were 1 μm-thick films that were produced using the reverse deposition order (i.e. deposition at high current density (here, 40 mA/cm^2) for a specified fraction of the film thickness followed by deposition at low current density (here, 5 mA/cm^2) until the total film thickness is achieved). Table 7.1 summarizes the as-deposited resistivities for all samples. The as deposited resistivity of sample 1 was 1.99 $\mu\Omega$.cm. This is lower than the resistivities of films deposited at higher current density (like 30 and 40 mA/cm^2 as discussed in chapter 5) but still corresponds to a nanocrystalline grain structure in the as-deposited microstructure. The low as-deposited resistivity value agrees with the trend that resistivity decreases as the deposition current density decreases. For sample 2, which is composed of 0.2 μm-thick layer deposited at 40 mA/cm^2 on top of 0.8 μm-thick layer deposited at 5 mA/cm^2, the resistivity is about

22% higher than the bulk resistivity of copper while for samples 3 and 4, the resistivity is 27-28% higher. For samples 5-7, the as-deposited resistivities are comparable with the corresponding resistivies for samples 2-4. Considering the standard deviation in the resistivity measurements of about 0.1 $\mu\Omega$.cm, the resistivity of all samples is within the expected range for a nanocrystalline microstructure (i.e. 2-2.4 $\mu\Omega$.cm).

All the samples were annealed at 60 °C to promote faster recrystallization. Figure 7.1-a shows the normalized resistivity as function of time after deposition for samples 1-4. In sample 1, the resistivity increases during heating and then a recovery period extends for about 4 hours. While the EBSD orientation map in Fig. 5.14 shows that 8 days were not enough to observe recrystallization at the surface of a 1 μm-thick film deposited at 5 mA/cm^2 when held at room temperature, recrystallization was observed at 60 °C. Here, about 44 hours were required to complete recrystallization while 50% recrystallization was obtained after 8.1 hours (see Table 7.2). On the other hand, less than one hour is sufficient to achieve 50% recrystallization for sample 2 while about 4 hours are sufficient to observe the resistivity plateau indicating complete recrystallization. Although this film was deposited using two different current densities, the shape of the resistivity profile seems to be similar to the resistivity profiles for films which are entirely deposited at a single current density (i.e. consist of an incubation period followed by a sharp drop in resistivity). As shown in Table 7.2, the final resistivity for this sample was 1.82 $\mu\Omega$.cm which implies final grain sizes that are in the order of 1 μm in diameter or larger. As the thickness of the top layer increases, faster recrystallization is observed as indicated from the resistivity

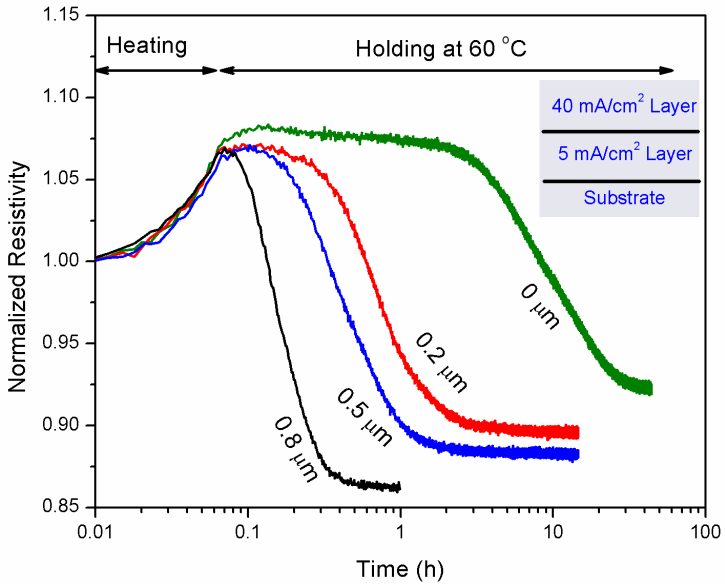

(a)

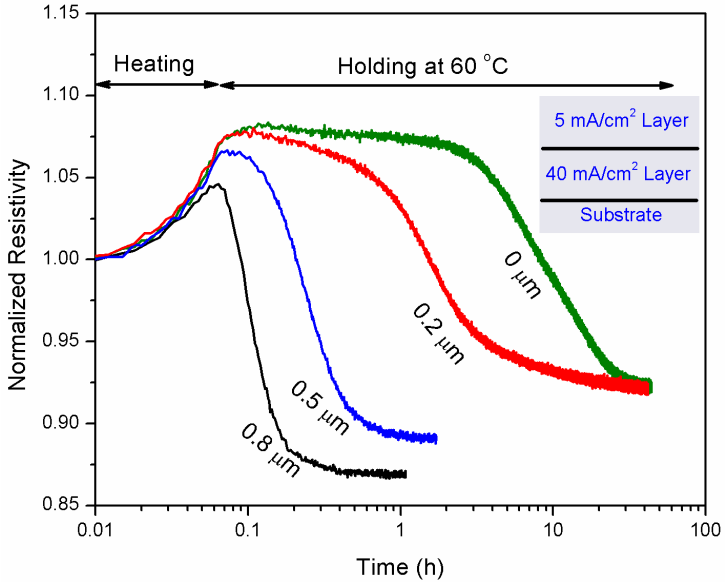

(b)

Figure 7.1: (a) Normalized resistivities for 1 μm-thick Cu films that were produced using two different deposition current densities (as shown in the figure inset). All films were heated from room temperature to 60 °C at 10 °C/min. The thickness of the layer deposited at 40 mA/cm^2 is shown next to its corresponding resistivity profile. In (b) the order of the deposition is reversed as shown in the figure inset.

Table 7.2: A summary of the resistivities and the time for 50% recrystallization for the films shown in Table 7.1.

	Sample						
	1	2	3	4	5	6	7
ρ_0(60 °C) ($\mu\Omega$.cm)	2.15	2.17	2.26	2.27	2.29	2.35	2.21
ρ_∞(60 °C) ($\mu\Omega$.cm)	1.83	1.82	1.86	1.85	1.96	1.97	1.96
$\frac{\rho_0-\rho_\infty}{\rho_0}\times 100$	15	16	18	19	15	16	11
$t_{50\%}$ (h)	8.1	0.7	0.4	0.17	1.53	0.25	0.13

profiles for sample 3 and 4. Here, less than half an hour is sufficient to obtain 50% recrystallization for the two films. The final resistivities for these two samples were 1.86 and 1.85 $\mu\Omega$.cm, respectively (i.e. correspond to recrystallized microstructures). It appears that the 40 mA/cm^2 layer acts as a seed layer for recrystallization were nucleation occurs in the top layer followed by recrystallization to consume the highly dislocated grains. Subsequently, recrystallization then proceeds to consume the layer deposited at the low current density. For 200 nm-thick capping layer as in the case of sample 2, an order of magnitude less time is sufficient to obtain complete recrystallization compared with the case when no capping layer is present (i.e. sample 1).

Figure 7.1-b shows the normalized resistivity profiles when the deposition order is reversed (i.e deposit a layer at 40 mA/cm^2 followed by a capping layer at 5 mA/cm^2). Here, a similar trend to that shown in Fig.7.1-a was observed (i.e. recrystallization occurs faster as the fraction of the 40 mA/cm^2 is increased). For this case, recrystallization initiates at the bottom of the sample (i.e. in the layer deposited at 40 mA/cm^2) and then proceeds towards

the sample surface. The recrystallization rate for sample 5 is slower than that for sample 2 (around 0.8 hour difference in their corresponding 50% recrystallization time). The final resistivity for this sample was 1.96 $\mu\Omega$.cm ($\approx$42 hours of holding time). Here, the time for 50% recrystallization for samples 6 and 7 is comparable with that for samples 3 and 4. This suggests that when the thickness for the layer deposited at 40 mA/cm^2 is 0.5 μm or thicker, recrystallization rate is very fast (less than 25 minutes are sufficient to obtain 50% recrystallized microstructure) and does not depend much on the location of the 40 mA/cm^2 layer (i.e. top or bottom). For sample 7 and as indicated in Table 7.2, the percentage change in resistivity is less than the other samples which is due to the fact that recrystallization occurs during heating (i.e. the resistivity at 60 °C is lowered).

Figure 7.2-a shows the EBSD orientation map and the corresponding image quality of the film deposited using the deposition conditions of sample 3. The SEM which was used in this study was not equipped with a heating stage so the film was left to recrystallize at room temperature (i.e. self-annealing). For the map that was obtained one day following the deposition, a partially recrystallized microstructure is observed with some grains having diameters greater than 1 μm. These grains are recrystallized grains as indicated by their relatively high image quality compared with the image quality that corresponds to the small grains in the microstructure. Figure 7.2-b shows the orientation map and the corresponding image quality for the same sample after 6 days following the deposition. Clearly, recrystallized grains have consumed the majority of the film area with some nonrecrystallized grains are still present in the microstructure. Another observation is that although

the resistivity measurement shows that 0.5 μm-thick film deposited at 40 mA/cm^2 did not undergo a change in resistivity in the first 24 hours after deposition (see Fig. 5.3), when the same thickness is placed on top of the 0.5 μm-thick layer deposited at 5 mA/cm^2, significant recrystallization is detected in the 40 mA/cm^2 layer. In this case, recrystallization initiates away from the substrate where the interaction with the substrate is minimum. It is also possible that recrystallization initiates at the interface between the two layers due to the significant stored energy difference between the two sides of the interface.

When the deposition order is reversed (i.e. same conditions of sample 6), few recrystallized grains can be observed at the film surface after 1 day following the deposition as can be seen in the orientation map and the corresponding image quality shown in Fig. 7.3-a. This indicates that the 5 mA/cm^2 layer starts to recrystallize. In this particular case, nucleation initiates at the bottom layer and then recrystallization proceeds towards the top surface. Here, the recrystallized grains (those larger than 1 μm in diameter) are bigger than the recrystallized grains observed in sample 3 as can be seen in the grain size distribution shown in Fig. 7.4. However, after 6 days, the EBSD map shows an almost fully recrystallized microstructure (see Fig. 7.3-b). These EBSD results prove that the presence of a layer deposited at 40 mA/cm^2 either at the top or at the bottom of the film accelerates self-annealing compared with the case when the film is entirely deposited at low current density (as shown in Fig. 5.14). These results are in agreement with the resistivity profiles shown in Fig. 7.1 for annealing at 60 °C.

The acceleration of the recrystallization can be also observed at room

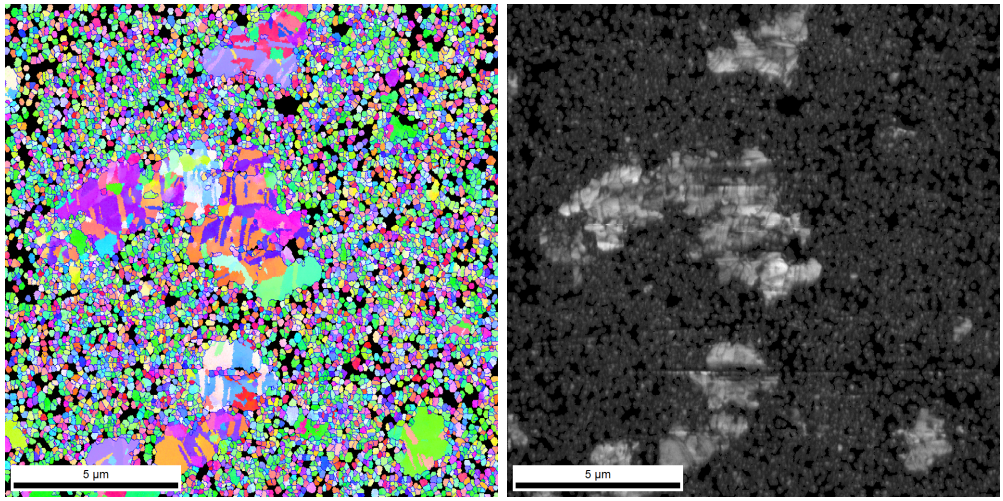

(a)

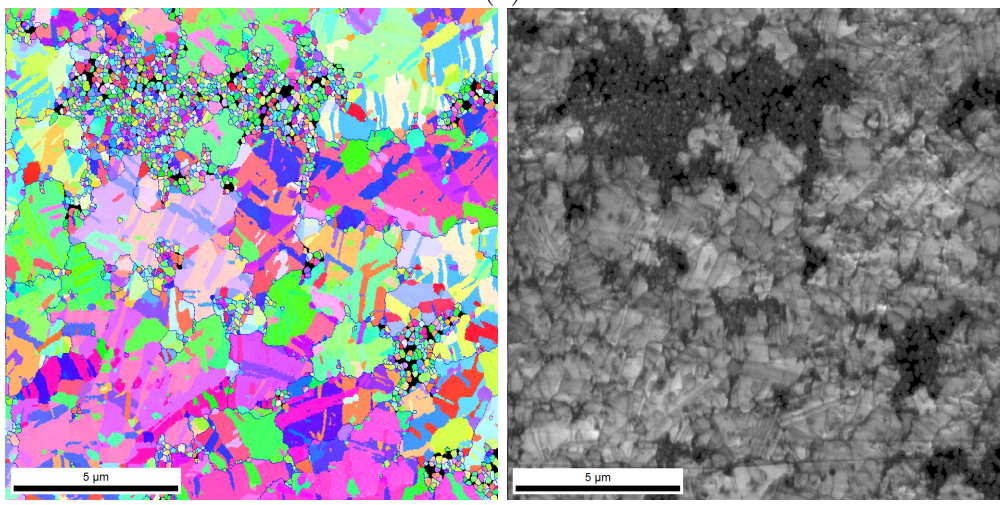

(b)

Figure 7.2: EBSD orientation map and the corresponding image quality of the film that was deposited using two subsequent deposition current densities (0.5 μm-thick layer at 5 mA/cm^2 followed by 0.5 μm-thick layer at 40 mA/cm^2) (a) 1 day after deposition (b) 6 days after deposition .

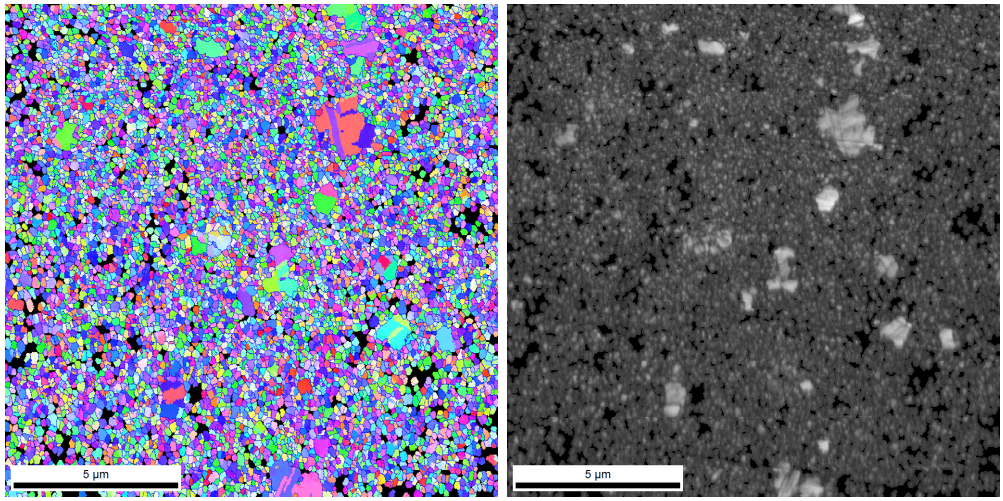

(a)

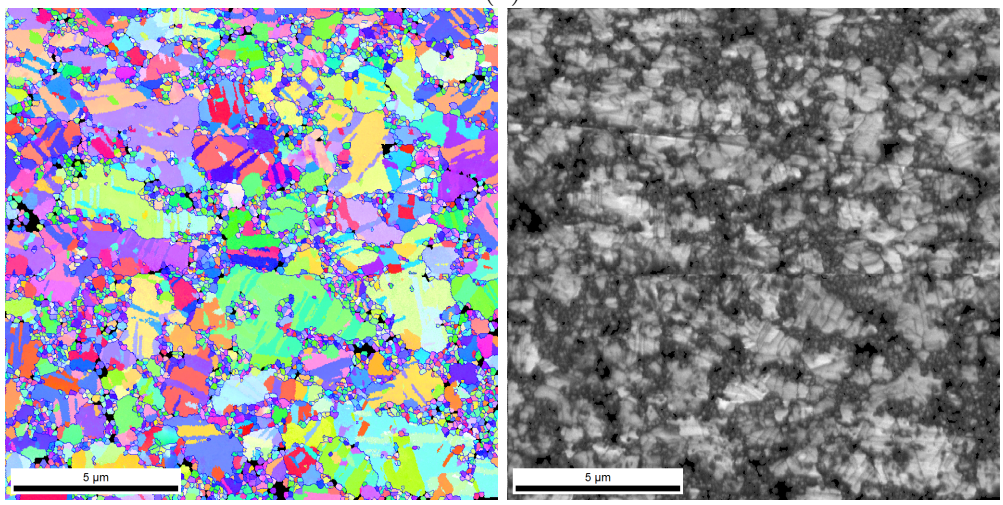

(b)

Figure 7.3: EBSD orientation map and the corresponding image quality of a film that was deposited using two subsequent deposition current densities (0.5 μm-thick layer at 40 mA/cm^2 followed by 0.5 μm-thick layer at 5 mA/cm^2) (a) 1 day after deposition (b) 6 days after deposition .

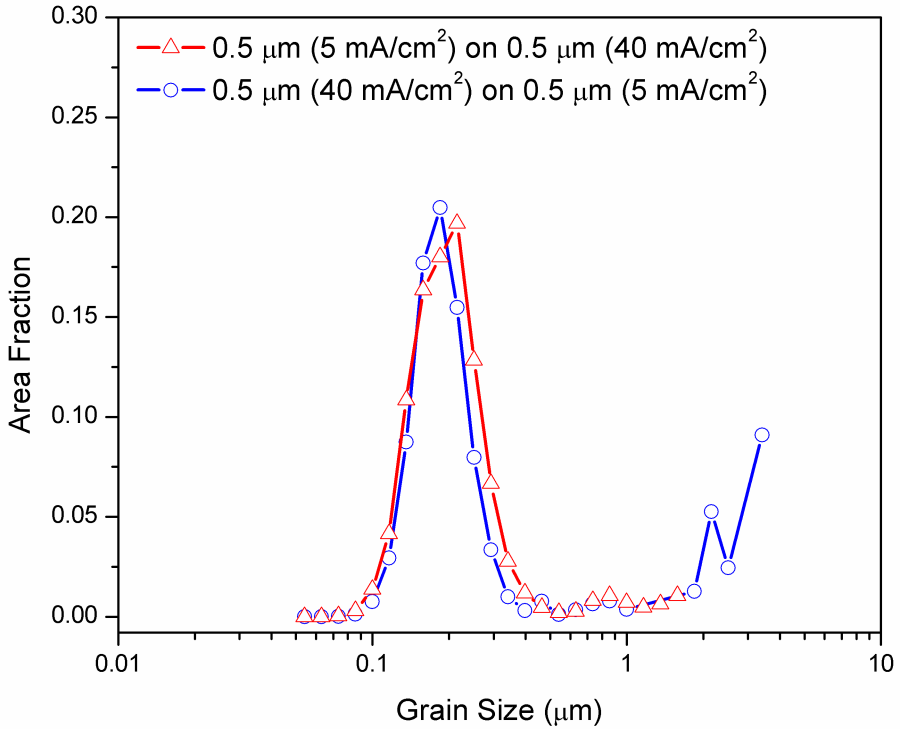

Figure 7.4: Effect of deposition order on the grain size distribution. In both cases, the film was 1 μm-thick and the EBSD scans were obtained 1 day after deposition.

temperature from the resistivity profiles. However, the film takes a longer time to recrystallize compared to the film that is annealed at a higher temperature (e.g. 60 °C). As shown in Figure 7.5, the resistivity profile that corresponds to the film deposited at variable current density (0.5 μm at 5 mA/cm^2 followed by 0.5 μm at 40 mA/cm^2) shows all the three stages of self-annealing (incubation stage, recrystallization and resistivity saturation). The initial and final resistivities for this sample were 2.13 and 1.74 $\mu\Omega$.cm, respectively (18.3 % resistivity drop). Compared with the film that was deposited at 5 mA/cm^2, the presence of the capping layer promotes recrys-

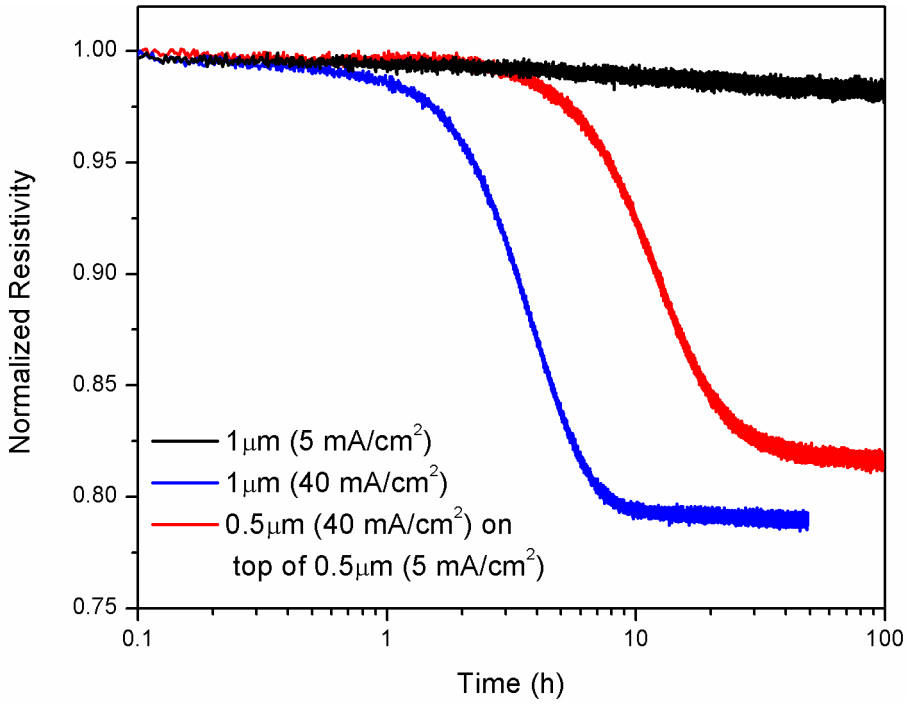

Figure 7.5: The effect of capping layer on the resistivity profile of 1 μm-thick films during self-annealing. The films that were entirely deposited at 5 and 40 mA/cm^2 are included for comparison.

tallization and the resistivity starts to saturate at around 40 hours following the deposition. However, the recrystallization rate for this film is still far from that for the film that was entirely deposited at 40 mA/cm^2 (complete self-annealing in about 10 hours). Comparing the resistivity profile shown in Fig. 7.5 with the EBSD orientation map shown in Fig. 7.2-a, it can be seen that the two techniques show recrystallization during the first 24 hours following the deposition.

7.3 Acceleration of Recrystallization in the Dual Damascene Process

Based on the resistivity and EBSD results presented above, we propose a new deposition strategy in the Dual Damascene process where a thin capping layer deposited at high current density is used as a seed layer for recrystallization. The proposed strategy is illustrated in Fig. 7.6. Here, superfilling of copper is achieved in trenches and vias by the aid of organic additives using low deposition current density (i.e. 5 mA/cm^2 or less). A thin capping layer is deposited on top of the overburden layer at high current density (i.e. 40 mA/cm^2). The thickness of this layer can be as thin as 200 nm. The wafer is then annealed at an appropriate holding temperature such that recrystallization is initiated in the capping layer. The wafer is then held for an appropriate holding time such that recrystallization proceeds in the overburden layer and in the trench/via. When recrystallization is complete and low resistivity is attained, CMP can be applied to remove the capping and the overburden layers.

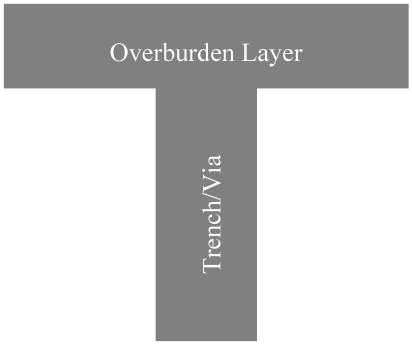

(a)

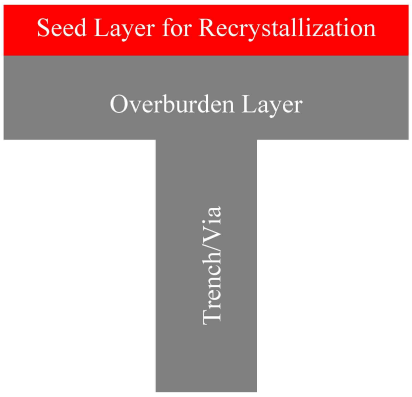

(b)

(c)

Figure 7.6: A proposed deposition strategy to accelerate recrystallization in copper interconnects. (a) achieve copper superfilling in trenches and vias by electrodeposition at low current density (b) deposit a thin copper film at high current density on top of the overburden layer (i.e. seed layer for recrystallization) followed by an appropriate annealing step and (c) remove the excess copper by CMP after recrystallization is complete.

7.4 Effect of Silver on Recrystallization Rate

When silver is added to an electrolyte containing chloride ions, the following chemical reaction occurs:

$$Ag^{+}_{(aq)} + Cl^{-}_{(aq)} \rightarrow AgCl_{(s)} \tag{7.1}$$

The outcome of the reaction is a precipitation of silver chloride which is a white solid material. To deposit copper-silver alloy, free silver must be present in the solution to co-deposit with copper. For this purpose, chloride was initially removed from the standard electrolyte. Figure 7.7 shows the normalized resistivity of a 2 μm-thick copper film during annealing when heated from room temperature to 100 °C (heating rate of 5 °C/min). The film was started to recrystallize during heating (at 88 °C) and completely recrystallized in about 0.5 hour. This indicates that the presence of chloride in the standard electrolyte is not critical for recrystallization to occur. To check if copper thin films can still recrystallize when silver is present in the solution, high purity silver (59 Grade, COMINCO) was dissolved in nitric acid and then added to the electrolyte bath (not containing chloride). In this way silver and copper co-deposition occurs. The as-deposited resistivity for this film was 2.31 $\mu\Omega$.cm which corresponds to a microstructure with nanocrystalline grains. However, the film was not shiny which indicates that the film quality is affected due to co-deposition with silver. As shown in Fig. 7.7, and even after about 5 hours of annealing at 100 °C, no resistivity drop was detected and when the film was air-cooled to room temperature, the film resistivity returned to the same initial resistivity value (i.e. as-deposited resistivity).

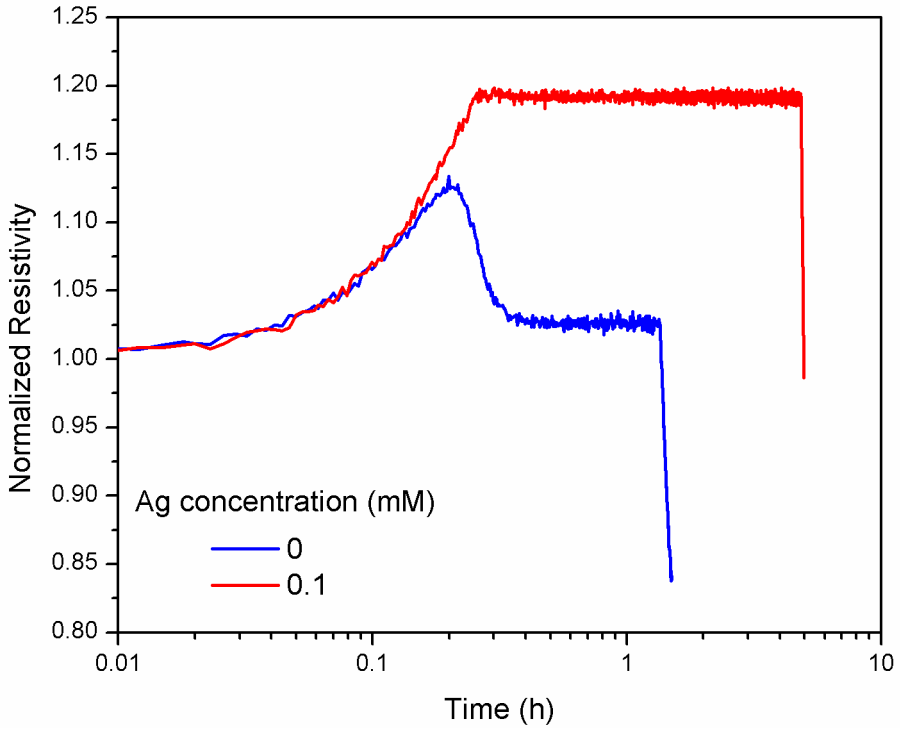

Figure 7.7: Effect of adding silver to the electrolyte (in the absence of chloride) on the normalized resistivity profile of 2 μm-thick copper film deposited at 20 mA/cm^2. The films were heated from room temperature to 100 °C at 5 °C/min.

This indicates that films which are electrodeposited in the presence of silver do not recrystallize with the present annealing treatment. Here, the amount of silver that is co-deposited with copper seems to be significant enough to pin the grain boundaries even at 100 °C. These results agree with the observation of Strehle [122, 124] who did not observe self-annealing in Cu-Ag alloy when chloride was absent. Although the researcher explained that the absence of additives and the effect of silver on grain boundary motion are responsible for not observing self-annealing, the present results indicate that

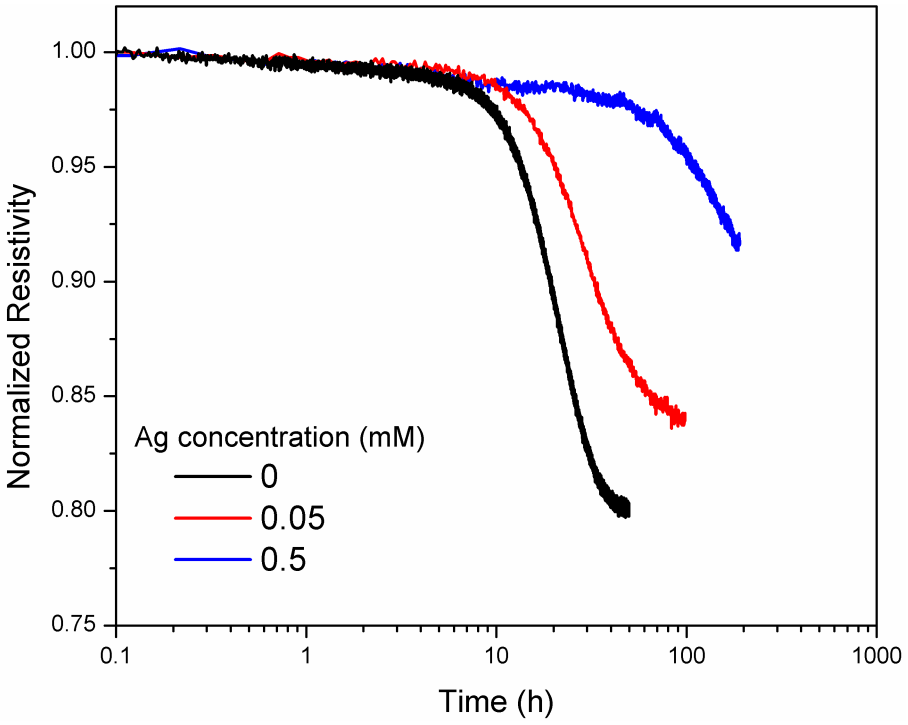

Figure 7.8: Effect of adding silver to the standard electrolyte on the normalized resistivity profiles during self-annealing of 1 μm-thick films that were deposited at 20 mA/cm^2.

even if the electrolyte contains the necessary organic additives, no recrystallization occurs.

When silver is added to the standard electrolyte (i.e. chloride is present), the silver chloride precipitates immediately as indicated by the change in the solution color. However, the deposited film was still shiny and the resistivity measurement shows that self-annealing can still occur as shown in Fig. 7.8. However, the rate of self-annealing seems to be slower for the films electrodeposited with silver present in the electrolyte. Here, it appears that not all silver reacts with chloride and some small amount of silver is still

available to co-deposit with copper (see the analysis in Appendix A). As the concentration of silver is increased in the electrolyte, slower recrystallization is observed. For the case of 0.05 mM of silver, 100 hours were not enough to achieve complete self-annealing compared with about 40 hours for the case when no silver was added. When the silver content was increased to 0.5 mM, less than a 10% resistivity drop was detected even after about 200 hours following the deposition (i.e. recrystallization was not complete even after one week following the deposition). The effect of silver in delaying the onset of recrystallization is less pronounced when the current density is increased to 40 mA/cm^2 as shown in Fig. 7.9. Here, longer incubation period was observed as the silver content is increased, but all the films completely recrystallized in 40 hours or less. For the highest silver concentration studied here (e.g. 0.5 mM), the recrystallization time is 4 times longer than in the case when no silver is present. For the case of 20 mA/cm^2 deposition current density, the film deposited with 0.5 mM of silver underwent very slow self annealing (i.e. recrystallization time much longer than 200 hours). From these results, it seems that the driving pressure for recrystallization for the case of films deposited at 40 mA/cm^2 is significantly enough to overcome the dragging effect of silver. Another possible explanation is that the amount of silver that co-deposits with copper depends on the deposition current density. Similar results were observed when the films were continuously annealed from room temperature to 100 °C as shown in Fig. 7.10. For the highest silver content (0.1 mM), the initial resistivity was 2.43 $\mu\Omega$.cm compared with 2.09 and 2.03 $\mu\Omega$.cm for the film deposited with electrolytes containing 0.01 and 0 mM of silver, respectively. Here, it was observed that the recrystal-

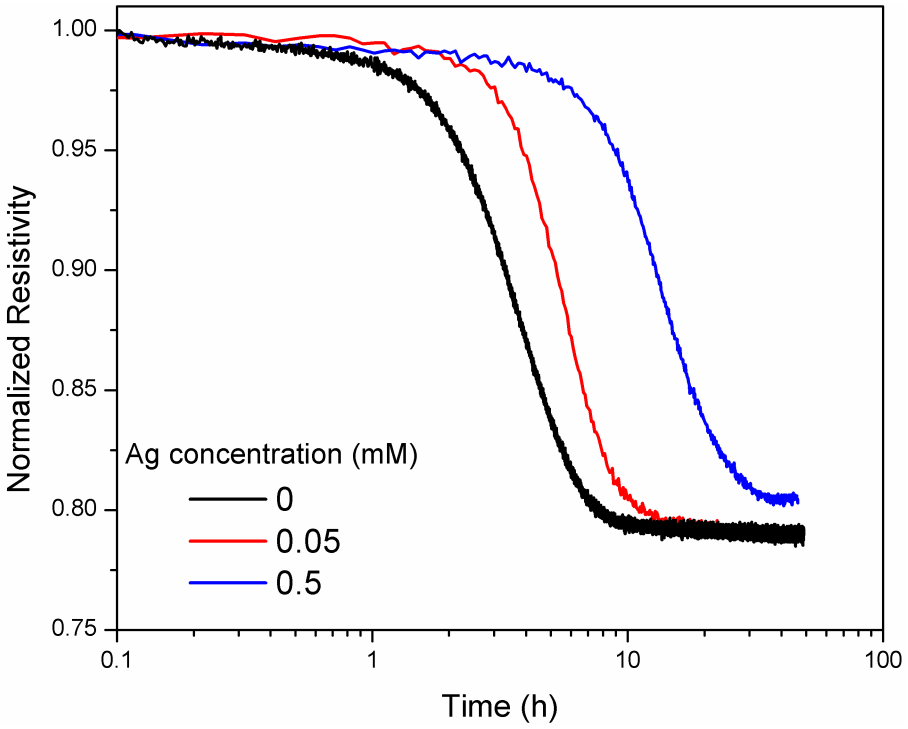

Figure 7.9: Effect of adding silver to the standard electrolyte on the normalized resistivity profiles during self-annealing of 1 μm-thick films that were deposited at 40 mA/cm^2.

lization temperature increases as the silver concentration increases. While the recrystallization temperature is less than 70 °C for the film produced without silver present in the electrolyte, annealing to temperatures higher than 80 °C is required to obtain a recrystallized film in the presence of silver. This implies that high annealing temperature is required to obtain fully recrystallized Cu-Ag film.

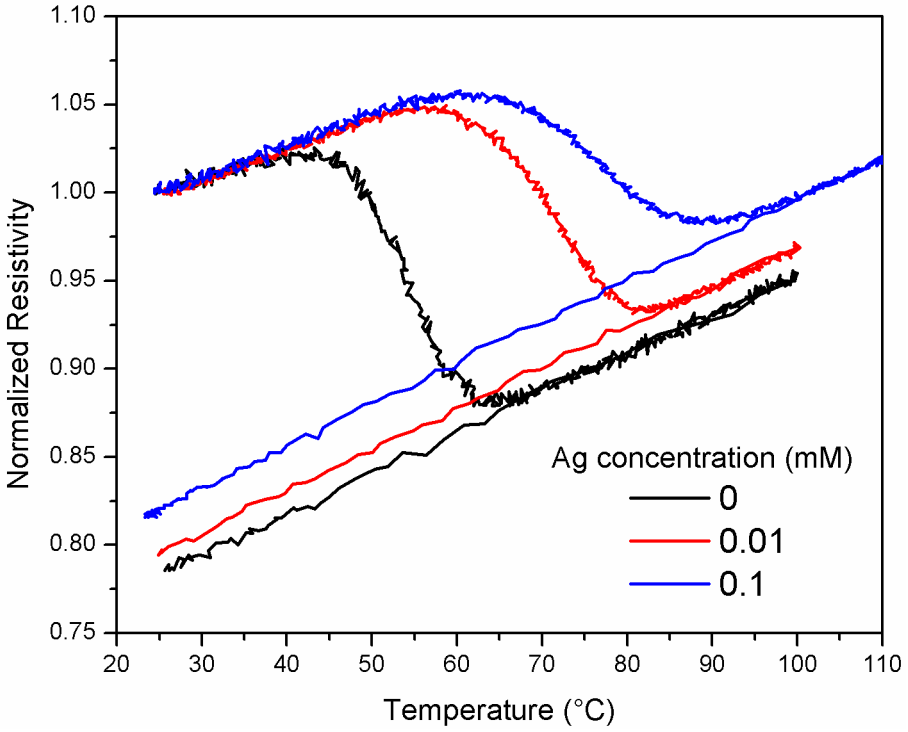

Figure 7.10: Effect of adding silver to the standard electrolyte on the normalized resistivity profiles of 1 μm-thick films that were deposited at 20 mA/cm^2. The films were continuously annealed from room temperature to until a complete recrystallization is obtained (heating rate 1 °C/min) and then air-cooled to the room temperature (10 °C/min) .

7.5 Summary

In this chapter, a deposition strategy was proposed to accelerate recrystallization in copper interconnects. The deposition strategy compensates for the slow recrystallization rate that is normally associated with deposition at low current density. In this method, a capping layer deposited at high current density on the top of the overburden layer. The resistivity and EBSD results showed that recrystallization initiates in the layer deposited at high current density and proceeds to consume the layer deposited at low current density. It was shown that as the thickness of this layer increases, recrystallization is achieved faster. This is significant for the processing of copper interconnects where the temperature (or the holding time) that is required to obtain fully recrystallized microstructure can be significantly reduced. In addition, the effect of adding silver to the deposition bath on the recrystallization rate was studied. When silver is present in the electrolyte not containing chloride, no recrystallization was detected even when annealed at 100 °C for 5 hours. On the other hand, when silver is added to the standard electrolyte (i.e. with chloride present), self-annealing occurs even with the presence of the silver chloride. In this case, the rate of the self-annealing is a function of the deposition current density and the concentration of silver added. The results in this chapter confirm that films produced by Cu-Ag co-deposition require higher holding temperature or longer holding time to obtain a fully recrystallized microstructure.

Chapter 8

Phase-Field Modelling of Recrystallization in Electrodeposited Copper Thin Films

8.1 Introduction

Modelling of the microstructure evolution in copper interconnects is of a great importance to determine the optimum process parameters (e.g. deposition current density, film thickness and temperature). In the literature, there exist models to simulate self-annealing and replicate the fraction recrystallized profiles obtained from resistivity measurement using phenomenological approaches like JMAK model. However, JMAK is not helpful to reveal the details of the microstructure. In this chapter, self-annealing in electrodeposited Cu thin films is simulated using phase-field modelling which is an emerging approach to simulate microstructure evolution processes that include grain growth and recrystallization. Here, a brief introduction of the phase-field theory is provided followed by the simulation methodology that

was employed to model self-annealing. The results of the phase field simulations for films deposited using different deposition current densities are presented and discussed.

8.2 Phase-Field Modelling

Phase field model (PFM) is widely used to simulate microstructure evolution processes that include grain growth, recrystallization and solidification [147–152]. The method was extended to simulate pinning due to finely dispersed second phase particles [153,154] and solute drag [155]. In PFM, the interface between grains is not sharp but considered to be continuously varying with distance and time (i.e. diffuse interface with a finite thickness as shown in Fig. 8.1). The total free energy of a polycrystalline microstructure is composed of a term related to the bulk energy and a second term related to the interface [156,157]. In the phase field approach, the total free energy can be described by a set of field variables ϕ_1, ϕ_2....ϕ_Q (often referred to as order parameters). Here, each crystallographic orientation is represented by an order parameter. The value of the order parameter, ϕ_i, inside the grain i is 1 while the order parameter at the interface is a continuous function with values between 0 and 1 [158]. There are different phase-field models available in the literature (e.g the Fan and Chen model [156] and the multi-phase field model that was proposed by Steinbach et al. [148]). In the multi-phase field model, the rate of the change of the order parameter is described by

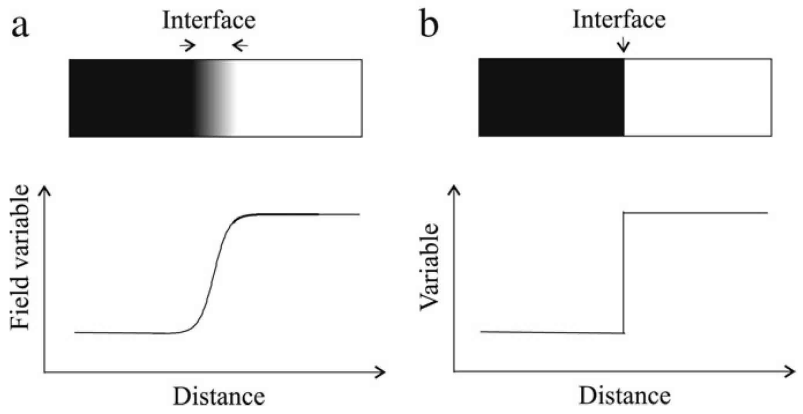

Figure 8.1: (a) A schematic of a diffuse interface where the grain properties change continuously through the interface (b) sharp interface where the properties change discontinuously at the interface. [157]

$$\frac{d\phi_i}{dt} = \sum_{i \neq j} M_{ij} \left[\sigma^*_{ij} \left\{ \phi_j \nabla^2 \phi_i - \phi_i \nabla^2 \phi_j + \frac{\pi^2}{2\eta_{ij}^2} (\phi_i - \phi_j) \right\} + \frac{\pi}{\eta_{ij}} \sqrt{\phi_i \phi_j} \Delta P_{ij} \right] \tag{8.1}$$

Here, M_{ij}, σ^*_{ij} and η_{ij} are the interface mobility, interface energy, and interface thickness, respectively [159]. The term ΔP_{ij} accounts for the driving pressure for microstructure evolution. The evolution of the of the order parameter is related to the minimization of the total free energy in the system. The set of PFM differential equations (shown in Eq. 8.1) can be solved numerically and the evolution of the microstructure with time can be visualized. The physical parameters like the interface mobility is hard to measure experimentally. Thus, to simulate the microstructure evolution in real systems using PFM, input parameters like the interface mobility and nucleation conditions are considered as adjustable parameters. In addition, PFM sim-

ulations are computationally expensive. To reduce the simulation time, the thickness of the interface in PFM simulations is normally considered much larger than the actual thickness [159].

In addition to its application in grain growth and particle pinning, phase-field models were developed to simulate recrystallization. The stored energy driven interface migration at a recrystallization front was simulated by Suwa et al. [160]. Similarly, Takakai et al. [152] developed a phase field model to describe static recrystallization using crystal-plasticity theory. However, the application of phase-field model to describe the microstructure evolution in thin films and interconnect features has not yet been reported. Thus, the present work provides a phase-field simulation of recrystallization in electrodeposited copper thin films.

8.3 Simulation Methodology

The microstructure evolution during recrystallization was simulated using MICRESS® (Microstructure Evolution Simulation Software) [161]. MICRESS is a commercial code that allows to simulate the microstructure evolution in time and space during solidification, grain growth and recrystallization. The software is based on the multi-phase field model that was proposed by Steinbach et al. [148] (i.e. Eq. 8.1). To model self-annealing in electrodeposited Cu thin films, recrystallization in a single phase was simulated assuming two dimensional and three dimensional domains. Here, a single grain was used to represent the nanocrystalline grains in the as-deposited microstructure. This is to simplify the PFM calculations (i.e. the small as-deposited grains are not

resolved). The stored energy is assumed to be homogenous throughout the as-deposited microstructure. Here, the driving pressure for recrystallization was based on the estimation of the dislocation density from the TEM observations (i.e. $\Delta P \approx$ 3-300 J/cm^3 for films which were deposited at 7.5-40 mA/cm^2 [66]). Nucleation site saturation was assumed and 13 nuclei were randomly positioned in the simulation domain at $t = 0$. The number of nuclei that was selected here corresponds to the number of grains that were observed from the EBSD map with grain size greater than 0.4 μm (See Fig. 5.19). The grain boundary energy was assumed to be constant (0.625 J/m^2 [88]). The interface mobility was considered as a fit parameter to replicate the rate of self-annealing that was obtained using resistivity data. The grains in the microstructure were assumed to be isotropic (i.e. no dependence on grain orientation was considered).

In the 2D simulations, 400×400 grid points were considered. The spacing between the grid points was constant ($\Delta x = 0.025$ μm). The domain size was the same as the scanned area in the EBSD maps. The initial radius for all of these nuclei was 0.1 μm and the interface thickness was considered to be $4\Delta x$. To allow for these grains to grow, their stored energy was considered to be zero (i.e. no dislocations present in these grains). Periodic boundary conditions were considered for the 2D simulation. The time step for the simulations was automatically determined by MICRESS. The total simulation time was chosen to be greater than 10 hours to replicate the typical time period that is required to complete self-annealing in 1 μm-thick films. In the 3D simulations, 400×400×40 grid points were considered. Insulated boundary condition was considered at the top and bottom of the film and periodic

boundaries on the other sides. After the simulation is complete, the fraction recrystallized was obtained from MICRESS.

8.4 Sensitivity Analysis

To check the accuracy of MICRESS PFM simulations as a function of the input parameters including interface thickness and step size, a moving boundary due to recrystallization was simulated. Here a 2D domain with a stored energy of 300 J/cm^3 was considered as shown in Fig. 8.2. The stored energy of 300 J/cm^3 corresponds to a scenario of 1 μm-thick film deposited at 40 mA/cm^2 [66]. At $t = 0$, a grain (0.5 μm-wide) was inserted in the calculation domain (left corner of Fig. 8.2-a). To simulate recrystallization, the stored energy inside this grain was considered to be zero. The mobility of the interface was selected to be $7.1\times\ 10^{-11}$ cm^4/Js. Due to the difference between the stored energies across both sides of the boundary, the recrystallized grain size increases with time (See 8.2-b). Figure 8.3 shows the fraction recrystallized as a function of time and interface thickness assuming a fixed step size and interface mobility. The recrystallization for interface thickness of $4\Delta x$ was faster than when the interface thickness was $3\Delta x$. No significant change in the fraction recrystallized was observed when the interface thickness was increased to 5, 6, 7 and $8\Delta x$. However, there is still a significant difference between the simulated fraction recrystallized and the analytical fraction recrystallized that is expected from a sharp interface model (i.e. $v = M\Delta P$). Figure 8.4 shows the effect of the step size on the fraction recrystallized assuming a fixed interface thickness (here, $4\Delta x$). As the Δx decreases, the

fraction recrystallized profile approaches the analytical solution. For small step sizes as of 0.0025 μm, the time required to complete the PFM simulation is very long. This is because MICRESS needs to solve the differential phase-field equations for each grid point in the domain. To correct for the dependance of the PFM simulations on the choice of the step size and interface thickness, the mobility of the interface can be increased to compensate for the difference between the PFM simulation and the analytical solution. Here, a fixed step size and interface thickness were considered (0.025 μm and $4\Delta x$, respectively). Figure 8.5 shows the fraction recrystallized as a function of the interface mobility. The recrystallization is faster as the mobility is increased. Taking $M = 7.1 \times 10^{-11}$ cm^4/Js as a reference, the mobility needs to be increased to 11.3×10^{-11} cm^4/Js to replicate the analytical solution. For this case, the correction factor, C_f, is 1.59. For the case of grain growth, a difference between the PFM simulations and the analytical solution was also observed (see Appendix B). The driving pressure for grain shrinking is much smaller than the driving pressure for recrystallization that was considered here (i.e. 300 J/cm^3). Thus, it is considered to be reasonable to use the mobility correction factor of 1.59 in the PFM simulations of self-annealing.

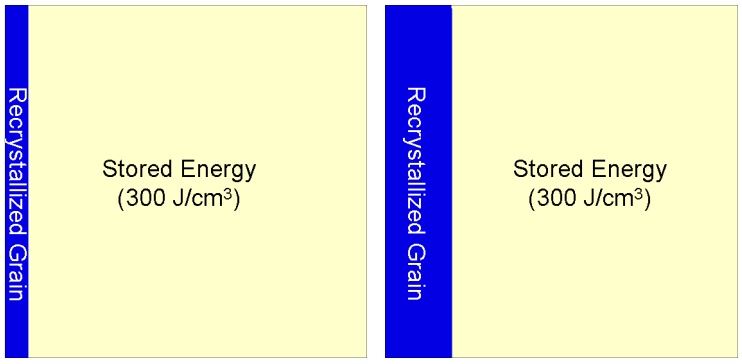

Figure 8.2: PFM simulation of the recrystallization process (here, the step size (Δx) is 0.025 μm, interface thickness is $4\Delta x$ and the domain size is 400×400). The mobility of the interface was 7.1×10^{-11} cm^4/Js. (a) $t = 0$ seconds and (b) 10^4 seconds.

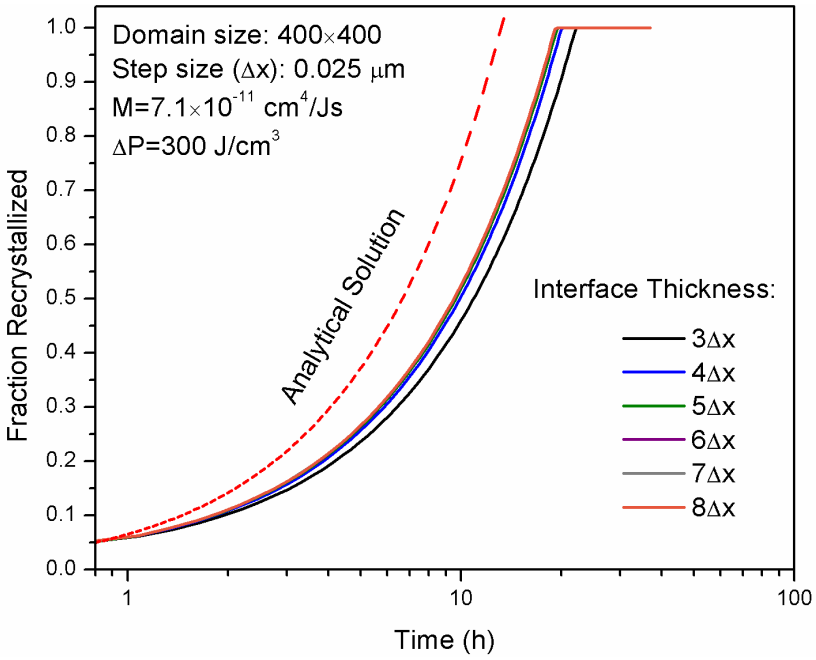

Figure 8.3: The effect of the interface thickness on the fraction recrystallized profile that is obtained from PFM simulations. The Analytical solution is based on ($v = M\Delta P$) where $M = 7.1 \times 10^{-11}$cm^4/Js. The time is adjusted to account for the incubation period in a film deposited at 40 mA/cm^2.

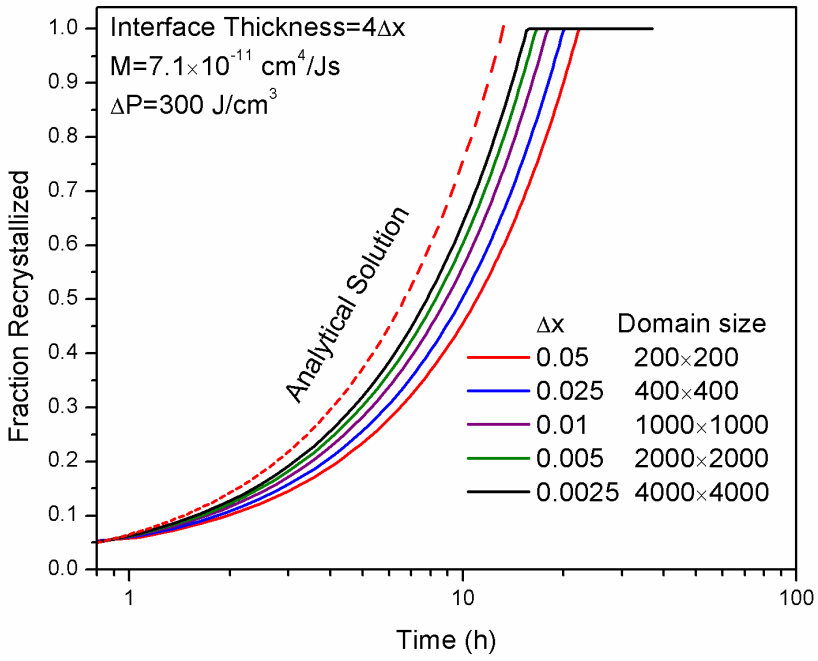

Figure 8.4: The effect of the step size (Δx) in the PFM simulation on the fraction recrystallized profile. The Analytical solution is based on ($v = M\Delta P$) where $M = 7.1 \times 10^{-11}$ cm^4/Js.

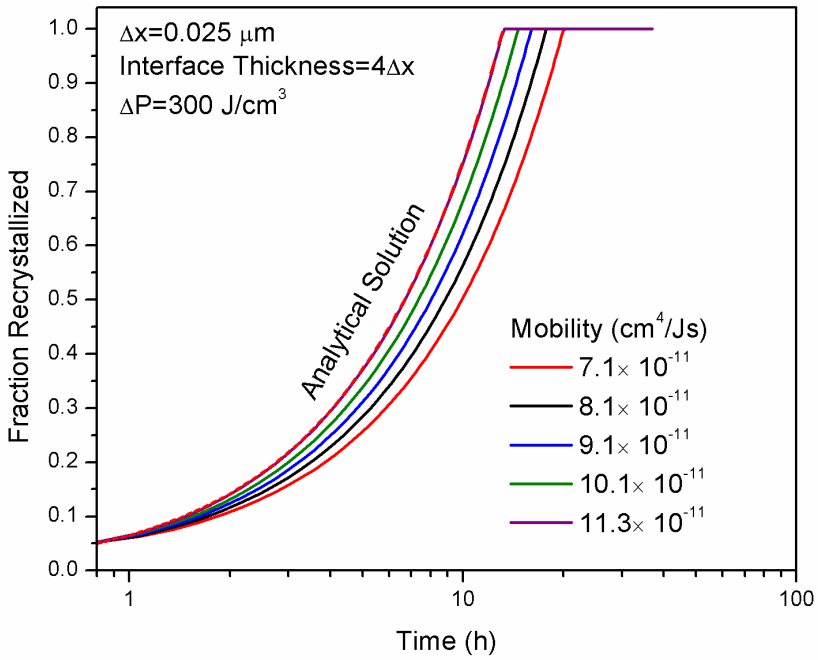

Figure 8.5: The fraction recrystallized from PFM simulations as a function of the interface mobility. The Analytical solution is based on ($v = M\Delta P$) where $M = 7.1 \times 10^{-11}$ cm^4/Js.

8.5 Simulation Results

8.5.1 2D Simulation

The phase-field simulations for the film deposited at 40 mA/cm^2 are shown in Fig. 8.6. In these simulations, the stored energy in the as-deposited microstructure was 300 J/cm^3. After 0.5 hour, all the nuclei grow at the expense of the nonrecrystallized grains as can be seen in Fig. 8.6-b. The recrystallized area increases with time and recrystallization proceeds towards completion. After 3 hours, the recrystallized grains start to impinge on each other and a fully recrystallized microstructure was achieved in about 7 hours (see Fig. 8.6-f). Figure 8.7 shows a comparison between the fraction recrystallized obtained from resistivity measurements and that obtained from PFM simulations. The PFM simulations were repeated 3 times (different location of the nuclei in each case). For the mobility value used here (6.1 $\times 10^{-11}$ cm^4/Js), the fraction recrystallized obtained from the PFM is in a reasonable agreement with the fraction recrystallized obtained from resistivity.

Figure 8.8 shows the PFM simulations for the case of the film deposited at 30 mA/cm^2. Here, the mobility was considered constant (6.1 $\times 10^{-11}$ cm^4/Js) while the stored energy was adjusted to replicate the fraction recrystallized obtained from resistivity. For this case, it was found that a stored energy value of 130 J/cm^3 produces a fully recrystallized microstructure in about 15 hours. Comparing the microstructure evolution that corresponds to this deposition scenario with the case described in Fig. 8.6 and taking $t = 3$ hours as an example, a slower recrystallization is observed for the 30 mA/cm^2 scenario. Here, the stored energy difference between the 30 mA/cm^2 and

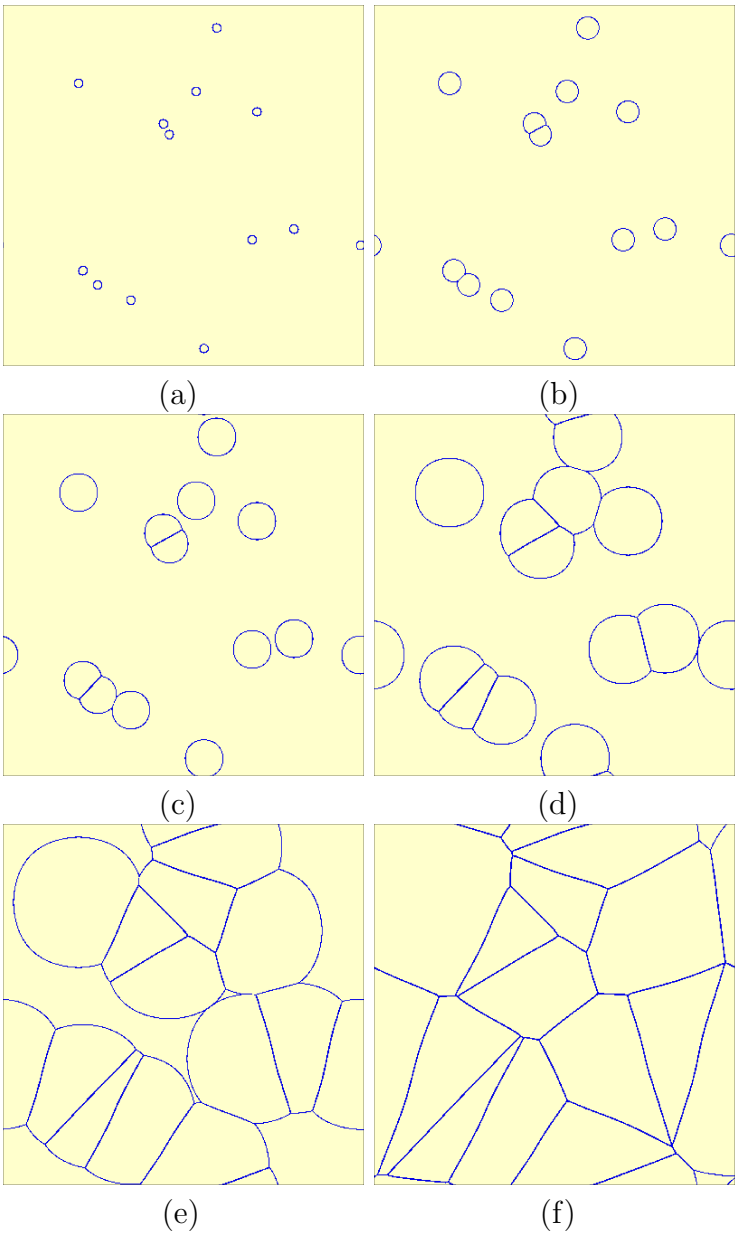

Figure 8.6: Simulation of the microstructure evolution for the case of the film deposited at 40 mA/cm^2 (a) 0 hour (b) 0.5 hour (c) 1 hours (d) 2 hours (e) 3 hours and (f) 7 hours.

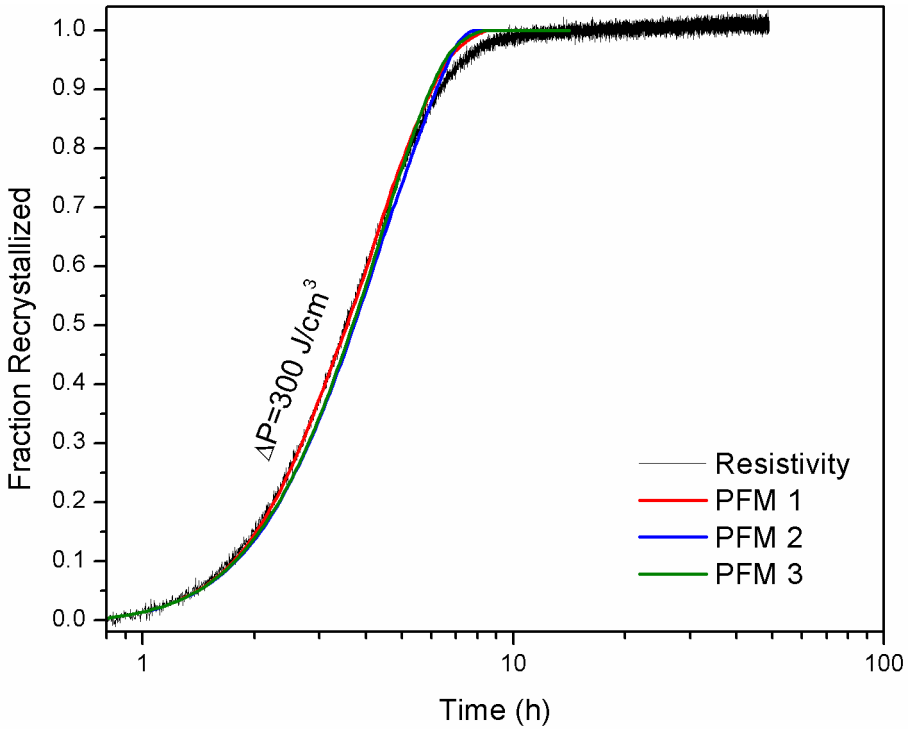

Figure 8.7: The fraction recrystallized obtained from resistivity and PFM simulation for the 1 μm-thick film that was deposited at 40 mA/cm^2. The fraction recrystallized curves were adjusted to account for the incubation period (t_{inc} =0.8 hour). The PFM simulations were repeated 3 times (nuclei locations at $t = 0$ are different in each case).

40 mA/cm^2 cases accounts for the different recrystallization rates. For the deposition current density of 20 and 10 mA/cm^2, the stored energy values that replicate the fraction recrystallized from resistivity were 50 J/cm^3 and 12 J/cm^3, respectively. The PFM simulations corresponding to these stored energy values are shown in Fig. 8.9. The film deposited at 20 mA/cm^2 shows faster recrystallization than the film deposited at 10 mA/cm^2. For the 20 mA/cm^2 deposition scenario, the PFM simulation shows a fully recrystallized microstructure in about 30 hours. On the other hand, around 100 hours are not enough for the film produced at 10 mA/cm^2 deposition current density to complete self-annealing. Figure 8.10 shows a comparison between the fraction recrystallized profiles obtained from resistivity measurements and that obtained from PFM simulations. Here, the mobility and the stored energy that are used in the PFM simulations are appropriate to replicate the fraction recrystallized profiles obtained from resistivity.

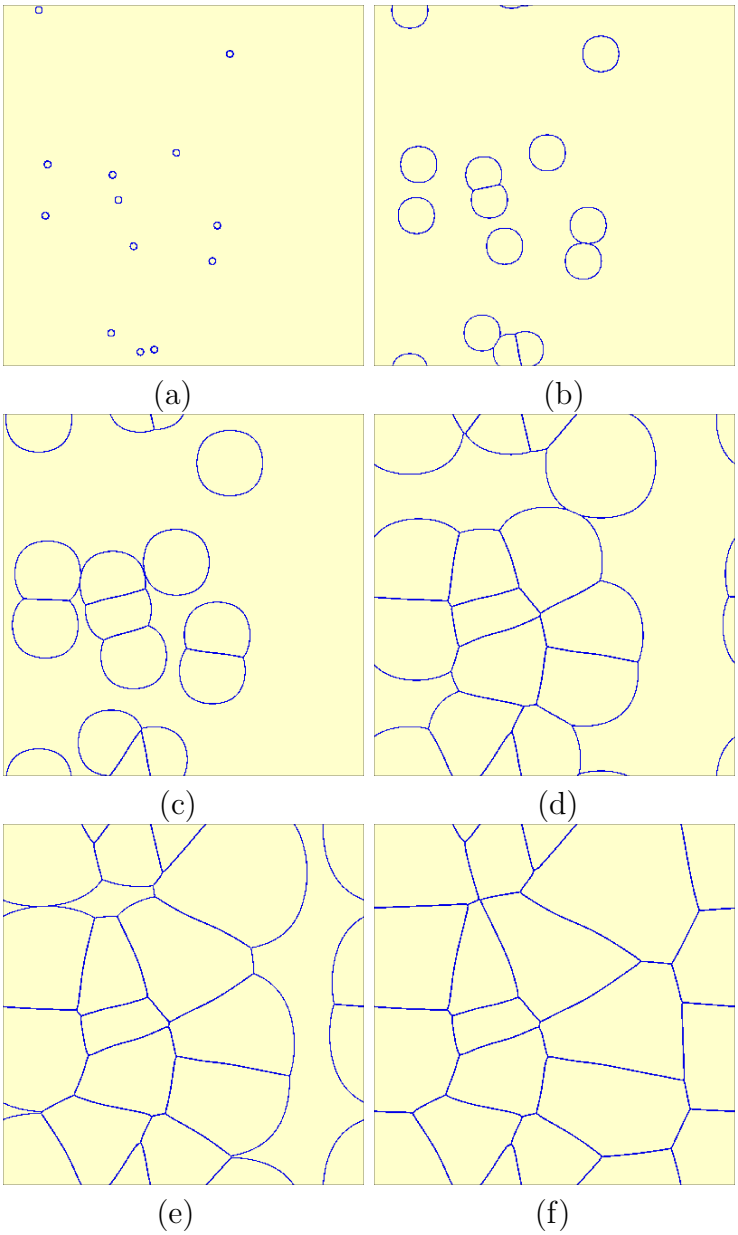

Figure 8.8: Simulation of the microstructure evolution for the case of the film deposited at 30 mA/cm^2 (a) 0 hour (b) 2 hours (c) 3 hours (d) 7 hours (e) 10 hours and (f) 15 hours.

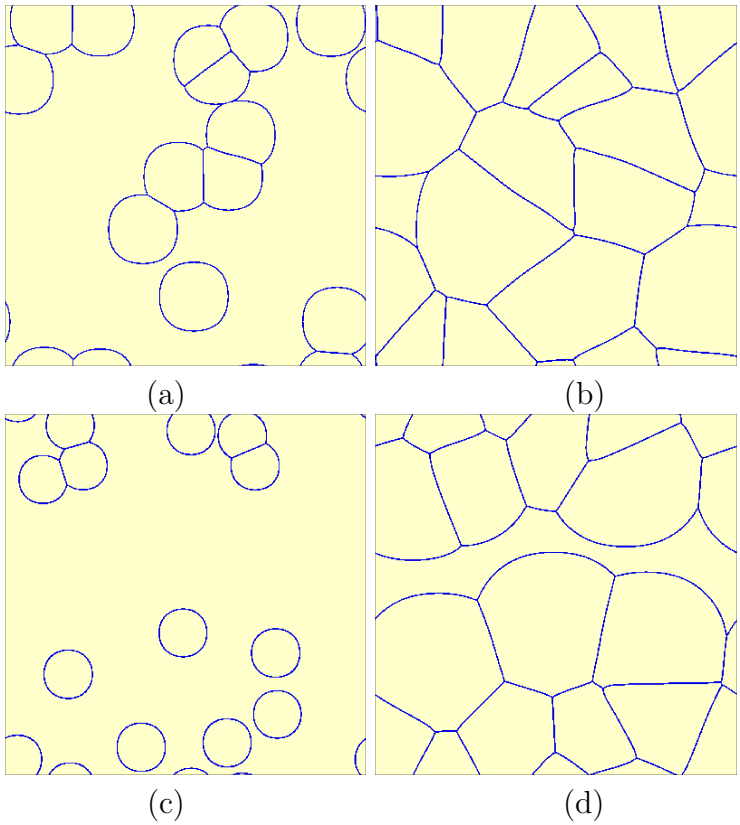

Figure 8.9: Simulation of microstructure evolution for the case of the film deposited at 20 mA/cm^2 (a) 10 hours and (b) 30 hours and at 10 mA/cm^2 (c) 10 hours (d) 100 hours.

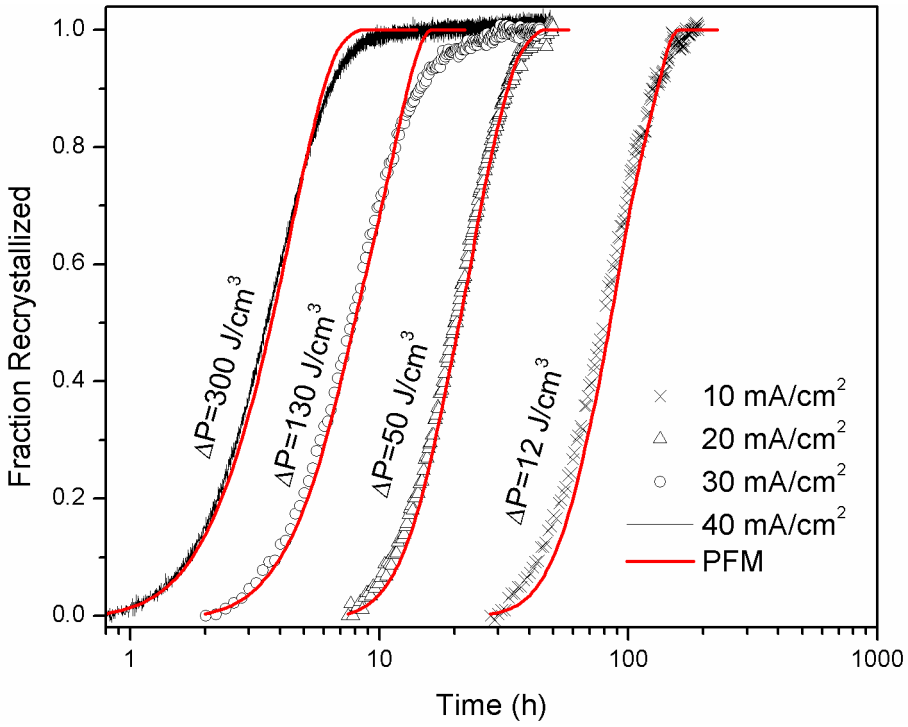

Figure 8.10: The fraction recrystallized obtained from resistivity and that obtained from 2D PFM simulation for films deposited at 10, 20 and 30 and 40 mA/cm^2. The fraction recrystallized curves were adjusted to account for the incubation period.

8.5.2 3D Simulation

To simulate the fact that recrystallization initiates in the bulk of the film near the substrate, the 13 nuclei were randomly distributed in the lower half of the film. The stored energy and mobility were the same as those used in the 2D PFM simulations (i.e. 6.1×10^{-11} cm^4/Js and 300 J/cm^3, respectively). Figure 8.11 shows the fraction recrystallized obtained from the PFM simulation of 1 μm-thick film deposited at 40 mA/cm^2 and compared with the fraction recrystallized from resistivity and EBSD profile. There is a reasonable agreement between fraction recrystallized obtained from resistivity and the fraction recrystallized that was obtained from the PFM simulations. Here, the PFM simulations show that there is a time lag between the fraction recrystallized obtained at the surface and that obtained from the bulk of the film. For this case, the fraction recrystallized that was obtained from the top surface approaches the fraction recrystallized profile obtained from the volume of the film after about 4 hours (i.e. $f > 0.6$). The time lag between the fraction recrystallized profile obtained from the top surface and that obtained from the bulk is consistent with the experimental observations from resistivity and in-situ EBSD. However, the PFM simulation does not exactly replicate the fraction recrystallized that was obtained from resistivity as in the case of the 2D simulations discussed above.

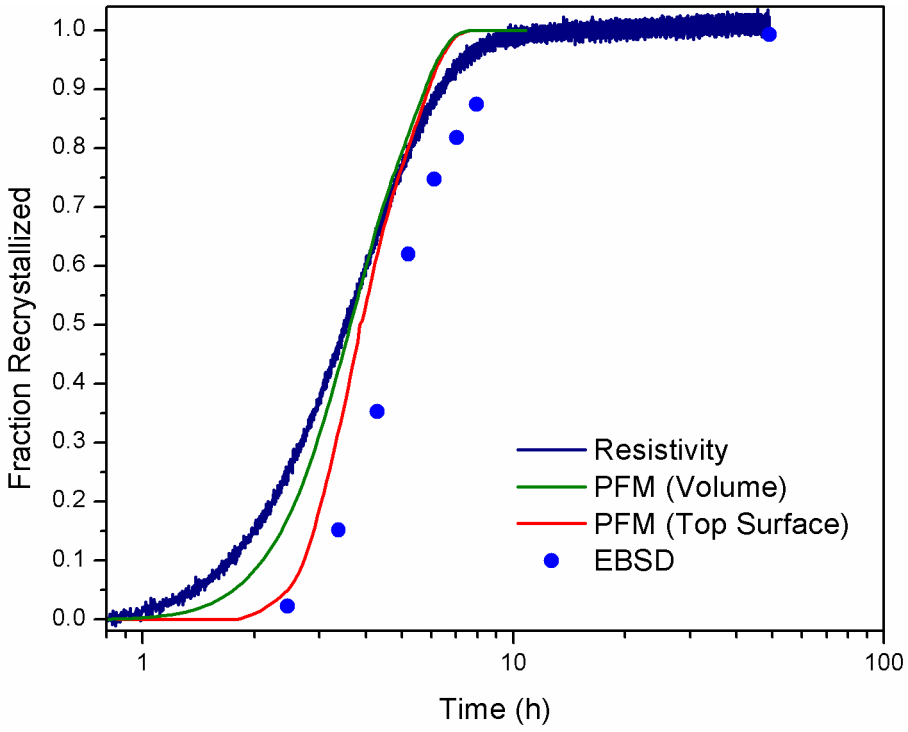

Figure 8.11: The fraction recrystallized obtained from resistivity, EBSD and that obtained from 3D PFM simulation for the film deposited at 40 mA/cm^2. From PFM simulation, two fraction recrystallized profiles were obtained: One from the bulk of the film and the other from the top surface.

8.5.3 Recrystallization in Dual Damascene Interconnects

Using the stored energies and mobility values that were obtained from the PFM simulations, one can simulate the progress of recrystallization in copper interconnects. Here, recrystallization initiates in the overburden layer above the trench corners as proposed by Lingk and Gross [69]. Recrystallization then proceeds to consume the overburden layer and the Cu trenches. To simulate this scenario using PFM, two separate phases were considered in the initial structure: copper phase and Low-K dielectric phase. Since the microstructure evolution occurs only in the copper phase, no phase interaction was considered between the two phases. Here, through-thickness PFM simulations were performed and 3 nuclei were placed in the overburden layer above the trench corners as shown in Fig. 8.12-a. After 12.5 hours at room temperature, the recrystallized grain grew to consume the overburden layer and Cu trench. After 37.5 hours, the grains impinge on each other and recrystallization proceeds towards completion. Complete recrystallization of the overburden and the Cu trenches was obtained after 150 hours. Based on this model, PFM can be useful to simulate the progress of recrystallization in copper interconnects as a function of geometry. For example, Fig. 8.13 shows the fraction recrystallized obtained from PFM simulations as a function of the trench height (i.e. different aspect ratio). Here, as the height of the interconnect trench is increased, longer times are required to obtain a fully recrystallized microstructure. About 200 hours are required for the trenches with a height of 3 μm to complete self-annealing compared with less than 100 hours for the case when the trench height is 0.5 or 1 μm.

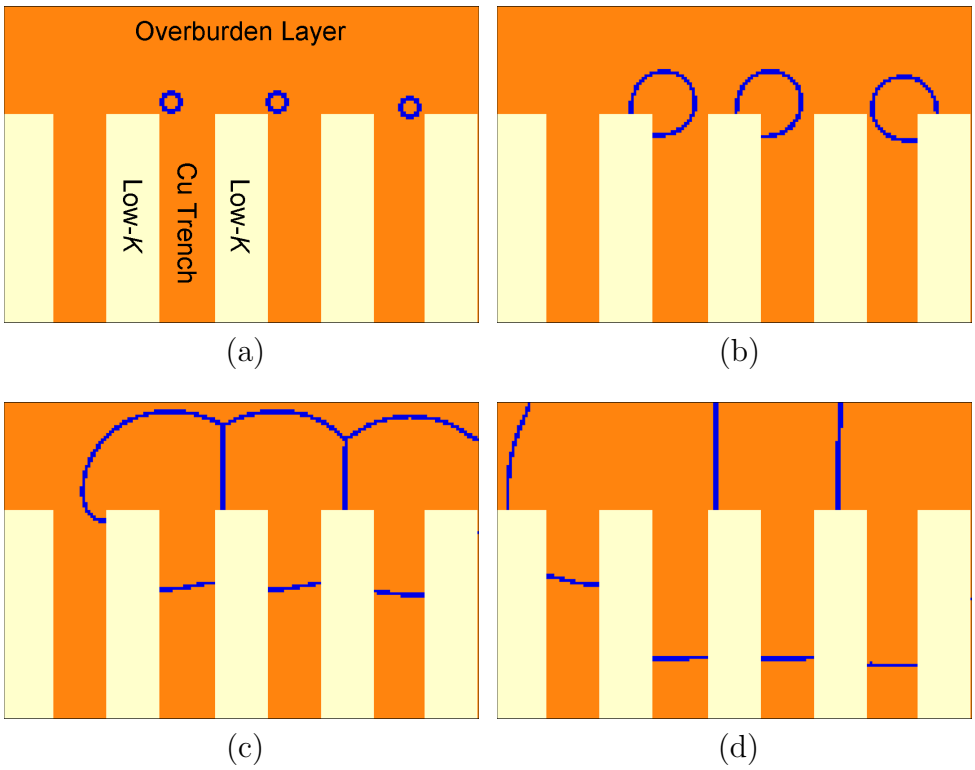

Figure 8.12: PFM simulation for recrystallization in copper interconnects as a function of time. (a) $t = 0$ h (b) $t = 12.5$ h (c) $t = 37.5$ h and (d) $t = 125$ h. The interconnect trench width and height were 0.5 μm and 2 μm, respectively. The height of the overburden layer was 1 μm. The deposition current density was assumed to be 10 mA/cm^2 and the Cu interface mobility was 6.1×10^{-11} cm^4/Js.

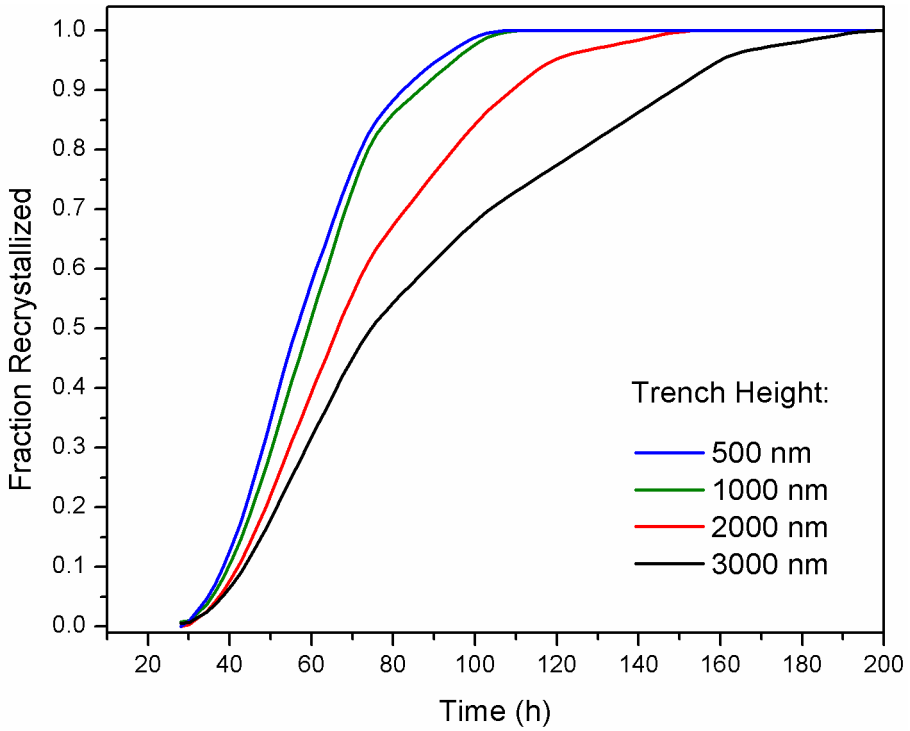

Figure 8.13: The fraction recrystallized as a function of PFM simulation time and the Cu trench height. The thickness of the overburden layer and the width of the trench were constants (1 and 0.5 μm, respectively). The fraction recrystallized profile was adjusted to account for the incubation period at 10 mA/cm^2 deposition current density.

8.6 Discussion

The simulation results presented in this work show that PFM can be used to simulate the phenomenon of self-annealing in copper thin films. Here, the dependence of the recrystallization rate on the deposition current density can be described by varying the stored energy in the initial microstructure. The interface mobility at room temperature is hard to measure and was considered here as a fit parameter. The mobility that was obtained from MICRESS, $M_{MICRESS}$, to replicate the fraction recrystallized profiles obtained from resistivity was 6.1 $\times 10^{-11}$ cm^4/Js. This mobility value must be corrected to account for the numerical artifact discussed in section 8.4. The actual mobility that replicates the resistivity data is

$$M = \frac{M_{MICRESS}}{C_f} \tag{8.2}$$

Thus, the actual mobility that replicates the resistivity profile is 3.8×10^{-11} cm^4/Js.

Vandermeer et al. [80] measured the stored energy in cold worked copper using calorimetry analysis. The researchers then measured the average interface velocity during recrystallization at 121 °C and found that the relationship between the two quantities obeys Eq. 2.9. The estimated mobility at this temperature was 6.31 $\times 10^{-8}$ cm^4/Js. As explained by Detavernier et al. [88], the interface mobility at a specific temperature, $M(T)$, can be obtained by extrapolation using:

$$M(T) = M(T_0) \exp\left(-\frac{Q}{k_B}\left(\frac{1}{T} - \frac{1}{T_0}\right)\right).\frac{T_0}{T} \tag{8.3}$$

where $M(T_0)$ is the mobility at a known temperature T_0. To obtain an estimate of the mobility of the boundary at room temperature (20 °C), the mobility at 121 °C can be used in Eq. 8.3. For the activation energy, 0.89-0.93 eV that were obtained from the isothermal and continuous resistivity measurements can be used. This results in a room temperature mobility of 0.67 $\times 10^{-11}$ to 1.01 $\times 10^{-11}$ cm^4/Js. From the PFM simulation presented here, the value of the boundary mobility that replicated the resistivity data (3.8 $\times 10^{-11}$ cm^4/Js) seems to be comparable with the mobility value obtained by extrapolation. This suggests that the mobility value used in the PFM simulation above is reasonable. It should be acknowledged that the mobility value that was obtained here using Eq. 8.3 is based on the data for cold-worked copper and the stored energy value (300 J/cm^3) that was reported by Lee et al. [66] is higher than what is expected for cold-worked copper (≈2-20 J/cm^3 [78]).

Stangl and Militzer [65] proposed that the dislocation density (and hence the stored energy) is directly proportional to the deposition current density (i.e. $\Delta P = Bj^*$, where j^* is the deposition current density and B is the proportionality factor). Figure 8.14 compares the stored energies values as a function of the deposition current density that were proposed by Lee et al. [66] and Stangl and Militzer [65] with the stored energies that were obtained from the PFM simulations in this work . Here, there is an agreement at low deposition current density between the PFM simulations and the data of Lee et al. [66]. It is still reasonable to assume that the stored energy changes linearly with the deposition current density between 20 to 40 mA/cm^2.

The PFM can be used to simulate recrystallization in copper intercon-

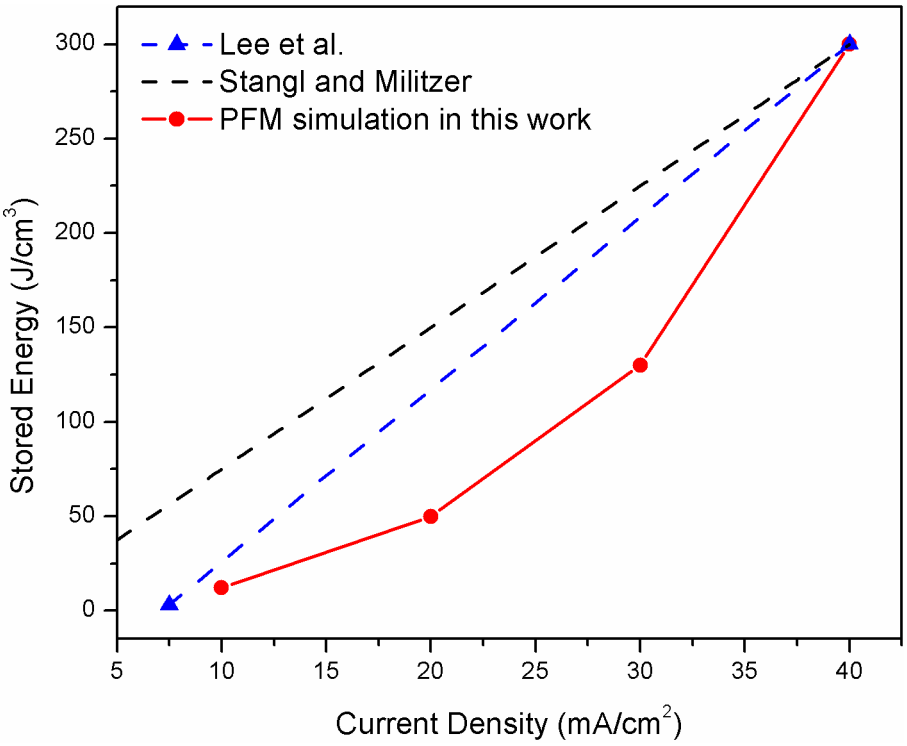

Figure 8.14: The relation between the stored energy and current density as obtained from the PFM simulations. The proposed relationships between the stored energy and current density that are available in the literature are included for comparison.

nects as shown in Fig. 8.12. The recrystallized grains appear to extend through the entire interconnect trench. This was observed experimentally by EBSD as shown in Fig. 8.15. Here, a single grain with its twins appears in the trench of the self-annealed and in the annealed microstructure. The PFM can be useful where a complete process map of the recrystallization rate as a function of the interconnect geometry (e.g. the width of interconnect trench, the height of the overburden layer and thickness of the dielectric) can be obtained. Wu et al. [162] showed that the extent to which recrystallized grains

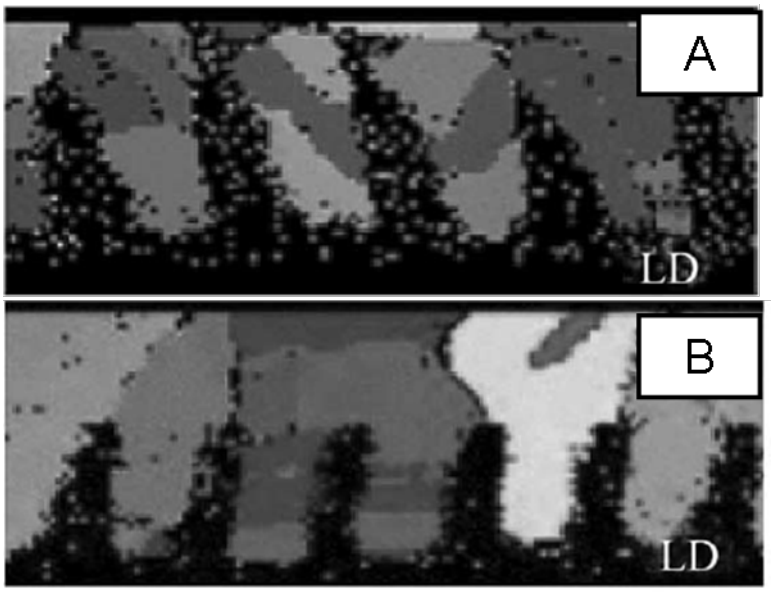

Figure 8.15: EBSD maps showing the cross section of Cu trenches after recrystallization (A) Self-annealed (30 days) and (B) Annealed at 200 °C for 10 minutes. The width, spacing and the height of the trench line were 0.5 μm, 0.5 μm and 0.7 μm. The height of the overburden layer was 0.7 μm. [163]

in the overburden layer affect recrystallization in copper trenches depends significantly on the width of the interconnect line. The researchers found that higher annealing temperature is required for the case of narrower lines. A more in-depth investigation is needed to measure the driving pressure for recrystallization in narrow trenches. The microstructure in the PFM simulations presented above is not identical to the one observed by EBSD. The PFM simulation does not include twins that are observed in the recrystallized microstructure. Further, the simulations did not take anisotropy into consideration. To replicate the details of the microstructure (like twinning and the development of a preferred texture), more advanced PFM is needed.

8.7 Summary

In this chapter, the microstructure evolution in electrodeposited copper thin films during self-annealing was simulated using phase-field. The simulations were obtained using MICRESS commercial code and simplified by assuming nucleation site saturation. Using the stored energies reported in the literature, the mobility of the interface at room temperature was found to be 3.8 $\times 10^{-11}$ cm^4/Js. By varying the stored energies, the effect of the deposition current density on self-annealing rate was simulated. From the stored energies that were found from the PFM, self-annealing in copper interconnects was simulated. In this case, the fact that recrystallization initiates in the overburden layer was modelled by assuming nucleation above the trench corners. The model was extended to assess recrystallization rate as a function of interconnect height. The PFM simulations presented in this chapter did not account for the slow recrystallization that is usually observed in narrow interconnect lines. In addition, the formation of twins and texture development during self-annealing were not simulated. A more advanced phase-field model is needed for this purpose.

Chapter 9

Conclusion and Future Remarks

9.1 Summary of Observations

This thesis presented a systematic study of the effect of deposition conditions on the rate of microstructure evolution during the phenomenon of self-annealing. In-situ EBSD was employed to study the correlation between resistivity and microstructure during self-annealing. From EBSD results, criteria based on grain size, image quality and local orientation spread were developed to assess the self-annealing rate. The correlation between microstructure and resistivity during self-annealing was then investigated. Further, the recrystallization rate during isothermal and continuous annealing treatment was investigated. A phenomenological model based on the JMAK approach was developed to describe the effect of temperature on recrystallization rate. Moreover, recrystallization in films produced by variable current density along with the effect of copper-silver co-deposition on recrystallization rate were studied. A phase-field model using the MICRESS commercial code was applied to replicate the rate of self-annealing that was observed using the resistivity measurements. The major findings of this works are

summarized below.

9.1.1 Self-annealing and Microstructure-Resistivity Correlation

A strong effect of deposition rate and film thickness on self-annealing rate was observed. As the film thickness is increased, self-annealing is accelerated. Similarly, the self-annealing can be accelerated by deposition at high current density. The time required to complete self-annealing is sensitive to the age of the electrolyte. Aged electrolyte results in self-annealing times that can be an order of magnitude longer than when fresh electrolyte is used. Self-annealing can be tracked at the film surface by in-situ EBSD technique during the first 10 hours after deposition. The drop in resistivity during self-annealing is accompanied by significant changes in grain size, image quality and local orientation spread. The microstructure of self-annealed film contains high twins density with average grain size much larger than the film thickness. The best method to asses self-annealing from EBSD maps is by adopting a threshold based on grain size (0.4 μm). Although the resistivity is a volume measurement while EBSD provides the details of the microstructure at surface, there is reasonable correlation between the drop in resistivity and the rate of grain size evolution. Self-annealing appears to initiate near the substrate and then proceeds towards the film surface. The recovery process is detected by resistivity measurements but the details of the microstructure evolution (e.g. grain size and twin density) are obtained from EBSD. Thus, the combination of resistivity and EBSD characterization provides a complete description of self-annealing in copper interconnects.

9.1.2 Recrystallization During Annealing Treatment

The recrystallization in copper interconnects appears to be thermally activated with an activation energy of 0.89-0.93 eV . For 1 μm-thick films, the heating rate and the deposition current density control the recrystallization time and temperature. A unified JMAK model was developed to describe the recrystallization rate obtained from resistivity measurements during annealing. Adopting the principle of additivity, the recrystallization rate during continuous annealing can be described using the isothermal resistivity profiles. Based on this model, a process map was obtained to describe the recrystallization during heating and holding.

9.1.3 Acceleration of Recrystallization

The recrystallization in copper interconnects can be accelerated by depositing a capping layer on top of the overburden layer. The capping layer is deposited at high current density (e.g. 40 mA/cm^2). The resistivity and EBSD results showed that recrystallization initiates in the capping layer and then proceeds to consume the layer deposited at low current density (e.g. 5 mA/cm^2). Since superconformal filling of narrow trenches and vias in Dual Damascene process is obtained using low deposition current density, the proposed capping layer is helpful to promote recrystallization in copper interconnects. Thus, the optimum annealing process temperature could be significantly reduced.

9.1.4 Copper-Silver Alloying

When silver is present in the electrolyte not containing chloride, no recrystallization occurs for 2 μm-thick films even when annealed at 100 °C for 5 hours. This suggests that silver inhibits the recrystallization process in electrodeposited thin films. When silver is added in the presence of chloride ions, silver chloride precipitates immediately but self-annealing was observed. However, adding silver to the electrolyte appears to delay the onset of recrystallization. High annealing temperature is required to obtain fully recrystallized copper-silver alloy films.

9.1.5 Phase-Field Modelling

Phase-field modelling was applied to simulate recrystallization in thin films. Assuming a homogenous distribution of stored energy, the interface mobility was varied to replicate the fraction recrystallized obtained from the resistivity measurements. From the phase-field simulation of 1 μm-thick film deposited at 40 mA/cm^2, the mobility of the interface was estimated to be 3.8×10^{-11} cm^4/Js. Using the stored energies and mobility values that were obtained from phase-field simulations, recrystallization in copper interconnects was simulated. Here, self-annealing was initiated by considering nucleation in the overburden layer above the corners of the trench lines as was proposed in the literature. The phase-field model is helpful to simulate the effect of the interconnect geometry on self-annealing rate (e.g. the height of the interconnect line).

9.2 Future Work

From this work, it appears that there are still areas where more research work is needed to provide a more in-depth understanding and better control of recrystallization in copper interconnects. Some suggestions can be made as follows:

1. Since the processing of copper interconnects requires temperatures as high as 400 °C, a systematic investigation is needed to check if recrystallization in copper interconnects at the optimum temperatures can be described by JMAK and additivity rule.

2. A complete process map to describe the effect of the interconnect geometry (e.g. overburden layer thickness and line width) and the deposition conditions (e.g. deposition current density and electrolyte chemistry) on recrystallization rate is needed. This process map will be of significance to the microelectronic industry.

3. Since novel deposition strategies including pulse-electrodeposition were proposed to synthesize copper micostructures with desired characteristic (e.g. high density of nanotwins), a systematic study is needed to check whether or not self-annealing can still occur in these films. This should include a study to quantify the effect of deposition conditions, film thickness, time on and time off on recrystallization rate. Moreover, a study to show how the high density of nanotwins in the as-deposited microstructure affects the progress of self-annealing is required.

4. Although the capping layer deposited at high current density appears to

accelerate recrystallization in copper thin films, the effectiveness of this method on promoting recrystallization in very narrow interconnects lines has yet to be determined.

5. The copper-silver co-deposition should be optimized to produce microstructures that are resistant to electromigration. Since silver reacts with chloride which is present in the standard electrolyte, material other than chloride is needed so that all silver in the solution is available to deposit with copper.

6. Phase field model is suitable to simulate recrystallization in thin films and in copper interconnects. An ideal phase-field simulations should account for anisotropy and twin formation during recrystallization. A phase field simulation to describe recrystallization rate in narrow interconnects trenches and vias (28 nm technology node and below) with the ability to predict the effect of deposition conditions and temperature will be useful.

Bibliography

[1] M. Bohr, "Interconnects scaling-the real limiter to high performance ULSI," in *Electron Devices Meeting*, pp. 241–244, 1995.

[2] R. C. Liu, C. S. Pai, and E. Martinez, "Interconnect technology trend for microelectronics," *Solid-State Electronics*, vol. 43, pp. 1003–1009, 1999.

[3] J. R. Black, "Electromigration: A brief survey and some recent results," *IEEE Transactions on Electron Devices*, vol. 16, pp. 338–347, 1969.

[4] K. Lee and P. Ho, "Statistical study for electromigration reliability in dual-damascene Cu interconnects," *IEEE Transactions on Device and Materials Reliability*, vol. 4, pp. 237–245, 2004.

[5] E. T. Ogawa, K. D. Lee, V. A. Blaschke, and P. S. Ho, "Electromigration reliability issues in dual-damascene Cu interconnections," *IEEE Transactions on Reliability*, vol. 51, pp. 403–419, 2002.

[6] E. T. Ogawa, A. J. Bierwag, K. D. Lee, H. Matsuhashi, P. R. Justison, A. N. Ramamurthi, P. S. Ho, V. A. Blaschke, D. Griffiths, A. Nelsen, M. Breen, and R. H. Havemann, "Direct observation of a critical length effect in Dual-Damascene Cu," *Applied Physics Letters*, vol. 78, pp. 2652–2654, 2001.

[7] M. A. Meyer, M. Herrmann, E. Langer, and E. Zschech, "In situ SEM observation of electromigration phenomena in fully embedded copper interconnect structures," *Microelectronic Engineering*, vol. 64, pp. 375–382, 2002.

[8] H. Lee and S. D. Lopatin, "The influence of barrier types on the microstructure and electromigration characteristics of electroplated copper," *Thin Solid Films*, vol. 492, pp. 279–284, 2005.

[9] A. V. Vairagar, S. G. Mhaisalkar, and A. Krishnamoorthy, "Electromigration behavior of dual-damascene Cu interconnects-structure, width, and length dependences," *Microelectronics Reliability*, vol. 44, pp. 747–754, 2004.

[10] A. V. Vairagar, S. G. Mhaisalkar, M. A. Meyer, E. Zschech, A. Krishnamoorthy, K. N. Tu, and A. M. Gusak, "Direct evidence of electromigration failure mechanism in Dual-Damascene Cu interconnect tree structures," *Applied Physics Letters*, vol. 87, p. 081909, 2005.

[11] A. V. Vairagar, Z. Gan, W. Shao, S. G. Mhaisalkar, H. Li, K. N. Tu, Z. Chen, E. Zschech, H. J. Engelmann, and S. Zhang, "Improvement of electromigration lifetime of submicrometer Dual-Damascene Cu interconnects through surface engineering," *Journal of The Electrochemical Society*, vol. 153, pp. G840–G845, 2006.

[12] C. L. Gan, C. V. Thompson, K. L. Pey, W. K. Choi, H. L. Tay, B. Yu, and M. K. Radhakrishnan, "Effect of current direction on the lifetime of different levels of Cu Dual-Damascene metallization," *Applied Physics Letters*, vol. 79, pp. 4592–4594, 2001.

[13] L. M. Gignac, C. K. Hui, B. Herbst, and B. C. Baker-O'Neal, "The effect of microstructure on resistivity and reliability in copper interconnects," in *Advanced Metallization Conference 2007 (AMC 2007)*, pp. 641–452, Materials Research Society, 2008.

[14] C. K. Hu, L. Gignac, S. G. Malhotra, R. Rosenberg, and S. Boettcher, "Mechanisms for very long electromigration lifetime in dual-damascene Cu interconnections," *Applied Physics Letters*, vol. 78, pp. 904–906, 2001.

[15] M. Stangl, M. Lipták, J. Acker, V. Hoffmann, S. Baunack, and K. Wetzig, "Influence of incorporated non-metallic impurities on electromigration in copper damascene interconnect lines," *Thin Solid Films*, vol. 517, pp. 2687–2690, 2009.

[16] S. P. Murarka, "Multilevel interconnections for ULSI and GSI era," *Materials Science and Engineering: R: Reports*, vol. 19, pp. 87–151, 1997.

[17] G. Schneider, M. A. Meyer, G. Denbeaux, E. Anderson, B. Bates, A. Pearson, C. Knöchel, D. Hambach, E. A. Stach, and E. Zschech, "Electromigration in passivated Cu interconnects studied by transmission x-ray microscopy," *Journal of Vacuum Science & Technology B*, vol. 20, pp. 3089–3094, 2002.

[18] M. Lane and R. Dauskardt, "Adhesion and reliability of copper interconnects with Ta and TaN barrier layers," *Journal of Materials Research*, vol. 15, pp. 204–211, 2000.

[19] M. Moussavi, "Conventional interconnects: the crisis," *Comptes Rendus de l'academie des Sciences - Series IV - Physics*, vol. 1, pp. 929–939, 2000.

[20] J. Gambino, "Process challenges for integration of copper interconnects with low-k dielectrics," *Electrochemical Society Transactions*, vol. 35, pp. 687–699, 2011.

[21] P. Kohl, D. Bhusari, M. Wedlake, C. Case, F. Klemens, J. Miner, L. Byung-Chan, R. Gutmann, and R. Shick, "Air-gaps in 0.3 μm electrical interconnections," *IEEE Electron Device Letters*, vol. 21, pp. 557 – 559, 2000.

[22] B. Shieh, K. C. Saraswat, J. P. McVittie, S. List, S. Nag, M. Islamraja, and R. H. Havemann, "Air-gap formation during IMD deposition to lower interconnect capacitance," *IEEE Electron Device Letters*, vol. 19, pp. 16–18, 1998.

[23] http://www.IBM.com, Accessed July 2011.

[24] S. Lakshminarayanan, J. Steigerwald, D. T. Price, M. Bourgeois, T. P. Chow, R. J. Gutmann, and S. P. Murarka, "Contact and via structures with copper interconnects fabricated using dual damascene technology," *IEEE Electron Device Letters*, vol. 15, pp. 307–309, 1994.

[25] C. Andricacos, C. Uzoh, J. Dukovic, J. Horkans, and H. Deligianni, "Damascene copper electroplating for chip interconnections," *IBM Journal of Research and Development*, vol. 42, p. 567, 1998.

[26] J. Reid, "Copper electrodeposition: Principles and recent progress," *Japanese Journal of Applied Physics*, vol. 40, pp. 2650–2657, 2001.

[27] A. J. Bard and L. R. Faulkner, *Electrochemical methods Fundamentals and Applications*. Jon Wiley & Sons, 1980.

[28] M. A. Pasquale, L. M. Gassa, and A. J. Arvia, "Copper electrodeposition from an acidic plating bath containing accelerating and inhibiting organic additives," *Electrochimica Acta*, vol. 53, pp. 5891–5904, 2008.

[29] D. Josell, D. Wheeler, W. H. Huber, and T. P. Moffat, "Superconformal electrodeposition in submicron features," *Physical Review Letters*, vol. 8701, p. 016102, 2001.

[30] D. Josell, D. Wheeler, and T. P. Moffat, "Superconformal electrodeposition in vias," *Electrochemical and Solid-State Letters*, vol. 5, pp. C49–C52, 2002.

[31] T. Moffat, D. Wheeler, W. Huber, and D. Josell, "Superconformal electrodeposition of copper," *Electrochemical and Solid-State Letters*, vol. 4, pp. C26–C29, 2001.

[32] T. P. Moffat, B. Baker, D. Wheeler, J. E. Bonevich, M. Edelstein, D. R. Kelly, L. Gan, G. R. Stafford, P. J. Chen, W. F. Egelhoff, and D. Josell, "Superconformal electrodeposition of silver in submicrometer features," *Journal of The Electrochemical Society*, vol. 149, pp. C423–C428, 2002.

[33] R. Rosenberg, D. C. Edelstein, C.-K. Hu, and K. P. Rodbell, "Copper metallization for high performance silicon technology," *Annual Review of Materials Science*, vol. 30, pp. 229–262, 2000.

[34] M. Hayase, M. Taketani, K. Aizawa, T. Hatsuzawa, and K. Hayabusab, "Copper bottom-up deposition by breakdown of PEG-Cl inhibition," *Electrochemical and Solid-State Letters*, vol. 5, pp. C98–C101, 2002.

[35] K. Kondo, T. Matsumoto, and K. Watanabe, "Role of additives for copper damascene electrodeposition," *Journal of The Electrochemical Society*, vol. 151, pp. C250–C255, 2004.

[36] K. Kondo, N. Yamakawa, Z. Tanaka, and K. Hayashi, "Copper damascene electrodeposition and additives," *Journal of Electroanalytical Chemistry and Interfacial Electrochemistry*, vol. 559, pp. 137–142, 2003.

[37] D. Josell, D. Wheeler, W. H. Huber, J. E. Bonevich, and T. P. Moffat, "A simple equation for predicting superconformal electrodeposition in submicrometer trenches," *Journal of The Electrochemical Society*, vol. 148, p. C767, 2001.

[38] J. Kelly, C. Tian, and A. West, "Leveling and microstructural effects of additives for copper electrodeposition," *Journal of The Electrochemical Society*, vol. 146, pp. 2540–2545, 1999.

[39] R. Akolkar and U. Landau, "A time-dependent transport-kinetics model for additive interactions in copper interconnect metallization," *Journal of The Electrochemical Society*, vol. 151, pp. C702–C711, 2004.

[40] A. West, S. Mayer, and J. Reid, "A superfilling model that predicts bump formation," *Electrochemical and Solid-State Letters*, vol. 4, pp. C50–C53, 2001.

[41] R. Akolkar and V. Dubin, "Pattern density effect on the bottom-up fill during damascene copper electrodeposition," *Electrochemical and Solid-State Letters*, vol. 10, pp. D55–D59, 2007.

[42] S. Spiesshoefer, J. Patel, T. Lam, L. Cai, S. Polamreddy, and R. Figueroa, "Copper electroplating to fill blind vias for three-dimensional integration," *Journal of Vacuum Science & Technology A*, vol. 24, pp. 1277–1282, 2006.

[43] S. Kim and J. Kim, "Additive-free superfilling in damascene Cu electrodeposition using microcontact printing," *Electrochemical and Solid-State Letters*, vol. 7, pp. C101–C103, 2004.

[44] M. Hasegawa, Y. Nonaka, Y. Negishi, Y. Okinaka, and T. Osaka, "Enhancement of the ductility of electrodeposited copper films by room-temperature recrystallization," *Journal of The Electrochemical Society*, vol. 153, pp. C117–C120, 2006.

[45] W. Dong, H. Zhang, J. Zheng, and H. Sheng, "Self-annealing of electrodeposited copper thin film during room temperature storage," *Materials Letters*, vol. 62, pp. 1589–1591, 2008.

[46] W. H. Teh, L. T. Koh, S. M. Chen, J. Xie, C. Y. Li, and P. D. Foo, "Study of microstructure and resistivity evolution for electroplated copper films at near-room temperature," *Microelectronics Journal*, vol. 32, pp. 579–585, 2001.

[47] M. Stangl, V. Dittel, J. Acker, V. Hoffmann, W. Gruner, S. Strehle, and K. Wetzig, "Investigation of organic impurities adsorbed on and incorporated into electroplated copper layers," *Applied Surface Science*, vol. 252, pp. 158–161, 2005.

[48] A. Mayadas and M. Shatzkes, "Electrical-resistivity model for polycrystalline films: the case of arbitrary reflection at external surfaces," *Physical Review B, Condensed Matter and Materials Physics*, vol. 1, pp. 1382–1389, 1970.

[49] J. M. E. Harper, J. C. Cabral, P. C. Andricacos, L. Gignac, I. C. Noyan, K. P. Rodbell, and C. K. Hu, "Mechanisms for microstructure evolution in electroplated copper thin films near room temperature," *Journal of Applied Physics*, vol. 86, pp. 2516–2525, 1999.

[50] J. Plombon, E. Andideh, V. M. Dubin, and J. Maiz, "Influence of phonon, geometry, impurity, and grain size on copper line resistivity," *Applied Physics Letters*, vol. 89, p. 113124, 2006.

[51] M. Shimada, M. Moriyama, K. Ito, S. Tsukimoto, and M. Murakami, "Electrical resistivity of polycrystalline Cu interconnects with nano-scale linewidth," *Journal of Vacuum Science & Technology B*, vol. 24, pp. 190–194, 2006.

[52] K. Fuchs, "The conductivity of thin metallic films according to the electron theory of metals," *Proc. Cambridge Phil. Soc.*, vol. 34, pp. 100–108, 1938.

[53] E. Sondheimer, "The mean free path of electrons in metals," *Advances in Physics*, vol. 1, pp. 1–42, 1952.

[54] Z. Basinski and S. Saimoto, "Resistivity of deformed crystals," *Canadian Journal of Physics*, vol. 45, pp. 1161–1176, 1967.

[55] F. J. Blatt, "Effect of point imperfections on the electrical properties of copper. i. conductivity," *Physical Review*, vol. 99, pp. 1708–1716, 1955.

[56] A. Ying, C. Witt, J. Jordan-Sweet, R. Rosenberg, and I. C. Noyan, "A quantitative analysis of room temperature recrystallization kinetics in electroplated copper films using high resolution X-ray diffraction," *Journal of Applied Physics*, vol. 109, p. 014907, 2011.

[57] K. Yin, Y. Xia, C. Chan, W. Zhang, Q. Wang, X. Zhao, A. Li, Z. Liu, M. Bayes, and K. Yee, "The kinetics and mechanism of room-temperature microstructural evolution in electroplated copper foils," *Scripta Materialia*, vol. 58, pp. 65–68, 2008.

[58] R. Huang, W. Robl, H. Ceric, T. Detzel, and G. Dehm, "Stress, sheet resistance, and microstructure evolution of electroplated Cu films during self-annealing," *IEEE Transactions on Device and Materials Reliability*, vol. 10, pp. 47–54, 2010.

[59] S. Chang, J. Shieh, B. Dai, M. Feng, and Y. Li, "The effect of plating current densities on self-annealing behaviors of electroplated copper films," *Journal of The Electrochemical Society*, vol. 149, pp. G535–G538, 2002.

[60] W. Zhang, A. Li, G. Ma, K. Yin, Y. Xia, Z. Liu, C. Chan, K. Cheung, M. Bayes, and K. Yee, "Interpretation of texture changes during self-annealing of electroplated copper," *Microelectronic Engineering*, vol. 87, pp. 2488–2494, 2010.

[61] M. S. Yoon, Y. J. Park, and Y. C. Joo, "Impurity redistributions in electroplated Cu films during self-annealing," *Thin Solid Films*, vol. 408, pp. 230–235, 2002.

[62] J. M. Paik, Y. J. Park, M. S. Yoon, J. H. Lee, and Y. C. Joo, "Anisotropy of grain boundary energies as cause of abnormal grain growth in electroplated copper films," *Scripta Materialia*, vol. 48, pp. 683–688, 2003.

[63] K. Pantleon and M. A. J. Somers, "Evolution of the microstructure in nanocrystalline copper electrodeposits during room temperature storage," *Zeitschrift Fur Kristallographie*, vol. 2, pp. 261–266, 2007.

[64] S. H. Brongersma, E. Kerr, I. Vervoort, A. Saerens, and K. Maex, "Grain growth, stress, and impurities in electroplated copper," *Journal of Materials Research*, vol. 17, pp. 582–589, 2002.

[65] M. Stangl and M. Militzer, "Modeling self-annealing kinetics in electroplated Cu thin films," *Journal of Applied Physics*, vol. 103, p. 113521, 2008.

[66] H. Lee, W. Nix, and S. Wong, "Studies of the driving force for room-temperature microstructure evolution in electroplated copper films," *Journal of Vacuum Science & Technology B*, vol. 22, pp. 2369–2374, 2004.

[67] S. Lagrange, S. H. Brongersma, M. Judelewicz, A. Saerens, I. Vervoort, E. Richard, R. Palmans, and K. Maex, "Self-annealing characterization of electroplated copper films," *Microelectronic Engineering*, vol. 50, pp. 449–457, 2000.

[68] G. Brunoldi, S. Guerrieri, S. G. Alberici, E. Ravizza, G. Tallarida, C. Wiemer, and T. Marangon, "Self-annealing and aging effect characterization on copper seed thin films," *Microelectronic Engineering*, vol. 82, pp. 289–295, 2005.

[69] C. Lingk and M. E. Gross, "Recrystallization kinetics of electroplated Cu in damascene trenches at room temperature," *Journal of Applied Physics*, vol. 84, pp. 5547–5553, 1998.

[70] T. Osaka, N. Yamachika, M. Yoshino, M. Hasegawa, Y. Negishi, and Y. Okinaka, "Effect of carbon content on the electrical resistivity of electrodeposited copper," *Electrochemical and Solid-State Letters*, vol. 12, pp. D15–D17, 2009.

[71] J. Gao, "The influence of additives on microstructure evolution of electrochemically deposited copper films," Master's thesis, The University of British Columiba, 2003.

[72] T. Ritzdorf, L. Chen, D. Fulton, and C. Dundas, "Comparative investigation of plating conditions on self-annealing of electrochemically deposited copper films," in *IEEE International Interconnect Technology Confernece*, pp. 287 – 289, 1999.

[73] J. Neuner, I. Zienert, A. Peeva, A. Preuße, P. Kücher, and J. W. Bartha, "Microstructure in copper interconnects- influence of plating additive concentration," *Microelectronic Engineering*, vol. 87, pp. 254–257, 2010.

[74] M. Stangl, J. Acker, O. S., M. Uhlehmann, T. Gemming, S. Baunack, and K. Wetzig, "Incorporation of sulfur, chlorine, and carbon into electroplated Cu thin films," *Microelectronic Engineering*, vol. 84, pp. 54–59, 2007.

[75] O. Dubreuil, V. Caubet-Hilloutou, J. Guillan, K. Haxaire, M. Mellier, P. Caubet, P. Vannier, E. Petitprez, D. Bellet, and P. Normandon, "Characterization and impact of reduced copper plating overburden on 45 nm interconnect performances," *Microelectronic Engineering*, vol. 87, pp. 421–425, 2010.

[76] M. Stangl, M. Lipták, A. Fletcher, J. Acker, J. Thomas, H. Wendrock, S. Oswald, and K. Wetzig, "Influence of initial microstructure and impurities on Cu room-temperature recrystallization (self-annealing)," *Microelectronic Engineering*, vol. 85, pp. 534–541, 2008.

[77] D. T. Read, Y. W. Cheng, and R. Geiss, "Morphology, microstructure, and mechanical properties of a copper electrodeposit," *Microelectronic Engineering*, vol. 75, pp. 63–70, 2004.

[78] F. J. Humphreys and M. Hatherly, *Recrystallization and Related Annealing Phenomena*. Pergamon, 2004.

[79] W. Cao, C. Gu, E. Pereloma, and C. Davies, "Stored energy, vacancies and thermal stability of ultra-fine grained copper," *Materials Science and Engineering A*, vol. 492, pp. 74–79, 2008.

[80] R. A. Vandermeer, D. J. Jensen, and E. Woldt, "Grain boundary mobility during recrystallization of copper," *Metallurgical and Materials Transactions A*, vol. 28A, pp. 749–754, 1997.

[81] D. Field, L. Bradford, M. Nowell, and T. Lillo, "The role of annealing twins during recrystallization of Cu," *Acta Materialia*, vol. 55, pp. 4233–4241, 2007.

[82] Y. Amouyal, S. Divinski, L. Klinger, and E. Rabki, "Grain boundary diffusion and recrystallization in ultrafine grain copper produced by equal channel angular pressing," *Acta Materialia*, vol. 56, pp. 5500–5513, 2008.

[83] K. Shen, M. Guo, and M. Wang, "Recrystallization characteristics of a fine grained copper alloy," *Materials Chemistry and Physics*, vol. 120, pp. 709–714, 2010.

[84] S. Wright and M. Nowell, *Electron Backscatter Diffraction in Materials Science*, ch. A Review of In Situ EBSD Studies, pp. 329–337. Springer, 2009.

[85] M. Nowell, S. Wright, and J. Carpenter, "In-situ orientation imaging of recrystallization and grain growth in OFHC copper," *Microscopy and Microanalysis*, vol. 15, pp. 678–679, 2009.

[86] J. Freudenberger, A. Kauffmann, H. Klauß, T. Marr, K. Nenkov, V. S. Sarma, and L. Schultz, "Studies on recrystallization of single-phase copper alloys by resistance measurements," *Acta Materialia*, vol. 58, pp. 2324–2329, 2010.

[87] G. Benchabanea, Z. Boumerzouga, I. Thibonb, and T. Gloriantb, "Recrystallization of pure copper investigated by calorimetry and microhardness," *Materials Characterization*, vol. 59, pp. 1425–1428, 2008.

[88] C. Detavernier, S. Rossnagel, C. Noyan, S. Guha, C. Cabral, and C. Lavoie, "Thermodynamics and kinetics of room-temperature microstructural evolution in copper films," *Journal of Applied Physics*, vol. 94, pp. 2874–2881, 2003.

[89] C. Zener, "Private communication with C.S. Smith," *Transactions of the Metallurgical Society of AIME*, vol. 175, p. 15, 1949.

[90] J. min Zhang, K. wei Xu, and V. Ji, "Strain-energy-driven abnormal grain growth in copper films on silicon substrates," *Journal of Crystal Growth*, vol. 226, pp. 168–174, 2001.

[91] N. Fukumuro, T. Adachi, S. Yae, H. Matsuda, and Y. Fukai, "Influence of hydrogen on room temperature recrystallisation of electrodeposited Cu films: thermal desorption spectroscopy," *Transactions of the Institute of Metal Finishing*, vol. 89, pp. 198–201, 2011.

[92] S. P. Hau-Riege and C. V. Thompson, "In situ transmission electron microscope studies of the kinetics of abnormal grain growth in electroplated copper films," *Applied Physics Letters*, vol. 76, pp. 309–311, 2000.

[93] C. Lee and C. Park, "Residual stress effect on self-annealing of electroplated copper," *Japanese Journal of Applied Physics*, vol. 42, pp. 4484–4488, 2003.

[94] S. Rossnagel and T. Kuan, "Alteration of Cu conductivity in the size effect regime," *Journal of Vacuum Science & Technology B*, vol. 22, pp. 240–247, 2004.

[95] K. Vanstreels, S. H. Brongersma, Z. Tokei, L. Carbonell, W. D. Ceuninck, J. D'Haen, and M. D'Olieslaeger, "Increasing the mean grain size in copper films and features," *Journal of Materials Research*, vol. 23, pp. 642–662, 2008.

[96] S. Rossnagel and T. Kuan, "Time development of microstructure and resistivity for very thin Cu films," *Journal of Vacuum Science & Technology A*, vol. 20, pp. 1911–1915, 2002.

[97] K.-W. Chen, L.-H. Hsu, J.-K. Huang, Y.-L. Wang, and K.-Y. Lo, "A strategic copper plating method without annealing process," *Journal of The Electrochemical Society*, vol. 156, pp. D448–D451, 2009.

[98] K. N. Chen, A. Fan, C. S. Tan, R. Reif, and C. Y. Wen, "Microstructure evolution and abnormal grain growth during copper wafer bonding," *Applied Physics Letters*, vol. 81, pp. 3774–3776, 2002.

[99] M. Militzer, P. Freundlich, and D. Bizzotto, "Abnormal grain growth in electrochemically deposited cu films," *Recrystallization and Grain Growth, Pts 1 and 2*, vol. 467-470, pp. 1339–1344, 2004.

[100] K. Pantleon, J. Jensen, and M. Somers, "Interpretation of quantitative crystallographic texture in copper electrodeposits on amorphous substrates," *Journal of The Electrochemical Society*, vol. 151, pp. C45–C51, 2004.

[101] K. Yin, Y. Xia, W. Zhang, Q. Wang, X. Zhao, A. Li, Z. Liu, X. Hao, L. Wei, C. Chan, K. Cheung, M. Bayes, and K. Yee, "Room-temperature microstructural evolution of electroplated Cu studied by focused ion beam and positron annihilation lifetime spectroscopy," *Journal of Applied Physics*, vol. 103, p. 066103, 2008.

[102] K. Pantleon and M. Somers, "In situ investigation of the microstructure evolution in nanocrystalline copper electrodeposits at room temperature," *Journal of Applied Physics*, vol. 100, pp. 114319 1–7, 2006.

[103] Q. Jiang and M. Thomas, "Recrystallization effects in Cu electrodeposits used in fine line damascene structures," *Journal of Vacuum Science & Technology B*, vol. 19, pp. 762–766, 2001.

[104] S. Kang, Y. Obeng, M. Decker, M. Oh, S. Merchant, S. Karthikeyan, C. Seet, and A. Oates, "Effect of annealing on the surface microstructural evolution and the electromigration reliability of electroplated Cu films," *Journal of Electronic Materials*, vol. 30, pp. 1506–1512, 2001.

[105] V. Carreau, S. Maîtrejean, M. Verdier, Y. Bréchet, A. Roule, A. Toffoli, V. Delaye, and G. Passemard, "Evolution of Cu microstructure and resistivity during thermal treatment of damascene line: Influence of line width and temperature," *Microelectronic Engineering*, vol. 84, pp. 2723–2728, 2007.

[106] S. Donthu, M. Vora, S. Lahiri, C. Thompson, and S. Yi, "Activation energy determination for recrystallization in electroplated-copper films using differential scanning calorimetry," *Journal of Electronic Materials*, vol. 32, pp. 531–534, 2003.

[107] L. Lu, N. Tao, L. Wang, B. Ding, and K. Lu, "Grain growth and strain release in nanocrystalline copper," *Journal of Applied Physics*, vol. 89, pp. 6408–6414, 2001.

[108] D. Gupta, "Comparative Cu diffusion studies in advanced metallizations of Cu and Al-Cu based thin films," in *Materials Research Society Proceeding*, vol. 337, p. 209, 1994.

[109] W. A. Johnson and R. F. Mehl, "Reaction kinetics in processes of nucleation and growth," *Trans. AIME*, vol. 135, p. 416, 1939.

[110] S. Brongersma, E. Richard, I. Vervoort, and K. Maex, "A grain size limitation inherent to electroplated copper films," in *Proceedings of the IEEE 2000 International Interconnect Technology Conference*, 2000.

[111] A. Uedono, T. Suzuki, T. Nakamura, T. Ohdaira, and R. Suzuki, "Defects introduced into electroplated Cu films during roomtemperature recrystallization probed by a monoenergetic positron beam," *Journal of applied physics*, vol. 98, p. 043504, 2005.

[112] K. Pantleon and M. A. Somer, "Interpretation of microstructure evolution during self-annealing and thermal annealing of nanocrystalline electrodeposits-a comparative study," *Materials Science and Engineering A*, vol. 528, pp. 65–71, 2010.

[113] D. Walther, M. Gross, K. Evans-Lutterodt, W. Brown, M. Oh, S. Merchant, and P. Naresh, "Room temperature recrystallization of electroplated copper thin films: methods and mechanisms," in *Material Research Society Symposium Proceedings*, vol. 612, 2000.

[114] D. Xu, W. L. Kwan, K. Chen, X. Zhang, V. Ozolins, and K. N. Tu, "Nanotwin formation in copper thin films by stress/strain relaxation in pulse electrodeposition," *Applied Physics Letters*, vol. 91, pp. 254105 1–3, 2007.

[115] D. Xu, V. Sriram, V. Ozolins, J.-M. Yang, K. Tu, G. R. Stafford, C. Beauchamp, I. Zienert, H. Geisler, P. Hofmann, and E. Zschech, "Nanotwin formation and its physical properties and effect on reliability of copper interconnects," *Microelectronic Engineering*, vol. 85, pp. 2155–2158, 2008.

[116] K. Lu, L. Lu, and S. Suresh, "Strengthening materials by engineering coherent internal boundaries at the nanoscale," *Science*, vol. 324, pp. 349–352, 2009.

[117] G. Lui, D. Chen, and J.-C. Kuo, "EBSD characterization of twinned copper using pulsed electrodeposition," *Journal of Physics D: Applied Physics*, vol. 42, p. 215410, 2009.

[118] M. Hauder, J. Gstottner, W. Hansch, and D. Schmitt-Landsiedel, "Scaling properties and electromigration resistance of sputtered Ag metallization lines," *Applied Physics Letters*, vol. 78, p. 838, 2001.

[119] K. Hansen and K. Pantleon, "Microstructure stability of silver electrodeposits at room temperature," *Scripta Materialia*, vol. 58, pp. 96–98, 2008.

[120] A. Isobayashi, Y. Enomoto, H. Yamada, S. Takahashi, and S. Kadomura, "Thermally robust Cu interconnects with Cu-Ag alloy for sub 45nm node." IEDM Proc., pp. 953-956, 2004.

[121] Y. Ko, J. Jang, S. Lee, H. Yang, W. Lee, J. Lee, and P. Reucroft, "Thickness effect on grain growth and precipitate coarsening of a copper-silver thin film in an advanced metallization process," *Journal of Materials Science: Materials in Electronics (USA)*, vol. 14, pp. 103–108, 2003.

[122] S. Strehle, S. Menzel, H. Wendrock, J. Acker, and K. Wetzig, "Microstructural investigation of electrodeposited CuAg-thin films," *Microelectronic Engineering*, vol. 70, pp. 506–511, 2003.

[123] W. Shao, G. Pattanaik, and G. Zangari, "Electrodeposition of copper-silver alloys on n-Si (100) from acidic sulfate solution," in *210 Electrochemical Society Meeting*, 2006.

[124] S. Strehle, S. Menzel, K. Wetzig, and J. Barth, "Microstructure of electroplated Cu(Ag) alloy thin films," *Thin Solid Films*, vol. 519, pp. 3522–3529, 2011.

[125] S. Strehle, R. Reiche, V. Hoffmann, J. Acker, T. Gemming, and K. Wetzig, "Sulfur incorporation in electroplated Cu(Ag) thin films," *Micorchimica Acta*, vol. 156, pp. 167–172, 2006.

[126] S. Menzel, S. Strehle, H. Wendrock, and K. Wetzig, "Effect of Ag-alloying addition on the stress-temperature behavior of electroplated copper thin films," *Applied Surface Science*, vol. 252, pp. 211–214, 2005.

[127] F. Smits, "Measurement of sheet resistivities with the four-point probe," *The Bell System Technical Journal*, vol. 37, pp. 711–718, 1958.

[128] X. Zhang, H. Xie, M. Fujii, H. Ago, K. Takahashi, T. Ikuta, H. Abe, and T. Shimizu, "Thermal and electrical conductivity of a suspended platinum nanofilm," *Applied Physics Letters*, vol. 86, p. 171912, 2005.

[129] M. Nowell, R. Witt, and B. True, "EBSD sample preparation: Techniques, tips, and tricks," *Microscopy and Microanalysis*, vol. 11, pp. 504–505, 2005.

[130] *OIM analysis software version 5.2 users manual*.

[131] H. Tu, P. Yen, S. Chen, and S. Yau, "In situ STM imaging of bis-3-sodiumsulfopropyl-disulfide molecules adsorbed on copper film electrodeposited on Pt(111) single crystal electrode," *Langmuir*, vol. 27, pp. 6801–6807, 2011.

[132] A. Frank and A. Bard, "The decomposition of the sulfonate additive sulfopropyl sulfonate in acid copper electroplating chemistries," *Journal of The Electrochemical Society*, vol. 150, pp. C244–C250, 2003.

[133] N. Alshwawreh, M. Militzer, D. Bizzotto, and J.-C. Kuo, "Resistivity-microstructure correlation of self-annealed electrodeposited copper thin films," *Microelectronic Engineering*, vol. 95, pp. 26–33, 2012.

[134] S. Wright and M. Nowell, "EBSD image quality mapping," *Microscopy and Microanalysis*, vol. 12, pp. 72–84, 2006.

[135] X. Tao, *An EBSD study on mapping of small orientation differences in lattice mismatched heterostructures*. PhD thesis, Lehigh University, 2003.

[136] J. Wu, P. Wray, C. Garcia, M. Hua, and A. Deardo, "Image quality analysis: A new method of characterizing microstructures," *ISIJ International*, vol. 45, pp. 254–265, 2005.

[137] J. Tarasiuk, P. Gerber, and B. Bacroix, "Estimation of recrystallized volume fraction from EBSD data," *Acta Materialia*, vol. 50, pp. 1467–1477, 2002.

[138] F. Humphreys, "Review grain and subgrain characterisation by electron backscatter diffraction," *Journal of Materials Science*, vol. 36, pp. 3833–3854, 2001.

[139] D. Field, R. Eames, and T. Lillo, "The role of shear stress in the formation of annealing twin boundaries in copper," *Scripta Materialia*, vol. 54, pp. 983–986, 2006.

[140] T. Nemoto, T. Fukino, S. Tsurekawa, X. Gu, A. Teramoto, and T. Ohmi, "In situ observation of grain growth on electroplated Cu film by electron backscatter diffraction," *Japanese Journal of Applied Physics*, vol. 48, p. 066507, 2009.

[141] F. Mompiou, M. Legros, and D. Caillard, "Stress assisted grain growth in ultrafine and nanocrystalline aluminum revealed by in-situ TEM," *Materials Research Society Proceedings*, vol. 1086, pp. U09–04, 2008.

[142] N. Alshwawreh, M. Militzer, and D. Bizzotto, "Recrystallization of electrodeposited copper thin films during annealing," *Journal of Electronic Materials*, vol. 39, pp. 2476–2482, 2010.

[143] C. Cabral, P. Andricacos, L. Gignac, I. Noyan, K. Rodbell, T. Shaw, R. Rosenberg, J. Harper, P. DeHaven, P. Locke, S. Malhotra, C. Uzoh, and S. Klepeis, "Room temperature evolution of microstructure and resistivity in electroplated copper films," in *Proceeding of the Advanced Metallization Conference XIV*, p. 81, 1999.

[144] J. Cahn, "Transformation kinetics during continous cooling," *Acta Materialia*, vol. 4, pp. 572–575, 1956.

[145] M. Ferry, D. Muljono, and D. Dunne, "Recrystallization kinetics of low and ultra low carbon steels during high-rate annealing," *ISIJ International*, vol. 41, pp. 1053–1060, 2001.

[146] S. Chang, J. Shieh, K. Lin, B. Dai, T. Wang, C. Chen, and M. Feng, "Investigation of effects of bias polarization and chemical parameters on morphology and filling capability of 130 nm damascene electroplated copper," *Journal of Vacuum Science & Technology B*, vol. 19, pp. 767–773, 2001.

[147] C. E. Krill and L. Chen, "Computer simulation of 3-d grain growth using a phase-field model," *Acta Materialia*, vol. 50, pp. 3059–3075, 2002.

[148] I. Steinbach, F. Pezzolla, B. Nestler, M. SeeBelberg, R. Prieler, G. J. Schmitz, and J. L. L. Rezende, "A phase field concept for multiphase systems," *Physica D: Nonlinear Phenomena*, vol. 94, pp. 135–147, 1996.

[149] J. A. Warren and W. J. Boettinger, "Prediction of dendritic growth and microsegregation patterns in a binary alloy using the phase-field method," *Acta Metallurgica et Materialia*, vol. 43, pp. 689–703, 1995.

[150] M. Militzer, M. Mecozzi, J. Sietsma, and S. van der Zwaag, "Three-dimensional phase field modelling of the austenite-to-ferrite transformation," *Acta Materialia*, vol. 54, pp. 3961–3972, 2006.

[151] I. Steinbach, "Phase-field models in materials science," *Modelling and Simulation in Materials Science and Engineering*, vol. 17, p. 073001, 2009.

[152] T. Takaki, A. Yamanaka, Y. Higa, and Y. Tomita, "Phase-field model during static recrystallization based on crystal plasticity theory," *Journal of Computer-Aided Materials Design*, vol. 14, pp. 75–84, 2007.

[153] N. Moelans, B. Blanpain, and P. Wollants, "A phase field model for the simulation of grain growth in materials containing finely dispersed incoherent second-phase particles," *Acta Materialia*, vol. 53, pp. 1771–1781, 2005.

[154] N. Moelans, B. Blanpain, and P. Wollants, "Phase field simulations of grain growth in two-dimensional systems containing finely dispersed second-phase particles," *Acta Materialia*, vol. 54, pp. 1175–1184, 2006.

[155] P. Cha, S. Kim, D. Yeon, and J. Yoon, "A phase field model for the solute drag on moving grain boundaries," *Acta Materialia*, vol. 50, pp. 3817–3829, 2002.

[156] D. Fan and L. Q. Chen, "Computer simulation of grain growth using a continuum field model," *Acta Materialia*, vol. 45, pp. 611–622, 1997.

[157] N. Moelans, B. Blanpain, and P. Wollants, "An introduction to phase-field modeling of microstructure evolution," *Computer Coupling of Phase Diagrams and Thermochemistry*, vol. 32, pp. 268–294, 2008.

[158] S. Kim, D. Kim, W. Kim, and Y. Park, "Computer simulations of two-dimensional and three-dimensional ideal grain growth," *Physical Review E*, vol. 74, p. 061605, 2006.

[159] M. Militzer, "Phase field modeling of microstructure evolution in steels," *Current Opinion in Solid State and Materials Science*, vol. 15, pp. 106–115, 2011.

[160] Y. Suwa, Y. Saito, and H. Onodera, "Phase field simulation of stored energy driven interface migration at a recrystallization front," *Materials Science and Engineering A*, vol. 457, pp. 132–138, 2007.

[161] http://www.access.rwth-aachen.de/MICRESS/.

[162] W. Wu, D. Ernur, S. Brongersma, M. Hove, and K. Maex, "Grain growth in copper interconnect lines," *Microlectronic Engineering*, vol. 76, pp. 190–194, 2004.

[163] H.-J. Lee, D. I. Kim, J. H. Ahn, and D. N. Lee, "Electron backscattered diffraction analysis of copper damascene interconnect for ultralarge-scale integration," *Thin Solid Films*, vol. 474, pp. 250–254, 2005.

[164] C. Davies and A. Jones, "The precipitation of silver chloride from aqueous solutions: Part 2.-kinetics of growth of seed crystals," *Transactions of the Faraday Society*, vol. 51, pp. 812–817, 1955.

Appendix A

Copper-Silver Co-Deposition

When silver is added to the standard solution (i.e. chloride is present), silver chloride (AgCl) precipitates immediately. The solubility limit of silver and chloride in solution is given by [164]

$$[Ag^+][Cl^-] = K_{sp} = 1.8 \times 10^{-10}$$

Here, $[Ag^+]$, $[Cl^-]$, and K_{sp} are the concentration of silver (Molar units), concentration of chloride (Molar units) and the solubility product, respectively. A given amount of silver reacts with a given amount of chloride to form silver chloride. The solubility equation can be then written as

$$[Ag^+ - x_p][Cl^- - x_p] = K_{sp} = 1.8 \times 10^{-10}$$

Here x_p represents the concentration of silver and the concentration of chloride that are consumed by the reaction. Figure A.1-a shows the amount of silver that remains in the solution as a function of the concentration of silver that is added. The silver concentration that is available to co-deposit with copper increases with increasing the concentration of added silver. However, the formation of silver chloride decreases the concentration of silver in solution significantly. Figure A.1-b shows that there is no significant change in the concentration of chloride when the added silver concentration is less than 0.1 mM.

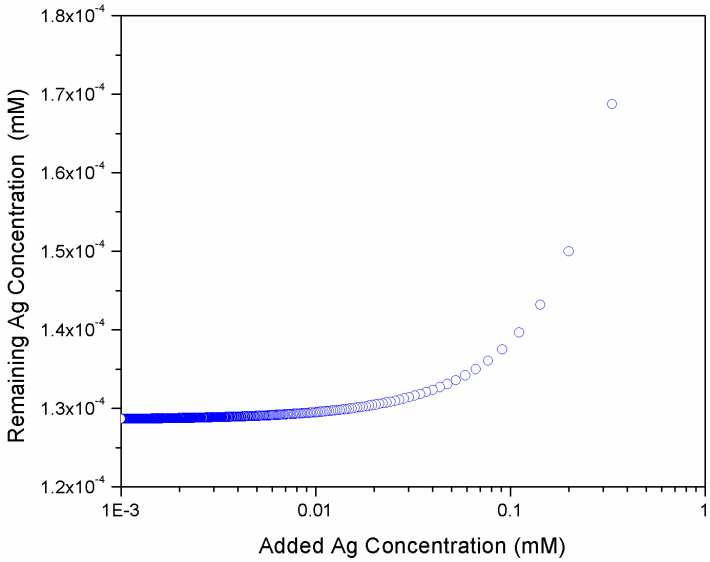

(a)

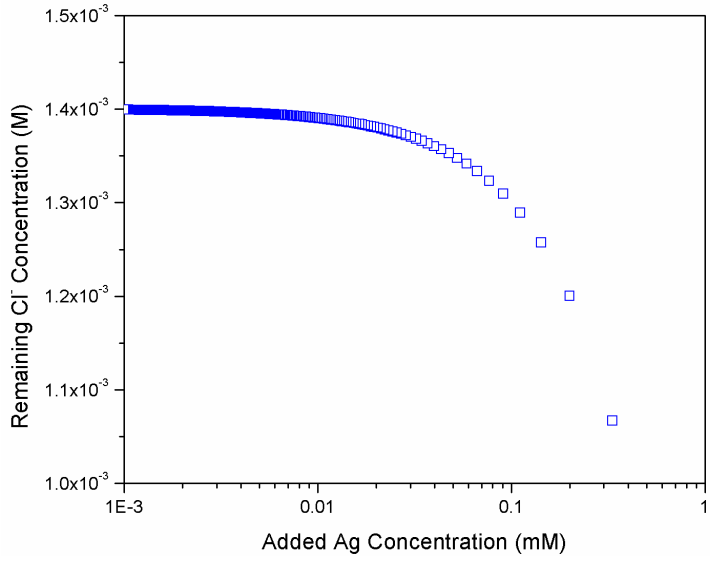

(b)

Figure A.1: (a) The concentration of silver remaining in the solution after silver chloride precipitation as a function of the added silver concentration. (b) The concentration of chloride remaining in the solution.

Appendix B

Phase-Field Model Sensitivity Analysis of a Shrinking Grain

Figure B.1 shows the PFM simulations for the case of a shrinking grain due to the curvature driving pressure (i.e. no stored energy was considered). To simplify the simulations, the grain was simulated as a circle with an initial radius of 4 μm. The interface mobility was considered to be 7.1×10^{-8} cm^4/Js. Here, the grain radius decreases with time and the circle disappeared after 6.1 hours. The change in the grain radius as a function of time is shown in Fig. B.2. Similar to the results observed for the case of recrystallization, there is a difference between the radius profile from the PFM simulations and that using the analytical solution (assuming ideal grain growth). As discussed in chapter 8, the mobility of the interface can be adjusted to replicate the analytical radius profile. Here, the mobility should be increased to 9.0 $\times10^{-8}$ cm^4/Js. The correction factor in this case is 1.27. There is a difference between the correction factors obtained from recrystallization and shrinking grain simulations. This suggests that the accuracy of the PFM simulations in MICRESS is different for grain growth and recrystallization processes.

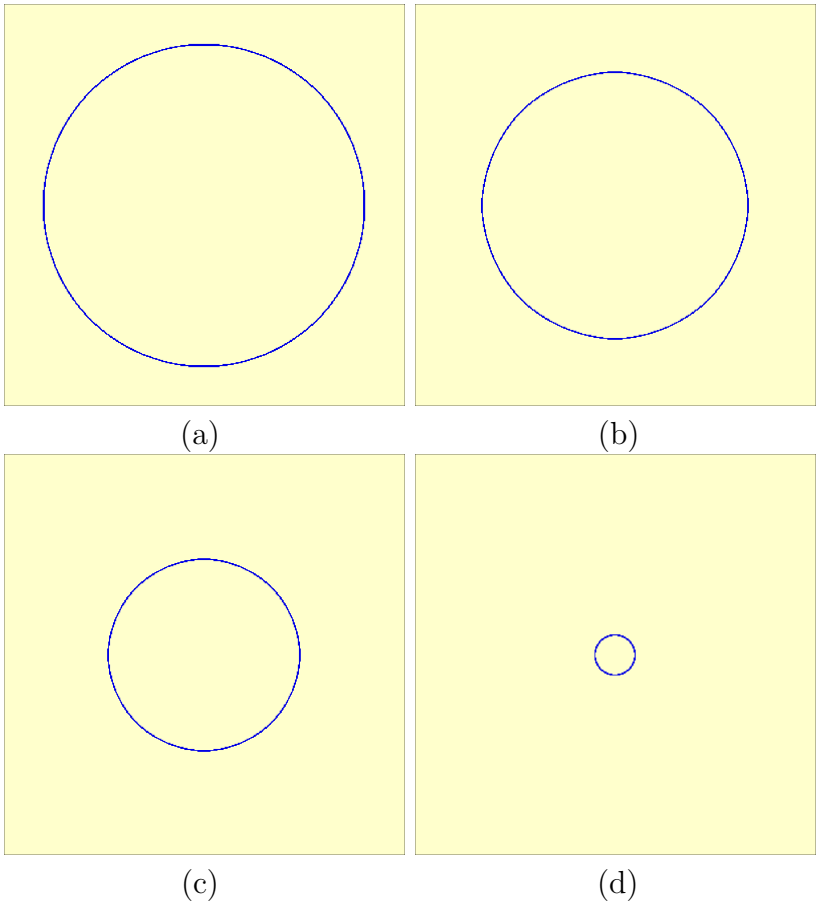

Figure B.1: Phase-Field simulation of a shrinking grain due to the curvature effect. The domain size is 10 μm$\times$ 10 μm and the initial radius of the circle is 4 μm. The interface mobility was considered to be 7.1 $\times$ 10^{-8} cm^4/Js and Δx was 0.025 μm. The interface thickness was considered to be $4\Delta x$. (a) $t = 0$h (b) $t = 2$h (c) $t = 4$h and (d) $t = 6$h.

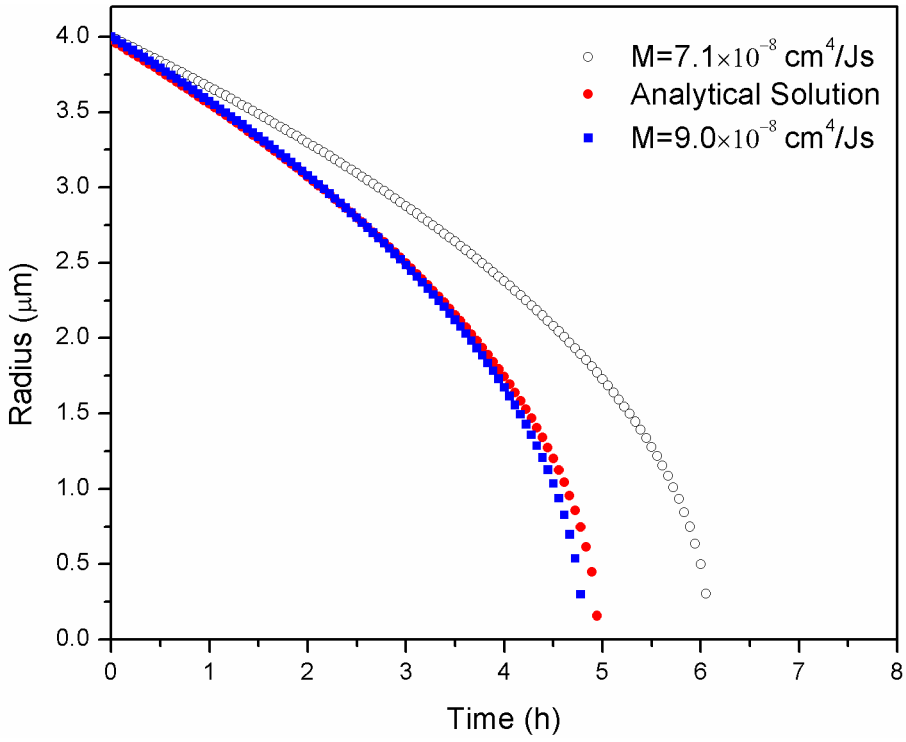

Figure B.2: The change in the grain radius as a function of time.